

VILNIUS UNIVERSITY  
CENTER FOR PHYSICAL SCIENCES AND TECHNOLOGY

Paulius Gaigalas

**Synthesis and characterization of  
effective nanoplatelet structure  
catalysts for electrochemical water  
splitting**

**DOCTORAL DISSERTATION**

Natural Sciences,  
Chemistry (N 003)

VILNIUS 2023

The dissertation was prepared between 2019 and 2023 at the Center for Physical Sciences and Technology.

The research was supported by Research Council of Lithuania (Mobility funding – P-DAK-22-62)

**Academic supervisor** – Dr. Arūnas Jagminas (Center for Physical Sciences and Technology, Natural Sciences, Chemistry – N 003).

This doctoral dissertation will be defended in a public meeting of the Dissertation Defence Panel:

**Chairman** – Prof. Habil. Dr. Rimantas Ramanauskas (Center for Physical Sciences and Technology, Natural Sciences, Chemistry – N 003).

**Members:**

Prof. Dr. Henrikas Cesiulis (Vilnius University, Natural Sciences, Chemistry – N 003)

Dr. Jurga Juodkazytė (Center for Physical Sciences and Technology, Natural Sciences, Chemistry – N 003),

Habil. Dr. Zenonas Jusys (Helmholtz Institute Ulm, Natural Sciences, Chemistry – N 003),

Prof. Dr. Tomas Tamulevičius (Kaunas University of Technology, Natural Sciences, Physics – N 002).

The dissertation shall be defended at a public meeting of the Dissertation Defence Panel at 11 a.m. on 1<sup>st</sup> December 2023 in meeting room A101 of the Center for Physical Sciences and Technology.

Address: Saulėtekio al. 3, Vilnius, Lithuania

Tel. +370852649211; e-mail: office@ftmc.lt

The text of this dissertation can be accessed at the libraries of Center for Physical Sciences and Technology, Vilnius University as well as on the website of Vilnius University:

[www.vu.lt/lt/naujienos/ivykiu-kalendorius](http://www.vu.lt/lt/naujienos/ivykiu-kalendorius)

VILNIAUS UNIVERSITETAS  
FIZINIŲ IR TECHNOLOGIJOS MOKSLŲ CENTRAS

Paulius Gaigalas

# Efektyvių nanolapelinės struktūros katalizatorių elektrocheminei vandens skaldymo reakcijai sintezė ir tyrimas

**DAKTARO DISERTACIJA**

Gamtos mokslai,  
Chemija (N 003)

VILNIUS 2023

Disertacija rengta 2019–2023 metais Fizinių ir technologijos mokslų centre.  
Mokslinius tyrimus rėmė Lietuvos mokslų taryba (Parama išvykoms – P-DAK-22-62)

**Mokslinis vadovas** – dr. Arūnas Jagminas (VMTI Fizinių ir technologijos mokslų centras, gamtos mokslai, chemija – N 003)

Gynimo taryba:

**Pirmininkas** – prof. habil. dr. Rimantas Ramanauskas (VMTI Fizinių ir technologijos mokslų centras, gamtos mokslai, chemija – N 003).

**Nariai:**

prof. dr. Henrikas Cesiulis (Vilniaus universitetas, gamtos mokslai, chemija N 003),

dr. Jurga Juodkazytė (VMTI Fizinių ir technologijos mokslų centras, gamtos mokslai, chemija – N 003),

habil. dr. Zenonas Jusys (Ulmo Helmholco institutas, gamtos mokslai, chemija – N 003),

prof. dr. Tomas Tamulevičius (Kauno technologijos universitetas, gamtos mokslai, fizika – N 002).

Disertacija ginama viešame Gynimo tarybos posėdyje 2023 m. gruodžio mėn.  
1 d. 11 val. Fizinių ir technologijos mokslų centro A101 posėdžiu salėje.

Adresas: Saulėtekio al. 3, Vilnius, Lietuva,  
tel. +370852649211; el. paštas office@ftmc.lt

Disertaciją galima peržiūrėti Fizinių ir technologijos mokslų centro, Vilniaus universiteto bibliotekose ir VU interneto svetainėje adresu:

<https://www.vu.lt/naujienos/ivykiu-kalendorius>

## PADĖKA/ACKNOWLEDGEMENTS

Nuoširdžiai dėkoju savo darbo vadovui, dr. Arūnui Jagminui, už padrąsinimą ir palaikymą svarstant rinktis doktorantūros studijas, pagalbą bei suteiktas žinias susiduriant su visais kilusiais klausimais ir kasdien juntamą rūpestį bei nuoširdumą.

Taip pat dėkoju dr. Vaclovui Klimui už kantrybę, pamokymus bei patarimus gilinantį elektrochemijos mokslą, išsakytas pastabas ir futbolo rezultatų aptarimus bei pokalbius prie arbato. Ačiū visiems Nanostruktūrų laboratorijos kolegom už palaikymą ir draugiškumą.

Ačiū dr. Arnui Naujokaičiui, dr. Romualdui Trusovui, dr. Vidui Pakštui, dr. Ievai Matulaitienei bei dr. Tomui Sabirovui už atliktus SEM, Raman spektroskopijos, XRD, FTIR ir EIS matavimus bei pagalbą atliekant gautų duomenų analizę.

Ačiū šeimai ir draugams, mane palaikiusiems ir padėjusiems kartu siekti užsibrėžtų tikslų.

I would also like to thank dr. Carla Bittencourt for collaboration, analysis of recorded XPS spectra, lessons on the theory of XPS and fitting of obtained spectra. I thank you for your hospitality and the warm reception I got from you and all your colleagues at ChIPS laboratory during my stay in Mons.

## LIST OF ABBREVIATIONS

2D (3D)	Two-dimensional (three-dimensional)	Dvidimensis (tridimensis)
BE	Binding energy	Ryšio energija
CPE	Constant phase element	Pastovios fazės elementas
CV	Cyclic voltammetry	Ciklinė voltamperometrija
CVD	Chemical vapour deposition	Cheminių graų nusodinimas
Cys	Cysteine	Cisteinas
DFT	Density-functional theory	Tankio funkcijos teorija
DMF	N,N-dimethylformamide	N,N-dimetilformamidas
ECSA	Electrochemical surface area	Elektrocheminis paviršiaus plotas
EDX	Energy dispersive X-ray spectroscopy	Rentgeno spindulių energijos dispersijos spektroskopija
EEC	Equivalent electric circuit	Ekvivalentinė elektrinė grandinė
FTIR	Fourier-transform infrared spectroscopy	Furjė-transformacijos infraraudonųjų spindulių spektroskopija
Gly	Glycine	Glicinas
HER	Hydrogen evolution reaction	Vandenilio išskyrimo reakcija
His	Histidine	Histidinas
HRTEM	High-resolution transmission electron microscopy	Aukštos raiškos peršvietimo elektronų mikroskopija
LPE	Liquid phase exfoliation	Skystos fazės eksfoliavimas
OER	Oxygen evolution reaction	Deguonies išskyrimo reakcija
PL	Photoluminescence	Fotoluminescencija
PTFE	Polytetrafluoroethylene	Politetrafluoroetilenas
RHE	Reversible hydrogen electrode	Grįžtamasis vandenilio elektrodas
SEM	Scanning electron microscopy	Skenuojanti elektronų mikroskopija
SHE	Standard hydrogen electrode	Standartinis vandenilio elektrodas
TGA-DSC	Thermogravimetric analyzer – differential scanning calorimeter	Termogravimetrinis analizeris – diferencialinis skenuojantis kalorimetras
TMD	Transition metal dichalcogenide	Pereinamujų metalų dichalkogenidas
TOF	Turnover frequency	Apyvartos dažnis
XPS	X-ray photoelectron spectroscopy	Rentgeno fotoelektronų spektroskopija
XRD	X-ray diffraction	Rentgeno spindulių difrakcija

## TABLE OF CONTENTS

PADÉKA/ACKNOWLEDGEMENTS .....	5
LIST OF ABBREVIATIONS .....	6
TABLE OF CONTENTS .....	7
INTRODUCTION.....	10
MAIN GOAL .....	11
TASKS .....	11
SCIENTIFIC NOVELTY.....	12
STATEMENTS OF DEFENCE.....	12
CONTRIBUTIONS OF AUTHOR .....	12
1. LITERATURE REVIEW .....	14
1.1. Properties of molybdenum disulfide .....	14
1.1.1. MoS <sub>2</sub> structure and polytypes.....	14
1.1.2. Characterization of MoS <sub>2</sub> .....	16
1.2. Synthesis of molybdenum disulfide nanomaterials.....	20
1.2.1. Exfoliation of MoS <sub>2</sub> .....	20
1.2.2. Chemical/physical vapour deposition .....	23
1.2.3. Hydrothermal/solvothermal synthesis.....	24
1.3. Electrochemical water splitting.....	31
2. MATERIALS AND METHODS .....	35
2.1. Materials and chemicals.....	35
2.2. Substrate preparation.....	35
2.3. Anodizing of titanium substrates .....	36
2.4. Molybdenum disulfide synthesis.....	36
2.5. Electrochemical measurements.....	37
2.6. Characterization of synthesized MoS <sub>2</sub> films .....	38
3. RESULTS AND DISCUSSION.....	40
3.1. Synthesis and characterization of MoS <sub>2</sub> /Glycine films .....	40
3.1.1. Morphology of MoS <sub>2</sub> /Glycine films .....	40

3.1.2. Characterization of MoS <sub>2</sub> /Glycine films .....	42
3.1.3. Investigation of MoS <sub>2</sub> /Glycine electrode HER performance .....	44
3.2. Molybdenum disulfide films hybridized with L-cysteine .....	47
3.2.1. Morphology of MoS <sub>2</sub> /Cysteine films .....	47
3.2.2. Characterization of fabricated MoS <sub>2</sub> /Cysteine films.....	48
3.2.3. Electrochemical HER performance of fabricated MoS <sub>2</sub> /Cysteine electrodes.....	52
3.2.4. Insight into possible intercalation of L-cysteine .....	53
3.3. Investigation of MoS <sub>2</sub> /Histidine electrochemical HER performance	55
3.3.1. Morphology of MoS <sub>2</sub> /Histidine films .....	55
3.3.2. Electrochemical investigations of MoS <sub>2</sub> /Histidine electrodes .....	56
3.3.3. Characterization of MoS <sub>2</sub> /Histidine films .....	61
3.4. Improving the HER performance of hydrothermally synthesized MoS <sub>2</sub> via anodic pretreatment .....	63
3.4.1. Anodic pretreatment and electrochemical investigation of MoS <sub>2</sub> /Cysteine electrodes.....	64
3.4.2. Characterization of anodically pretreated MoS <sub>2</sub> /Cysteine electrodes	68
3.4.3. Influence of annealing on the MoS <sub>2</sub> /Cysteine electrodes and their activation via anodic pretreatment.....	72
3.4.4. Investigation of HER stability of anodically pretreated MoS <sub>2</sub> /Cysteine electrodes.....	75
3.5. Activity comparison of hydrothermally synthesized MoS <sub>2</sub> /amino acid electrodes.....	79
<b>CONCLUSIONS .....</b>	<b>80</b>
<b>SANTRAUKA .....</b>	<b>81</b>
<b>ĮVADAS .....</b>	<b>81</b>
<b>DARBO TIKSLAS .....</b>	<b>82</b>
<b>DARBO UŽDAVINIAI .....</b>	<b>82</b>
<b>MOKSLINIS NAUJUMAS .....</b>	<b>82</b>
<b>GINAMIEJI TEIGINIAI .....</b>	<b>83</b>
<b>AUTORIAUS INDĖLIS .....</b>	<b>83</b>

4. EKSPERIMENTO METODIKA.....	84
5. TYRIMO REZULTATAI.....	86
5.1. MoS <sub>2</sub> /Glicino dangų sintezė ir charakterizavimas .....	86
5.1.1. MoS <sub>2</sub> /Glicino dangų morfologija.....	86
5.1.2. MoS <sub>2</sub> /Glicino dangų charakterizavimas.....	86
5.1.3. MoS <sub>2</sub> /Glicino elektrodų HER savybių tyrimas .....	88
5.2. MoS <sub>2</sub> dangos su L-cisteinu.....	89
5.2.1. MoS <sub>2</sub> /Cisteino dangų morfologija.....	89
5.2.2. Susintetintos MoS <sub>2</sub> /Cisteino dangos charakterizavimas .....	90
5.2.3. MoS <sub>2</sub> /Cisteino elektrodų HER savybių tyrimas .....	91
5.2.4. Ižvalgos apie galimą L-cisteino įsiterpimą.....	92
5.3. MoS <sub>2</sub> /Histidino dangų elektrocheminių HER savybių tyrimas.....	93
5.3.1. MoS <sub>2</sub> /Histidino dangų morfologija.....	93
5.3.2. MoS <sub>2</sub> /Histidino elektrodų elektrocheminiai tyrimai .....	93
5.3.3. MoS <sub>2</sub> /Histidino dangų charakterizavimas.....	95
5.4. Elektrocheminių HER savybių pagerinimas anodiškai apdorojant hidrotermiškai susintetintą MoS <sub>2</sub> .....	96
5.4.1. MoS <sub>2</sub> /Cisteino elektrodų anodinis apdorojimas ir elektrocheminiai matavimai .....	97
5.4.2. Anodiškai apdorotų MoS <sub>2</sub> /Cisteino elektrodų charakterizavimas.....	98
5.4.3. Atkaitinimo įtaka MoS <sub>2</sub> /Cisteino elektrodams ir jų aktyvavimas anodiniu apdorojimu.....	101
5.4.4. MoS <sub>2</sub> /Cisteino elektrodo HER stabilumo tyrimas po anodinio apdorojimo .....	101
IŠVADOS.....	104
CURRICULUM VITAE .....	105
LIST OF PUBLICATIONS.....	106
Publications for doctoral dissertation .....	106
Other publications .....	106
Conference reports .....	106
REFERENCES .....	108

## INTRODUCTION

Energy has always been the backbone of human civilization and has played a vital role in the advancement of almost every aspect of our lives, from basic survival to the development of technology and subsequent shaping of the modern world. With the rapid growth of global population, and the ceaseless strive for progress, the global energy demand increases almost exponentially. This raises a few concerns, foremost among them being the current dependence on fossil fuels for energy production [1]. Combustion of fossil fuels results in the emission of excessive amounts of methane CH<sub>4</sub>, carbon dioxide CO<sub>2</sub>, and nitrous oxide N<sub>2</sub>O gasses, collectively called greenhouse gasses. The greenhouse effect, exacerbated by these gasses, induces global warming, resulting in changes of the ecosystems, abnormal weather patterns, and the rise of sea-level [2]. Therefore, the search and development of sustainable alternatives for fossil fuels is of utmost importance, and one of the proposed alternatives in consideration is hydrogen fuel [3].

Hydrogen is particularly attractive as a fuel due to its high gravimetric energy density (3 times higher than fossil fuels) and zero carbon emissions [4, 5]. Only <1% of hydrogen is present on Earth as hydrogen gas H<sub>2</sub>, however, and most commonly employed (~90-95% of total H<sub>2</sub> produced) hydrogen production methods, such as steam methane reforming, partial oxidation of hydrocarbons or coal gasification use fossil fuels and release significant amounts of greenhouse gasses during H<sub>2</sub> production [6, 7]. A more sustainable method of producing hydrogen is obtaining it from water via water electrolysis. Water electrolysis involves splitting of water molecules into their constituent components, hydrogen and oxygen, via hydrogen and oxygen evolution reactions [8]. The produced hydrogen could be considered “green” if the electricity required for the hydrogen evolution reaction (HER) were to be obtained from renewable sources [9], therefore water splitting shows great promise as an alternative and sustainable method of hydrogen production. However, a suitable electrocatalyst is needed in order to facilitate HER and achieve a significant amount of generated hydrogen gas. Currently, scarce and costly noble-metal catalysts like Pt, RuO<sub>2</sub> or IrO<sub>2</sub> are considered the best electrocatalysts of HER [10, 11], prompting the development of novel, non-noble metal electrocatalysts for HER which would be more sustainable and commercially available.

Recently, much effort has been put into development of alternative, earth-abundant electrocatalysts for OER and HER. Transition metal phosphates [12], oxides [13], hydroxides [14], perovskites [15], and chalcogenides [16, 17] are being investigated for their application as OER electrocatalysts.

Meanwhile, materials such as transition metal phosphides [18], carbides [19], nitrides [20], and chalcogenides [21] are considered as potential HER electrocatalysts. Transition metal dichalcogenide  $\text{MX}_2$  nanomaterials (M – transition metal, X – chalcogenide), and in particular molybdenum disulfide  $\text{MoS}_2$ , has garnered significant attention for their potential application in hydrogen generation [22] owing to their layered two-dimensional structure and nano-scale thickness, which give rise to peculiar chemical, physical, or electronic properties compared to their bulk counterparts [23, 24].  $\text{MoS}_2$  nanomaterials possess nearly neutral Gibbs free energy of hydrogen adsorption ( $\Delta G_{\text{H}^*}$ ), which is only slightly higher than that of Pt [25], making it a promising alternative. However, a few challenges, namely, the scalable and feasible synthesis of  $\text{MoS}_2$  nanomaterials, the increase of HER activity and electrocatalyst stability, and integration of  $\text{MoS}_2$  nanomaterials into practical water electrolysis systems ought to be overcome for these materials to become commercially viable options for hydrogen production.

## MAIN GOAL

To investigate the influence of amino acid additives on the enhancement of activity and stability of hydrothermally synthesized nanoplatelet-shaped  $\text{MoS}_2$  electrodes for hydrogen evolution reaction and determine the nature of the most active HER sites on fabricated  $\text{MoS}_2$ .

## TASKS

- To fabricate  $\text{MoS}_2$  films with glycine, L-cysteine and DL-histidine amino acids and study the influence of amino acid additives on the electrocatalytic HER activity and stability.
- To characterize  $\text{MoS}_2$ /amino acid films and explore possible intercalation of guest species into the interlayers of  $\text{MoS}_2$ .
- To investigate the effects of anodic pretreatment on hydrothermally synthesized  $\text{MoS}_2$  electrodes.
- To distinguish the HER active sites of  $\text{MoS}_2$  and assess the increase of active site relative content after anodic pretreatment.

## SCIENTIFIC NOVELTY

- The influence of amino acids on the hydrothermal synthesis of molybdenum disulfide was investigated for the first time. It was determined, that the addition of amino acids to the ammonium heptamolybdate and thiourea solution results in the formation of nanoplatelet MoS<sub>2</sub> films with a relatively high content of metastable, metallic 1T-MoS<sub>2</sub> phase during the hydrothermal synthesis.
- It was established for the first time that hydrothermally synthesized MoS<sub>2</sub> films with amino acids possess higher electrocatalytic HER activity and stability, compared to MoS<sub>2</sub> films, fabricated without amino acids due to formation and insertion of amino acid fragments.
- A novel method of increasing the electrocatalytic activity of molybdenum disulfide electrode via anodic pretreatment was determined and investigated. It was distinguished that during anodic pretreatment the relative quantity of catalytically active bridging S<sub>2</sub><sup>2-</sup> groups is increased.

## STATEMENTS OF DEFENCE

- Hydrothermally synthesized MoS<sub>2</sub> films with amino acid additives exhibit enhanced hydrogen evolution reaction activity and stability, compared to hydrothermally synthesized MoS<sub>2</sub> films without amino acids.
- Increase in activity and stability of MoS<sub>2</sub>/amino acid electrodes is linked with the formation of metastable 1T-MoS<sub>2</sub> phase due to intercalation of charged guest species or fragments between neighbouring nanoplatelets.
- Increase in electrocatalytic activity of MoS<sub>2</sub>/amino acid electrode is achieved via anodic pretreatment by increasing the relative content of bridging S<sub>2</sub><sup>2-</sup> groups, which are considered as the active sites for hydrogen evolution, during anodic processing.

## CONTRIBUTIONS OF AUTHOR

Preparation of substrates, anodizing of Ti and hydrothermal synthesis of MoS<sub>2</sub> films and powders described herein were carried out by the author of this dissertation. All samples for the experiments reported in this work were fabricated by the author. The author also performed HER measurements of synthesized MoS<sub>2</sub> films via cyclic voltammetry and chronopotentiometry, as well as anodic pretreatment and electrochemical measurements of pretreated

electrodes. Furthermore, the author carried out the deconvolution and fitting of XPS spectra, analysis of other obtained results, designing their graphs and figures, and preparing all publications listed below. The author wrote this dissertation himself, with proper referencing employed for all information obtained from sources other than the original works of the author.

## 1. LITERATURE REVIEW

### 1.1. Properties of molybdenum disulfide

#### 1.1.1. MoS<sub>2</sub> structure and polytypes

Molybdenum disulfide is a layered 2D structure transition metal dichalcogenide (TMD), with each individual layer consisting of a plane of molybdenum atoms sandwiched in between two planes of sulfur atoms, with the average layer thickness of 0.65 nm [26]. The atoms in one S-Mo-S layer are bonded together predominantly by covalent bonds, while interlayer bonding stems from weak van der Waals forces [27]. MoS<sub>2</sub> has three main polytypes: 1T with trigonal structure symmetry, hexagonal 2H, and rhombohedral 3R, with the digits indicating the number of layers in a unit cell (Fig. 1.1. a-f). In each individual layer, the Mo atom is coordinated by six S atoms (Fig. 1.1. g, h) and the Mo-S coordination is octahedral in 1T, while in 2H and 3R the coordination is trigonal prismatic [28]. The 2H phase is thermodynamically stable and is the main naturally occurring phase, while 3R and 1T are both metastable, with only small amounts of 3R found in nature [29], and 1T phase is only obtained synthetically. Both 2H and 3R phases are semiconducting and bulk MoS<sub>2</sub> crystals are indirect band gap (1.3 eV) semiconductors [30], while a monolayer of MoS<sub>2</sub> is a direct band gap (1.8 eV) semiconductor [31, 32]. Contrarily, the 1T phase is metallic and paramagnetic due to two spin-parallel 4d electrons located in d<sub>xy</sub>, d<sub>xz</sub>, and d<sub>yz</sub> orbitals in octahedral coordination, while two spin-antiparallel electrons occupy d<sub>z<sup>2</sup></sub> orbital in trigonal prismatic coordination (2H and 3R) and are thus diamagnetic [33-35]. The conductivity of 1T phase is reported to be ~10<sup>7</sup> times higher than the conductivity of semiconducting 2H or 3R phases [36]. Being thermodynamically metastable, 1T phase gradually transforms to the stable 2H polytype in ambient conditions [37], and quite readily when heated to 100 °C [38]. However, Chhowalla's group described a linear increase in 2H phase fraction up to 150 °C when heating chemically exfoliated 1T-MoS<sub>2</sub>, and XPS analysis determined that predominantly 2H phase was obtained only when annealing was carried out at 300 °C [39].

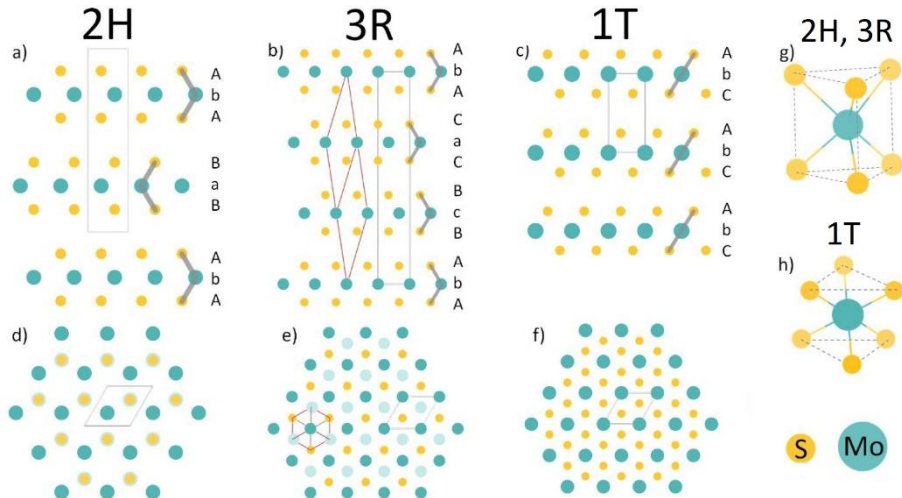


**Figure 1.1.** Schematic illustration of the crystal structures for the most common MoS<sub>2</sub> polytypes: 2H (a, d), 3R (b, e), and 1T (c, f). Side-view from the a-axis (a-c) and bilayer top-views from the c-axis (d-f) show the unit cell, layer directions, and stacking sequence (a-c). Mo-S trigonal prismatic (2H, 3R) and octahedral (1T) coordination schematic illustrations are displayed in (g, h). In the portrayed stacking sequences (a-c), uppercase letters indicate S atoms, while lowercase letters indicate Mo atoms [40].

Several approaches to achieve the 2H to 1T phase transformation have been reported. One of the commonly used methods is alkali metal intercalation into the interlayers of MoS<sub>2</sub>, inducing the transition from 2H to 1T [41]. Phase transition by generating sulfur vacancies was also reported by Cai *et al.* [42]. Charge injection and strain effects were also employed for the formation of 1T phase from 2H-MoS<sub>2</sub> [43, 44]. The 2H → 1T phase transition could be visualized as a clockwise 60° rotation of S atoms with respect to the central Mo atom, resulting in the misalignment of S atom planes (Fig. 1.2. a-b), with the upper or lower S plane gliding resulting in octahedral coordination of Mo [45, 46]. Further distortion of 1T phase results in the formation of 1T' phase, where Mo atoms form a zigzag chain in a distorted octahedral structure (Fig. 1.2. c). There are contradicting reports about 1T' phase properties, as some report that it possesses slightly higher conductivity than 1T [47], while it is described as a semiconductor with ~0.09 eV band gap in other reports [48].

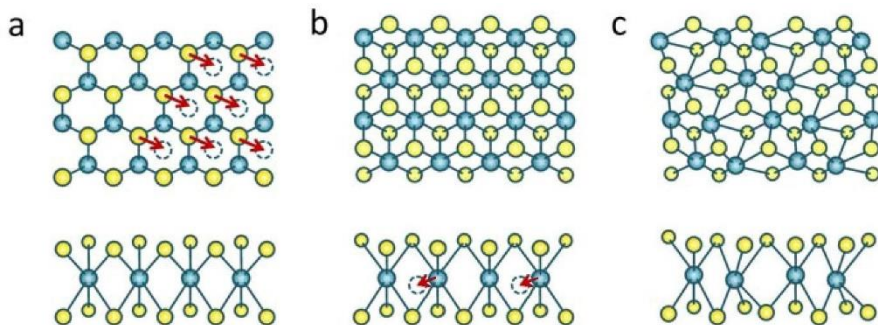


**Figure 1.2.** Schematic illustration of 2H (a), 1T (b), and 1T' (c) structures, observed from c-axis (upper) and a-axis (lower). Only the upper plane S atoms are seen for 2H structure, since the lower plane S atoms are precisely underneath. The S plane glide motion, depicting 2H→1T transformation is depicted by red arrows (a,b), and the motion of Mo atoms for 1T' phase is depicted in (b, c) [45].

Stable polytypes of  $\text{MoS}_2$  have been used for lubrication in extreme conditions [49] due to their chemical inertness as well as weak van der Waals forces holding the layers together and enabling the layers to slide on top of one another [50].  $\text{MoS}_2$  is also commonly employed as a hydrodesulfurization catalyst in petrochemistry, where it is used to remove sulfur in various petroleum products [51]. The semiconducting properties of 2H phase find application in various fields such as solar cells [52], batteries [53], gas sensors [54], field-effect transistors [55], or flexible electronics [56]. Owing to the broken inversion symmetry, the 3R phase displays outstanding nonlinear optical properties with promising applications [57]. The presence of a metallic 1T phase eliminates the Schottky barrier when in contact with metals, thus enhancing the charge transfer, thereby providing distinct benefits in electrochemical applications [43].

### 1.1.2. Characterization of $\text{MoS}_2$

The existence of various polytypes of molybdenum disulfide and the possibility of obtaining different structures via numerous synthesis routes gives rise to various diverse properties, greatly expanding the potential for application in different fields, albeit unambiguous characterization of molybdenum disulfide and determination of polytype is of utmost importance. A few of the most used methods for  $\text{MoS}_2$  characterization are highlighted below.

Scanning electron microscopy (SEM) is widely used for the determination of bulk MoS<sub>2</sub> morphology as it is readily accessible and works well with both conducting and semiconducting MoS<sub>2</sub> samples. SEM can be utilized in examining sample degradation by analyzing the samples before and after processing or natural degradation during storage [58]. Similarly, SEM can assist in controlling the synthesis parameters by investigating the morphology of samples fabricated with different synthesis parameters or intermediate products when stepwise syntheses are carried out [59, 60].

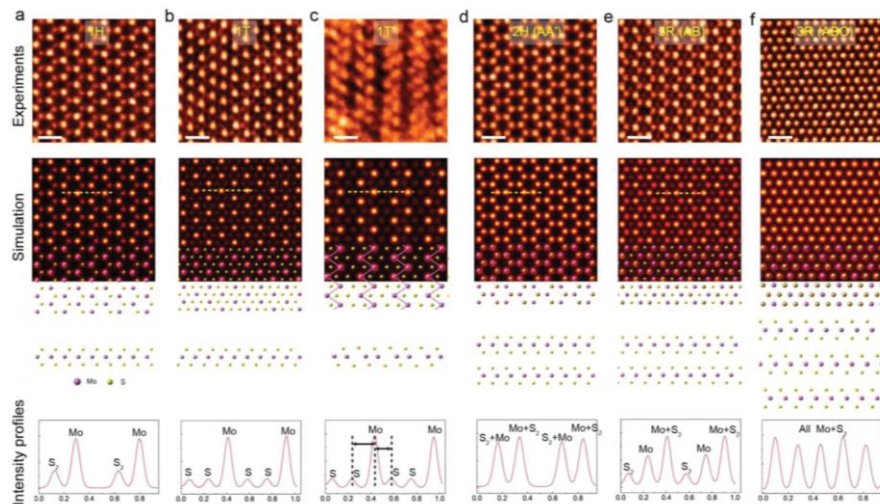


**Figure 1.3.** HAADF-STEM images and simulated images with atomic models of monolayer: a) 1H, b) 1T, c) 1T', d) bilayer 2H (AA'), e) bilayer 3R (AB)-stacked, and f) trilayer 3R (ABC)-stacked MoS<sub>2</sub>. Depicted below are the intensity profiles of each atomic model. The scale bars in HAADF-STEM images are 0.5 nm [61].

High-resolution transmission electron microscopy (HRTEM) and high-angle annular dark-field scanning transmission electron microscopy (HAADF-STEM) enables the examination of mono- or few-layered MoS<sub>2</sub> materials (Fig. 1.3.). A repeating hexagonal structure, with a gap in the center, is observed for the 2H phase with Mo atoms appearing slightly brighter than S atoms (Fig. 1.3. d). Meanwhile, only a series of Mo atoms in a closer packed trigonal lattice is observed for the 1T phase (Fig. 1.3. b) as the intensity of S is much lower due to the misalignment of S atoms in the upper and bottom planes [62]. 3R phase is also feasibly distinguished (Fig. 1.3. f), as Mo and both S atoms provide uniform intensity profiles due to AbA CaC BcB stacking [61]. TEM is also routinely employed for the evaluation of interlayer spacing, nanosheet thickness, and the number of layers present [63, 64].

X-ray diffraction (XRD) is used for the evaluation of sample crystallinity, as crystalline materials give rise to sharp peaks, whereas broad peaks of lower intensity are observed for amorphous materials. MoS<sub>2</sub> is routinely investigated by XRD using Cu K<sub>α</sub> X-ray source and the major peak is ascribed to the (002) reflection with  $2\theta \approx 14.4$  deg for 2H-MoS<sub>2</sub>, which corresponds to the lattice spacing of 6.1 Å [65]. Determination of 1T phase via XRD is not straightforward. There are reports of a new (001) peak appearing at  $2\theta \approx 7.3$  deg, which is presumed to be an indication of a metallic phase with a reported *d*-spacing of ~11.8 Å [36, 66]. Other reports describe the shift of the (002) peak of 2H-MoS<sub>2</sub> to lower  $2\theta$  values as the interlayer is expanded via intercalation, where the magnitude of interlayer expansion, and consequently, the shift of (002) peak depends on the size of intercalated species [67]. Because phase transformation from 2H to 1T usually involves intercalation, the possibility of both (001) of 1T and (002) of 2H peaks coexisting as only part of 2H is transformed to 1T and the fact that other *hkl* peaks are found in both phases with minimal shift, characterization of phase via XRD is difficult and therefore should be supplemented by other techniques.

The composition of fabricated MoS<sub>2</sub> materials, as well as phase content, can be evaluated using X-ray photoelectron spectroscopy (XPS). In the Mo 3d spectrum, the doublet of 2H-MoS<sub>2</sub> is observed at binding energies of 229.4 eV for 3d<sub>5/2</sub> and 232.5 eV for 3d<sub>3/2</sub> [68], while 1T-MoS<sub>2</sub> doublet resides at binding energies of 228.5 eV and 231.6 eV for 3d<sub>5/2</sub> and 3d<sub>3/2</sub>, respectively [39]. Variations of 3d doublet binding energy are reported and mostly occur due to different sample fabrication, however, the separation between 2H and 1T is generally accepted to be ~0.9 eV, with the peaks corresponding to the 1T located at lower binding energy than those of 2H [69-71]. In addition to the peaks attributable to Mo<sup>+4</sup>, peaks from higher oxidation states can be observed in the 3d spectrum of Mo. Peaks at ~232.6 eV are ascribed to Mo<sup>+6</sup>, which is usually from MoO<sub>3</sub> [72], thus providing an insight into sample degradation. Peaks for Mo<sup>+5</sup> [73] or Mo<sup>+4</sup> oxysulfides [74] at a binding energy of ~230.3 eV are also observed. Similarly, an approximately 0.9 eV shift between 1T and 2H phases is observed in the sulfur S 2p spectrum [75]. 2p<sub>3/2</sub> peaks at 162.4 eV and 161.6 eV are ascribed to 2H and 1T, respectively, while corresponding 2p<sub>1/2</sub> peaks appear at higher by 1.16 eV binding energies.

Visible light techniques are also used for MoS<sub>2</sub> phase confirmation. Raman spectroscopy is employed to study lattice vibrations, where characteristic phonon modes for different crystal structures are observed. Bulk (2H) MoS<sub>2</sub> Raman spectrum consists of four active modes: E<sup>2g</sup> (32 cm<sup>-1</sup>), E<sub>1g</sub> (281 cm<sup>-1</sup>), E<sup>1g</sup> (379 cm<sup>-1</sup>), and A<sub>1g</sub> (405 cm<sup>-1</sup>) [76]. However, the obtained Raman spectra, i.e. which modes are detected, depend on the excitation

wavelength. Placidi *et al.* obtained Raman spectra of mechanically exfoliated 2H-MoS<sub>2</sub> nanosheets using different wavelength excitation, from ultraviolet (325 nm) to infrared (1064 nm) [77]. It was determined that two modes, namely E<sup>1</sup><sub>2g</sub> and A<sub>1g</sub>, were observed regardless of wavelength used and are now generally accepted as the two dominant features of MoS<sub>2</sub> Raman spectra. The E<sup>1</sup><sub>2g</sub> mode arises from the in-plane vibration of S atoms in one direction and the vibration of Mo atom in another direction, while vibrations in adjacent layers are out of phase. The A<sub>1g</sub> mode stems from out-of-plane stretching of S atoms, where the vibrations of S atoms are in opposite directions [78]. Analysis of these two peaks can also give an approximation of the layer thickness based on the wavenumber difference ( $\Delta\bar{v}$ ) of these peaks as E<sup>1</sup><sub>2g</sub> blueshifts and A<sub>1g</sub> redshifts when the number of layers decreases from 5 to 1; for more than 5 layers  $\Delta\bar{v}$  becomes indistinguishable from bulk MoS<sub>2</sub> [76]. Raman spectroscopy also enables the identification of 2H and 1T phases. 2H → 1T conversion leads to a considerable decrease or disappearance of the E<sup>1</sup><sub>2g</sub> and A<sub>1g</sub> peaks altogether, with the emergence of three peaks, which are not seen in 2H phase: J<sub>1</sub> (147 cm<sup>-1</sup>), J<sub>2</sub> (222 cm<sup>-1</sup>), and J<sub>3</sub> (333 cm<sup>-1</sup>) [79, 80]. In some cases, only the E<sup>1</sup><sub>2g</sub> peak disappears, while a low-intensity A<sub>1g</sub> peak could be observed. Moreover, the E<sub>1g</sub> (281 cm<sup>-1</sup>) becomes more pronounced in the 1T phase, even though it can also appear in the 2H phase [81]. Due to similarities between 1T-MoS<sub>2</sub> and MoO<sub>3</sub> Raman spectra [82], care should be taken when determining the phase of MoS<sub>2</sub> via Raman spectroscopy, as high energy irradiation may lead to the oxidation of MoS<sub>2</sub>, subsequently increasing MoO<sub>3</sub> content [83]. Photoluminescence spectroscopy is also a viable technique for determining whether the MoS<sub>2</sub> sample is metallic or semiconducting. A photoluminescence spectrum with two peaks at ~630 nm and ~670 nm is observed for few-layered semiconducting 2H-MoS<sub>2</sub>, and the photoluminescence intensity is influenced by the number of layers, as it is significantly higher for monolayered 2H-MoS<sub>2</sub> than the photoluminescence intensity of 2 to 4 layers of MoS<sub>2</sub> [76]. In contrast, the metallic 1T-MoS<sub>2</sub> has no band gap and therefore does not exhibit photoluminescence, as was detailed by Zhu *et al.* [84]. In their work, a patterned polymethyl methacrylate (PMMA) mask was placed on a 2H-MoS<sub>2</sub> sample, which was then subjected to Ar plasma treatment, resulting in 2H → 1T phase transition at unmasked areas of the sample. The emergence of J<sub>1</sub>, J<sub>2</sub>, and J<sub>3</sub> was observed in the Raman spectrum of exposed regions and the photoluminescence was gradually quenched with respect to the duration of plasma treatment. Meanwhile, only the E<sup>1</sup><sub>2g</sub> and A<sub>1g</sub> Raman peaks were observed at the masked regions which exhibited intense photoluminescence, therefore confirming that the masked

regions were of 2H phase, while a phase transition to 1T occurred at unmasked regions subjected to plasma treatment.

## 1.2. Synthesis of molybdenum disulfide nanomaterials

$\text{MoS}_2$  is naturally found as a crystalline mineral molybdenite, a rather abundant mineral similar in appearance to graphite, or jordisite, a much rarer amorphous mineral. Relatively pure  $\text{MoS}_2$  is produced via froth flotation of molybdenite ore [85]. However, for application in electrocatalysis, nanomaterials of  $\text{MoS}_2$  are preferred, and most of the publications surrounding  $\text{MoS}_2$  as a catalyst for HER make use of various nanomaterial synthesis methods and the  $\text{MoS}_2$  catalysts are usually comprised of nanomaterials.

As is the case for other layered materials, the two main approaches for the synthesis of molybdenum disulfide nanomaterials are top-down and bottom-up approaches [86]. Top-down synthesis methods involve reducing the dimensions of bulk  $\text{MoS}_2$  materials into nanoscale-sized materials by various mechanical methods. Bottom-up approaches employ chemical reactions, during which the growth of  $\text{MoS}_2$  nanomaterials starts from atoms or molecules, producing various molybdenum disulfide nanostructures.

By using different methods of synthesis, a plethora of molybdenum disulfide nanostructures could be obtained with diverse physical and chemical properties. Thus, the HER activity and stability of  $\text{MoS}_2$  strongly depend on the choice of synthesis method.

### 1.2.1. Exfoliation of $\text{MoS}_2$

As mentioned previously, molybdenum disulfide has a layered structure, where adjacent layers are held together by van der Waals interactions. Hence,  $\text{MoS}_2$  nanolayers can be obtained using the so-called ‘scotch-tape’ or mechanical exfoliation technique, as was first demonstrated by Novoselov *et al.* [87]. In essence, bulk  $\text{MoS}_2$  crystals are micromechanically cleaved by repeated application of an adhesive tape, resulting in few-layered flakes, which are then transferred onto a Si wafer. Obtained flakes are of high purity with few defects and retain the same crystal structure as the bulk crystal since during mechanical exfoliation no chemical reactions take place [88]. Ottaviano *et al.* fabricated  $\text{MoS}_2$  nanoflakes via mechanical exfoliation onto  $\text{SiO}_2/\text{Si}$  wafer and reported that by using optical microscopy and atomic force microscopy along with Raman and photoluminescence spectroscopies, the

number of obtained layers could be precisely characterized [89]. The mechanical exfoliation technique is fairly simple and applicable to any large layered crystal material. However, it requires intensive labour in order to obtain single layers. Furthermore, it is hindered by a lack of scalability and control of obtained nanomaterial dimensions, making it feasible only for laboratory purposes [88, 90].

Another prevalent category of exfoliation techniques is liquid phase exfoliation (LPE). During LPE, powders of bulk layered material are added to a liquid medium, and exfoliation is achieved using ultrasonic or shear energy. Then, the nanosheets are separated from unexfoliated material by centrifugation of obtained dispersion [91]. A process called cavitation occurs in liquid media subjected to ultrasonic waves, where microbubbles or voids form and collapse in the liquid [90]. As the cavitation bubbles collapse, shock waves and jets of liquid act on the bulk material, leading to the exfoliation of the layer. However, high local temperatures and pressures during cavitation may lead to fragmentation or an increase of defects in exfoliated nanolayers [92].

During solvent-assisted exfoliation, layered bulk crystals are exfoliated by ultrasonication in organic solvents. Matching the surface tension of the organic solvent with the surface energy of layered material facilitates the overcoming of interlayer van der Waals interaction. Additionally, the resultant nanosheet dispersions are stabilized via solvent-nanosheet interaction [93]. The choice of organic solvent could also determine the structure of obtained nanomaterials, as Dong *et al.* demonstrated that by using a mixture of H<sub>2</sub>O<sub>2</sub> and 1-methyl-2-pyrrolidone, porous MoS<sub>2</sub> nanosheets were obtained [94]. Solvent-assisted exfoliation is a relatively straightforward method, albeit obtaining nanosheets with uniform thickness and lateral size is difficult [95]. Moreover, the best solvents for exfoliation are usually toxic, and complete removal of organic solvent is crucial prior to coating a substrate with obtained nanoflakes [96]. A more environmentally friendly LPE technique is surfactant-assisted exfoliation. In this case, rather than using organic solvents, the exfoliation is performed using aqueous solutions of surfactants. The surface tension of the liquid media can be tuned by using surfactant molecules, thus promoting exfoliation and stabilizing the resultant nanosheets. Restacking of obtained nanosheets is prevented by the adsorption of surfactant molecules on the nanosheet surface [97]. Generally, nanosheets obtained via surfactant-assisted exfoliation retain the structure of the bulk crystal, although, in the work of Zhao *et al.*, very small quantum dots stabilized by a polymeric surfactant with more than 80% of the metastable 1T phase were reported [98]. Exfoliation could also be carried out in pure water by controlling the

temperature, as described by Kim *et al.* [99]. The temperature was controlled by adjusting the cooling of the sonic bath, with the heat generated from the dissipation of sonic energy being sufficient for exfoliation. Characterization of obtained MoS<sub>2</sub> by XPS, Raman, and PL spectroscopies revealed that pristine 2H-MoS<sub>2</sub> monolayers were formed. Nevertheless, Bodik and coworkers argue that water molecules may facilitate oxidation of few-layered MoS<sub>2</sub> and thus exfoliation in water may result in increased content of MoO<sub>x</sub> and MoO<sub>3</sub> phases [100]. The main drawbacks of LPE are a lack of scalability and poor control over both the lateral size and the number of layers present in obtained nanosheets [101]. The process is also hindered by long sonication times and the use of liquid media itself. In solvent-assisted exfoliation, this hindrance is the removal of organic high-boiling point solvents, while nanosheets obtained via surfactant-assisted exfoliation require post-treatment in order to remove the adsorbed surfactants that stabilize the nanosheets and prevent their re-agglomeration [102]. To overcome the issue of scalability shear-mixing exfoliation, an alternative method to exfoliation with ultrasonic waves, was described by Paton *et al.* [103]. Instead of using ultrasonic waves, exfoliation is carried out by high-shear mixing of liquid medium, resulting in large quantities of unoxidized, defect-free nanosheets. It was demonstrated that exfoliation could be achieved if the local shear rate exceeds a critical value of 10<sup>4</sup> s<sup>-1</sup>, which, according to the authors, can be achieved with a variety of mixers, including household kitchen blenders. Shear exfoliation is shown to be more efficient than sonication-induced exfoliation, with the difference in efficiency being more pronounced with increasing volume.

Another prominent technique for the exfoliation of layered materials is ion intercalation. During this process, various species are intercalated in the gaps of MoS<sub>2</sub> layers, thus expanding the interlayer distance. An external driving force, like ultrasonication, then separates the layers [104]. Joensen *et al.* first described the exfoliation of MoS<sub>2</sub> with n-butyllithium [105]. In their work, bulk MoS<sub>2</sub> powder was soaked in a solution of n-BuLi in hexane for 48 h., and the resultant Li<sub>x</sub>MoS<sub>2</sub> powder was immersed in water and ultrasonicated. It was determined that exfoliation occurs due to the evolution of H<sub>2</sub> gas, which forms due to a reaction of Li with water, while sonication was shown to improve exfoliation and promote the formation of monolayers. Later, it was shown that high concentrations of intercalated Li promote the phase change of obtained MoS<sub>2</sub> nanomaterial from 2H to 1T, which was claimed to be irreversible [106]. Chhowalla's group reported that Li exfoliation results in a predominantly metallic metastable 1T phase for as-exfoliated MoS<sub>2</sub> [39], however, annealing restores the semiconducting phase. Moreover, after annealing the exfoliated material above 300 °C band gap

photoluminescence was observed, indicating that the exfoliated nanosheets consist of semiconducting monolayers. The possibility to obtain the 1T phase makes ion intercalation more suitable than other exfoliation methods for the synthesis of MoS<sub>2</sub> electrocatalysts. Yin *et al.* fabricated porous 1T-MoS<sub>2</sub> nanosheets via liquid-ammonia-assisted lithiation by placing bulk MoS<sub>2</sub> powder with Li metal in a test tube, filled with ammonia gas [107]. After intercalation, the ammonia gas was evaporated and exfoliation of MoS<sub>2</sub> was carried out in deionized water. Their findings show that both porous 1T and conventional 1T, obtained with n-BuLi exfoliation, possess superior HER activity than exfoliated 2H-MoS<sub>2</sub>.

### 1.2.2. Chemical/physical vapour deposition

Chemical vapour deposition is a frequently used method for the synthesis of MoS<sub>2</sub> films with various thicknesses and lateral sizes. CVD is typically carried out by one of three routes: (1) sulfurization of deposited Mo metal layer by S precursor, (2) sulfur vapour reaction with MoO<sub>3-x</sub>, and (3) thermal decomposition of ammonium thiomolybdate. A report by Zhan describes the first route [108]: Mo thin film, deposited on SiO<sub>2</sub> substrate was placed in a quartz tube furnace. Pure sulfur was placed in the low-temperature zone of the quartz tube, which was kept slightly above the melting point of sulfur. The temperature is gradually raised to 750 °C. Sulfur vapour reacts with the Mo film, forming a thin MoS<sub>2</sub> film. The thickness and size of MoS<sub>2</sub> are directly related to the parameters of pre-deposited Mo metal, making this method highly scalable. In a similar fashion, Lee *et al.* fabricated MoS<sub>2</sub> films on Si/SiO<sub>2</sub> substrates by sulfurization of MoO<sub>3</sub>. Powders of sulfur and MoO<sub>3</sub> were placed in a quartz tube, along with the substrate. By heating to 650 °C MoO<sub>3</sub> powder was reduced to MoO<sub>3-x</sub> by sulfur vapour. Volatile suboxide then reacted with sulfur vapour to form crystalline MoS<sub>2</sub> on the substrate. The authors infer substrate pre-treatment with graphene-like molecules facilitates MoS<sub>2</sub> layer growth [109]. A MoS<sub>2</sub>/graphene hybrid heterostructure was described by Shi *et al.* using ammonium thiomolybdate solution in DMF as a precursor for MoS<sub>2</sub> [110]. Graphene was first deposited on Cu foil via CVD, then ammonium thiomolybdate was carried to the substrate by Ar gas flow. After annealing at 400 °C, MoS<sub>2</sub> layers formed on the graphene surface were shown to have high crystallinity and an abundant quantity of edge sites, which are favourable for electrocatalysis. Thermal decomposition of ammonium thiomolybdate may also lead to the formation of amorphous MoS<sub>x</sub>, as reported by Hsu *et al.* Carbon cloths were immersed in a solution of ammonium

thiomolybdate in DMF and were annealed in a CVD furnace at 120 °C in H<sub>2</sub>/Ar environment. Characterization of obtained molybdenum sulfide catalyst revealed that obtained material is indeed amorphous, as no Raman or XRD features were observed. Additionally, by adding NbCl<sub>5</sub> to the synthesis solution, obtained electrocatalysts attain even greater HER activity. XPS revealed that the addition of NbCl<sub>5</sub> affects the structure of MoS<sub>x</sub>, as almost no peaks are seen for Nb, whereas an increase in unsaturated sulfur S<sub>2</sub><sup>2-</sup> content is observed and correlates with the enhancement of HER [111].

Physical vapour deposition is seldom used to fabricate MoS<sub>2</sub> electrocatalysts, as the method is better suited for the synthesis of single-crystal semiconductor materials. By using molecular beam epitaxy, high-quality monolayers of TMDs could be fabricated with the ability to control the thickness and doping of obtained thin films [112]. Magnetron sputtering method enables the synthesis of MoS<sub>2</sub> films with various properties, ranging from those similar to exfoliated materials [113, 114], to amorphous MoS<sub>2</sub> [115], or MoS<sub>2</sub>-Ti composites [116]. Zhang *et al.* reported the fabrication and investigation of amorphous MoS<sub>2</sub> electrocatalyst film on carbon cloth [115]. According to the authors, by using magnetron sputtering power of 100 W at 3 mtorr pressure, dense MoS<sub>2</sub> nanosheet arrays were formed on a carbon cloth substrate. Lower sputtering power was found to yield short and sparsely distributed nanostructures, whereas a much smoother film-like surface was obtained when the sputtering power was set to 150 W. The MoS<sub>2</sub> films obtained at 100 W sputtering power displayed the best HER activity, while the smooth films revealed the worst HER activity, as both the Tafel slope and overpotential at -10 mA cm<sup>-2</sup> current density are higher for the sample, fabricated at 150 W.

### 1.2.3. Hydrothermal/solvothermal synthesis

Hydrothermal and solvothermal synthesis methods are probably one of the most useful methods for the synthesis of HER electrocatalysts due to the ease of obtaining various nanostructures. During hydrothermal synthesis, an aqueous solution of Mo and S precursors is poured into a suitable pressure vessel (usually a PTFE-lined steel autoclave) which is then heated at a fixed temperature for up to 24 hours [86]. During synthesis, Mo<sup>VI</sup> complexes are usually reduced by S<sup>2-</sup> that also acts as a sulfur source. However, the reaction mechanism is perplexing, as it depends largely on the precursors used and the exact mechanism of MoS<sub>2</sub> synthesis is not yet elucidated [117]. After cooling down to room temperature, MoS<sub>2</sub> precipitates are then removed from the

vessel and washed thoroughly to remove traces of precursor solution. Solvothermal synthesis proceeds in much the same way, differing only in that non-aqueous solutions of precursors are used. The ability to control the morphology of the material, as well as its physical and chemical properties, is readily available. By altering the type of precursors and solvents used, synthesis temperature and time, and by inserting substrates, various nanomaterials could be obtained, such as nanowires, nanorods, nanospheres, or nanoplatelets [86].

One of the first reports of nanocrystalline MoS<sub>2</sub> solvothermal synthesis was published in 1998 [118]. A mixture of molybdenum trioxide and elemental sulfur was used as Mo and S precursors, hydrazine monohydrate was used as a reducing agent and pyridine was used as a solvent. It was found that thin platelets of nanocrystalline 2H-MoS<sub>2</sub> were formed when the Mo:S precursor ratio was 1:2 or 1:3, whereas a mixture of MoS<sub>2</sub> and MoO<sub>2</sub> had formed when the precursor ratio was 1:1, suggesting that MoO<sub>2</sub> might be a reaction intermediate. More recently, Lin *et al.* fabricated MoS<sub>2</sub> nanorods via hydrothermal synthesis at 220 °C for 24 h by adding silicotungstic acid to an aqueous solution of sodium molybdate and thioacetamide [119]. It was found that the addition of silicotungstic acid promotes the formation of uniform nanorods with a diameter of 20–50 nm and a length of 400–500 nm. This was ascribed due to the intermediate product H<sub>4</sub>SiMo<sub>12</sub>O<sub>40</sub> possibly serving as a template since the addition of other inorganic acids or synthesis without any additional acids did not yield nanorods, but rather combined nanoparticles. Xie *et al.* obtained oxygen-incorporated MoS<sub>2</sub> via hydrothermal synthesis by controlling the crystallization process [120]. Decreasing the synthesis temperature leads to insufficient reduction of the molybdenum precursor, in this case ammonium heptamolybdate, thus Mo-O bonds may be incorporated into the MoS<sub>2</sub> nanosheets. Moreover, it was reported that higher synthesis temperatures lead to higher crystallinity of products and the lowest degree of disorder, whereas highly disordered MoS<sub>2</sub> nanosheets were obtained by lowering the synthesis temperature to 140 °C. HER investigations portrayed the intermediate temperature (180 °C) MoS<sub>2</sub> to be the most active, with the overpotential at -10 mA cm<sup>-2</sup> current density being 30 – 45 mV lower than for other tested samples in their work. Similarly, Zhao *et al.* reported the solvothermal synthesis of oxygen-incorporated MoS<sub>2-x</sub> nanosheets [121]. By comparing the XPS of as-grown samples and commercially available bulk MoS<sub>2</sub> oxygen incorporation was identified as temperature-dependent, with the highest synthesis temperature (260 °C) sample possessing the highest quantity of oxygen content. The sample synthesized at 220 °C was shown to possess the best HER activity due to the largest ECSA and better conductivity than

samples fabricated at other temperatures. Dunne *et al.* proposed a scalable continuous-flow hydrothermal synthesis method, which allowed the stepwise investigation of the MoS<sub>2</sub> synthesis [122]. Continuous-flow hydrothermal synthesis boasts considerably faster reaction times and scalability to industrial levels. During synthesis, a stream of ammonium heptamolybdate aqueous solution was mixed with a preheated stream of thiourea and an additional stream of acetic acid was added to speed up the reaction process and to precipitate the reaction intermediates as amorphous MoS<sub>3</sub>. The authors proposed a mechanism of MoS<sub>2</sub> synthesis as proceeding by sulfidation of molybdate anions to form MoS<sub>4</sub><sup>-</sup>, which then forms amorphous MoS<sub>3</sub> in the acidification step, and further hydrothermal processing decomposes MoS<sub>3</sub> into nanosheets of MoS<sub>2</sub>.

One of the advantages of hydrothermal/solvothermal synthesis methods is the facile fabrication of MoS<sub>2</sub> nanosheet films directly onto a suitable substrate. This was described in a publication by Miao *et al.* where MoS<sub>2</sub> films were obtained on Ti foil substrates [123]. This was achieved by placing a piece of Ti foil into an autoclave, filled with an aqueous solution of sodium molybdate and thiourea. By placing the piece of foil at an angle, different growth of MoS<sub>2</sub> was observed for the up and bottom sides of the foil. It was determined from SEM images that the upside is covered with flowerlike nanospheres whose diameter ranged from 2 to 6 μm as the hydrothermal synthesis was carried out from 3 to 24 hours at 220 °C, respectively, while a continuous film of nanosheets was observed at the bottom. Interestingly, when synthesis was performed for 3 hours at 200 °C, both sides were covered with regularly arranged MoS<sub>2</sub> nanosheet films, and increased synthesis time to 6 hours at the same temperature resulted in flowerlike microspheres on the upside of the foil. XRD analysis revealed a (002) diffraction peak shift from 14.2° to 9.4° for the samples synthesized for 3h, as well as those, that were synthesized at 200 °C, indicating an enlargement of interlayer spacing, while other samples matched well with the diffraction peaks of pure hexagonal MoS<sub>2</sub>.

Arguably one of the most beneficial, as far as the fabrication of HER electrocatalysts is concerned, is the ability to obtain the 1T-MoS<sub>2</sub> phase via hydrothermal/solvothermal synthesis. The first identification of hydrothermally synthesized material as 1T-MoS<sub>2</sub> might be credited to the work of Song *et al.* published in 2015 [124]. It was reported that by using ammonium heptamolybdate and thiourea as Mo and S sources, with a Mo:S ratio of 1:2.14, 1T-MoS<sub>2</sub> was obtained via ammonium ion intercalation into the MoS<sub>2</sub> interlayer spacing by coordination with S. Ammonium ions were described as forming due to amine molecule hydrolysis from reactant

materials and protonation by water under hydrothermal synthesis conditions. Interestingly, the authors declare that changing the Mo precursor to sodium molybdate with the same Mo:S ratio results in 2H-MoS<sub>2</sub> and 1T-MoS<sub>2</sub> could only be obtained from this precursor if the Mo:S ratio is increased to 1:3. Various characterization techniques were used to confirm that the synthesized material consists of the metallic phase and their results were in good agreement with characterizations of 1T-MoS<sub>2</sub> obtained via Li-ion exfoliation. The authors also proved that obtained 1T-MoS<sub>2</sub> was a more efficient HER catalyst than pristine 2H-MoS<sub>2</sub>. Ammonium-intercalated MoS<sub>2</sub> has been prepared using ammonium bicarbonate as an intercalant [125, 126]. Sun *et al.* reported the synthesis of a 3D microsphere-like structure with a diameter of 2 – 5 µm using ammonium heptamolybdate and thiourea synthesis solution with a Mo:S precursor ratio of 1:4 and adding ammonium bicarbonate [125]. The prepared nanospheres were composed of individual MoS<sub>2</sub> flakes with an average thickness of 10 nm. An increased interlayer spacing to 0.93 nm and enhanced hydrophilicity were reported. Similarly, Wang and coworkers report on multiphasic 1T/2H MoS<sub>2</sub> from ammonium molybdate, thiourea, and ammonium bicarbonate [126]. Contrary to the previous report, synthesized MoS<sub>2</sub> was composed of 50 – 60 nm size nanoflowers, with the same 0.93 nm interlayer spacing confirmed by HRTEM, while also confirming the co-existence of both 1T and 2H phases. It is important to note, that in [126] the Mo:S precursor ratio was 1:2.48 which may be one of the reasons why no 3D microspheres were formed, as Sun *et al.* report that without adding ammonium bicarbonate, Mo:S 1:2 ratio leads to the synthesis of 2H-MoS<sub>2</sub> and increasing the sulfur content leads to 1T/2H-MoS<sub>2</sub> [125]. The fabricated 1T/2H multiphasic electrocatalyst displayed improved HER performance with a Tafel slope value of 46 mV dec<sup>-1</sup> and, according to the report, 1T content could be controlled by adjusting the synthesis temperature. A report by Geng and coworkers claim that hydrothermally grown 1T-MoS<sub>2</sub> could also be stabilized by water molecules [66]. In their work, 1T-MoS<sub>2</sub> was synthesized using MoO<sub>3</sub>, thioacetamide, and urea as a molybdenum precursor, sulfur precursor, and reducing agent, respectively. Raman, XPS and XRD were used to characterize the grown MoS<sub>2</sub> as metallic. It is reported, that the increased interlayer spacing of hydrothermally synthesized 1T-MoS<sub>2</sub> matches the theoretically calculated spacing of 11.8 Å, corresponding to a bilayer of water molecules between adjacent MoS<sub>2</sub> layers. Heterogeneous 1T/2H nanosheets were synthesized with a mixture of propionic acid and water as a solvent [127]. Two distinct lattice matrices were identified in the MoS<sub>2</sub> basal plane by HRTEM. The average size of the 1T-MoS<sub>2</sub> phase regions, indicated by trigonal lattice features, was determined to be approximately 5 nm, while the

honeycomb lattice of trigonal prismatic coordination indicated 2H-MoS<sub>2</sub> formation. Additionally, defects were observed, especially at the interface between crystalline 1T and 2H domains, and were attributed to lattice misfit between the two phases. Propionic acid was determined to influence the quantity of 1T phase formed. When the propionic acid:water ratio was 2:1 or 1:2, the quantity of 1T was reported to be about 70%, while decreasing the amount of propionic acid (1:5 ratio) resulted in 43% of 1T phase in 1T/2H heterogeneous nanosheets. The authors also reported that the overpotential needed to achieve -10 mA cm<sup>-2</sup> current density was -220 mV for 1T/2H-MoS<sub>2</sub> electrocatalyst, which is 100 mV lower than the overpotential of their fabricated 2H-MoS<sub>2</sub>, indicating improved HER efficiency. Fabrication of 1T-MoS<sub>2</sub> phase in the hydrothermally synthesized nanomaterials could also be achieved by using ethanol. Li *et al.* obtained high 1T concentration using the synergistic effect of ethanol and nitric acid [128]. It was reported that MoS<sub>2</sub> synthesis from ammonium heptamolybdate and thiourea aqueous solution with additional HNO<sub>3</sub> and C<sub>2</sub>H<sub>5</sub>OH yields up to 83.6% of 1T phase in the fabricated nanosheets, while the 1T phase content was reported at 33% when only nitric acid was added. The obtained high-content 1T-MoS<sub>2</sub> was reported to be stable for up to 6 months. A two-step hydrothermal synthesis route to fabricate 1T-doped 2H-MoS<sub>2</sub> was described by Yao and coworkers [129]. The nanosheets are first synthesized from ammonium heptamolybdate and thiourea aqueous solution at 200 °C. Then, the obtained nanosheets are rinsed and autoclaved again, this time in ethanol at 220 °C, resulting in sulfur vacancy formation at the nanosheet surface. It is claimed that these sulfur vacancies promote the phase transition from 2H to 1T.

Various modifications of conventional techniques were also reported for the fabrication of 1T phase via hydrothermal/solvothermal synthesis, showing promising results for HER electrocatalyst fabrication. Vertically aligned 1T-MoS<sub>2</sub>, which was called a monolithic catalyst, bonded to a plate of molybdenum metal was reported by Wang *et al.* [130]. This was done using an aqueous solution of sodium molybdate, thiourea, and additional polyethylene glycol (PEG-6000) surfactant and a vertically inserted Mo plate introduced into the autoclave. The authors claim that the charged particles do not need to cross the interlayer spacing, but rather could be transferred directly from the Mo plate to the catalyst nanosheets, greatly facilitating the electron transfer. The 1T-MoS<sub>2</sub> monolithic catalyst exhibited substantial HER activity and was shown to perform stably at -350 mA cm<sup>-2</sup> for up to 60 hours in 0.5 M H<sub>2</sub>SO<sub>4</sub>. Venkateshwaran *et al.* achieved the selective formation of 1T-MoS<sub>2</sub> by using a mesoporous silica template Santa Barbara Amorphous-15 (SBA-15) [131]. SBA-15 is composed of a porous silica network, resembling a

honeycomb structure, with a uniform pore size of 10 – 15 nm. SBA-15 was found to facilitate 1T-MoS<sub>2</sub> phase formation due to confined pore channel space. Interestingly, it was reported that (002) peak shift was observed in XPS only in the sample synthesized with ammonium heptamolybdate without SBA-15, while Raman analysis showed most intense bands, attributable to 1T-MoS<sub>2</sub>, were observed for samples synthesized with SBA-15, especially the sample where sodium molybdate was used. The latter was ascribed to the possibility of more sluggish insertion of Mo<sub>7</sub>O<sub>24</sub><sup>6-</sup> ions into the pores of SBA-15, compared to MoO<sub>4</sub><sup>2-</sup> ions from sodium molybdate. XPS analysis revealed that samples synthesized from sodium molybdate with SBA-15 contain up to 90% of 1T-MoS<sub>2</sub>, which was the highest content from their samples, and excellent reproducibility was pointed out by repeating the synthesis 14 times with unvarying results. Ding and coworkers described the phase-controlled synthesis of 1T-MoS<sub>2</sub> via hydrothermal synthesis under high magnetic fields [132]. In what was described as magneto-hydrothermal processing, an autoclave filled with ammonium molybdate and thiourea aqueous solution was heated at 210 °C in a heating sleeve with circulating water cooling, which was placed between two superconducting magnets, capable of operating up to 10T. Obtained MoS<sub>2</sub> nanosheets had high crystalline quality and it was shown that nanosheet thickness decreased when the applied magnetic field was increased. The diagonal atomic-scale edge structure was ascertained via HAADF-STEM, confirming the formation of 1T-MoS<sub>2</sub>. From the XPS analysis, the influence of magnetic fields on the 1T phase content was investigated. Pure 100% 1T-MoS<sub>2</sub> was detected when the applied magnetic field was at 9T, while 76.4%, 48.9%, and 24.7% were determined for samples synthesized at 8T, 5T, and 0T, respectively. After ageing the magneto-hydrothermally synthesized 1T-MoS<sub>2</sub> for one year XRD, HAADF-STEM, and XPS analysis revealed no obvious changes, corroborating the exceptional stability of 1T-MoS<sub>2</sub> nanosheets.

Lastly, the HER activity of MoS<sub>2</sub> electrocatalysts could be increased by doping various heteroatoms, forming heterostructures, or introducing basal plane defects. Increased HER performance of MoS<sub>2</sub> via transition metal doping was reported by Shi *et al.* [133]. Metal-doped MoS<sub>2</sub> was fabricated by adding ammonium tetrathiomolybdate to DMF and FeCl<sub>2</sub>, Co(NO<sub>3</sub>)<sub>2</sub>, Ni(NO<sub>3</sub>)<sub>2</sub>, Cu(NO<sub>3</sub>)<sub>2</sub>, or Zn(NO<sub>3</sub>)<sub>2</sub> solution and autoclaved at 200 °C. Characterization of obtained transition metal doped MoS<sub>2</sub> revealed the different electronic densities of MoS<sub>2</sub>, which were determined from a varying negative shift of binding energies via XPS, while no variations in morphology or crystal structure of MoS<sub>2</sub> were determined. It is stated that different electronic densities of MoS<sub>2</sub> affect the HER catalytic activity, and it was

reported that Fe and Co doping decreased HER electrocatalytic activity, while Ni doping had negligible effect. Meanwhile, Cu and Zn-doped MoS<sub>2</sub> possessed increased HER activity, particularly Zn-MoS<sub>2</sub> for which a 13 times larger current density, compared to a non-doped sample, was observed at -200 mV. Gao *et al.* described the phase transition of 2H-MoS<sub>2</sub> to 1T-MoS<sub>2</sub> due to electron injection by Co and Ni co-doping [134]. This was achieved via hydrothermal synthesis with additional CoSO<sub>4</sub> and NiSO<sub>4</sub> added to the standard synthesis solution. It was found that co-doped Co,Ni-MoS<sub>2</sub> contained about 69% of 1T phase, while for single atom doped Co-MoS<sub>2</sub> and Ni-MoS<sub>2</sub> the 1T phase contents were reported at 26%, and 21%, respectively. The HER activity of Co,Ni-MoS<sub>2</sub> was substantially higher than for single-atom doped MoS<sub>2</sub>, with the overpotential at -10 mA cm<sup>-2</sup> being -102 mV in 1M KOH solution. By introducing reduced graphene oxide (RGO) during hydrothermal MoS<sub>2</sub> synthesis an RGO/1T-MoS<sub>2</sub> heterostructure was fabricated by He and coworkers [135]. Aside from the addition of graphene oxide to the synthesis solution, the authors also report on what was called slow successive heating where citric acid was added to the synthesis solution, and hydrothermal synthesis was carried out by a stepwise temperature change, maintaining the synthesis reactor for 2 hours at 50 °C, 70 °C, 100 °C, 130 °C and at the last stage a temperature of 160 °C was maintained for 16 hours. The role of citric acid/ successive heating was to slow down the formation of MoS<sub>2</sub> and thus facilitate the formation of the 1T phase. Reduced graphene oxide and citric acid/ successive heating were found to decrease the average particle size of MoS<sub>2</sub> nanosheets leading to an increase in active surface area. Because of this, RGO/1T-MoS<sub>2</sub> displayed enhanced photo- and electrocatalytic hydrogen evolution activity. Recently, a bifunctional MoS<sub>2</sub> electrocatalyst for both hydrogen and oxygen evolution reactions was fabricated using Fe/Ni bimetallic organic framework (b-MOF) supported 1T/2H-MoS<sub>2</sub> heterostructure [136]. This was achieved by hydrothermal synthesis of sodium molybdate, thiourea, and Fe/Ni-MOF, which was prepared by a separate hydrothermal process and was used as the framework for 1T/2H-MoS<sub>2</sub>. Obtained MoS<sub>2</sub>@Fe/Ni-MOF possessed flower-like morphology with furcated nanosheet petals, which are assumed to induce numerous distortions or dislocations making such a defect-rich structure preferable for catalysis. The increase of HER and OER electrocatalytic activity was ascribed to the synergistic effect of specific 3D structure formation, electronic modulation of MoS<sub>2</sub> by Fe/Ni, and 1T/2H phase formation. Xie *et al.* reported a scalable synthesis method to engineer defects on MoS<sub>2</sub> and increase the number of active sites [137]. This was achieved by using a high concentration of thiourea, as it was claimed that excess thiourea could adsorb to the growing

nanocrystallites and impede the oriented growth of the crystal, thus forming defect-rich structures. It was pointed out that by decreasing both precursor concentrations, whilst still maintaining an excess of thiourea, thick nanosheets with defect-rich structures were obtained, while higher concentrations resulted in thinner nanosheets. Defect-rich MoS<sub>2</sub> possessed an overpotential of -120 mV, which is comparable to overpotentials obtained with 1T-MoS<sub>2</sub>, while the number of active sites for the defect-rich MoS<sub>2</sub> was reported to be 13 times greater than that of bulk MoS<sub>2</sub>. A rapid one-pot MoS<sub>2</sub> electrocatalyst synthesis on a glassy carbon electrode was described by Nakayasu and coworkers [138]. MoS<sub>2</sub> films on glassy carbon electrodes (GCE) were fabricated via hydrothermal electrodeposition, during which GCE was used as a working electrode, and Au foil was used as a counter electrode, while sodium tetrathiomolybdate and KCl were used as an electrolyte. Electrodes were submerged in the electrolyte and placed in a pressure reactor, which was pressurized to 10 MPa using Ar and the reactor was heated to 200 °C. A negative potential of -1.5 V was applied for up to 60 s to the glassy carbon electrode which was used as a substrate for MoS<sub>2</sub> film. It was determined that a uniform coating of MoS<sub>2</sub> forms on the GCE surface when electrolysis was used, and an edge-exposed surface was obtained when hydrothermal electrodeposition was carried out at 200 °C, while synthesis at 150 °C leads to a cracked surface with limited exposed edges. Moreover, XPS revealed that synthesis at 200 °C for 60 s results in the highest 1T phase content, whereas peaks attributable to Mo<sup>5+</sup> and Mo<sup>6+</sup> were considerably more pronounced when synthesis was carried out at 150 °C. The formation of the 1T phase was attributed to high sulfur defect content on the surface of MoS<sub>2</sub> films, as the formation of sulfur defects is claimed to be due to proton and electron transfer to the S atoms during electrodeposition. As synthesis for 10 min at 200 °C produced predominantly 2H-MoS<sub>2</sub> and MoS<sub>3</sub>, synthesis for just 60 seconds resulted in the best electrocatalyst of those tested by the authors, making this synthesis method immensely faster than conventional hydrothermal methods.

### 1.3. Electrochemical water splitting

The hydrogen evolution reaction is a half-reaction of the water splitting process, where the oxygen evolution reaction (OER) occurs on the anode and the hydrogen evolves at the cathode under applied voltage [139]. Hydrogen evolution is a two-step reaction (Fig. 1.4. a) during which in the first step, called the Volmer reaction, H<sub>3</sub>O<sup>+</sup> (in acidic media) or H<sub>2</sub>O (in alkaline media) adsorbs on the active site of the catalyst and hydrogen intermediates (H\*) are

produced via electrochemical reduction step. In the second step, desorption of  $\text{H}_2$ , formed by Heyrovsky or Tafel reactions, occurs [140]. During the Heyrovsky reaction, adsorbed  $\text{H}^*$  combines with  $\text{H}_3\text{O}^+$  or  $\text{H}_2\text{O}$  to form  $\text{H}_2$ , while during the Tafel reaction  $\text{H}_2$  is formed by combining two adsorbed  $\text{H}^*$ . As the adsorbed  $\text{H}^*$  is involved in all three reaction pathways, the hydrogen adsorption free energy ( $\Delta G_{\text{H}^*}$ ) is crucial for the HER – if the hydrogen is bonded to the surface too weakly, the adsorption (Volmer) step limits the reaction rate, whereas too strong bonding limits the desorption steps (Heyrovsky/Tafel) [141]. Therefore, an ideal electrocatalyst should possess  $\Delta G_{\text{H}^*}$  that is close to zero (Fig. 1.4. b), and according to theoretical calculations,  $\Delta G_{\text{H}^*}$  of Pt metal is 0.06 eV, making it the best electrocatalyst so far [25].

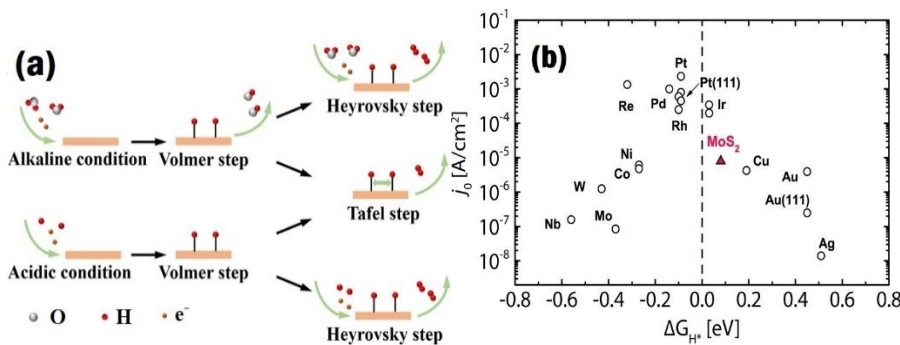


**Figure 1.4.** (a) Schematic illustration of the HER mechanisms in acidic and alkaline media [142]. (b) Exchange current density as a function of  $\Delta G_{\text{H}^*}$  for different HER electrocatalysts [141].

$\text{MoS}_2$  was determined to possess nearly neutral hydrogen adsorption free energy ( $\Delta G_{\text{H}^*} = 0.08$  eV, when  $\text{H}^*$  coverage is 50%), however, the exchange current density is lower than those observed on Pt [25]. Nevertheless, various strategies to decrease the  $\Delta G_{\text{H}^*}$  of  $\text{MoS}_2$  are being considered, such as doping of  $\text{MoS}_2$  with phosphorous and oxygen, as reported by Huang and coworkers [143]. Based on DFT calculations, Tsai *et al.* reported that an increase of 0.037 nm in the interlayer spacing of  $\text{MoS}_2$  (equivalent to a 6% expansion between layers) leads to a reduction of 0.05 eV in the hydrogen adsorption free energy compared to non-expanded pristine  $\text{MoS}_2$  [144]. It was determined by Jaramillo *et al.* that the edge sites of  $\text{MoS}_2$  are the active sites for HER electrocatalysis, while the basal plane is inert [145]. Although the basal plane is generally accepted to be inert [146, 147], Bentley and coworkers reported that the activity of the basal plane could be undervalued by numerous other reports [148]. Using scanning electrochemical cell microscopy, it was

determined that the basal plane of 2H-MoS<sub>2</sub> possesses HER activity comparable to, if not somewhat higher, than glassy carbon, and the discrepancy from previous reports was attributed to perplexing HER activity evaluation using macroscale measurements due to high ohmic resistance of bulk 2H-MoS<sub>2</sub>.

The overall water splitting reaction ( $\text{H}_2\text{O} \rightarrow \text{H}_2 + \frac{1}{2}\text{O}_2$ ) requires an energy input of  $\Delta G = 237.1 \text{ kJ/mol}$  (at STP), which is equal to a thermodynamic potential of 1.23 V and the potential of HER is 0 V vs. RHE [149]. During electrochemical hydrogen evolution, the actual potential of HER is larger than 0 V due to electrode polarization, reaction activation energy, and internal resistance. This difference is defined as the overpotential of HER and is frequently used to characterize different HER electrocatalysts. Usually, the overpotential needed to generate -10 mA cm<sup>-2</sup> is used as a benchmark in various publications, along with onset potential, i.e. the potential at which cathodic current appears. Lower values of said potentials mean higher HER activity of the electrocatalyst in question. Another commonly used parameter for the characterization of HER electrocatalyst is the Tafel slope, which describes the dependence of steady-state currents when the overpotential is increased. It can be regarded as a value of additional overpotential needed to increase the current density by one order of magnitude. Smaller Tafel slopes correspond to better HER electrocatalytic activity. Furthermore, the value of the Tafel slope is used to determine the rate-determining step of the HER [150]. It is widely accepted and reported in the literature that the Tafel slope values of 120 mV dec<sup>-1</sup>, 40 mV dec<sup>-1</sup>, and 30 mV dec<sup>-1</sup> correspond to the Volmer, Heyrovsky, and Tafel steps as the rate-determining steps, respectively. Similarly, exchange current density, i.e. the current density when electrode reactions are in equilibrium, is used to characterize the rate of electrochemical reactions. Electrocatalysts with higher exchange current densities require less energy for the reaction to occur. The stability of the electrocatalyst during operation is also a key parameter. It is usually investigated via cyclic voltammetry, where the electrocatalyst is subjected to at least 1000 cycles of potential sweeps, or chronoamperometry and chronopotentiometry, during which a fixed potential or current is applied for a set amount of time (at least 12 hours). Observation of changes in current density or overpotential indicate the stability (or lack thereof) of the analyzed electrocatalyst. To evaluate the HER activity and compare different electrocatalyst materials, turnover frequency (TOF) is occasionally reported. TOF is defined as the number of product, which is H<sub>2</sub> in the case of HER,

obtained per active site in a time period [151]. Turnover frequency is calculated by:

$$\text{TOF} = \frac{jA}{znF} \quad (1)$$

where  $j$  is the current density,  $A$  is the electrochemically active surface area (ECSA),  $z$  is the number of electrons involved in the reaction,  $n$  is the number of moles of active material, and  $F$  is the Faraday constant [142]. One of the main advantages of TOF is the ability to directly compare different electrocatalysts, whether they are of the same material or not. However, difficulty in calculating  $n$  hinders accurate calculation of TOF, as not all active sites might be identical or uniformly accessible to the reactants. As the edge sites of MoS<sub>2</sub> are the active sites, and the basal plane is inert (or substantially less active), the ECSA may not represent the number of active sites, thus leading to an overestimation of TOF.

To summarize, the fabrication of molybdenum disulfide based catalysts, especially MoS<sub>2</sub> nanomaterials with high 1T-MoS<sub>2</sub> phase content, for hydrogen evolution via water splitting hold great promise. However, substantial additional research is necessary to better our understanding of MoS<sub>2</sub> catalyst synthesis and their potential application. The abundance of molybdenum disulfide nanomaterial fabrication methods and post-synthesis treatments discussed previously enables the synthesis of diverse MoS<sub>2</sub> materials, each possessing distinct catalytic capabilities and characteristics, some of which are yet to be systematically investigated. The influence of amino acid additives on the structure and catalytic properties of hydrothermally synthesized MoS<sub>2</sub> films has not been thoroughly explored and therefore it is investigated in the following sections. Moreover, a novel and facile post-synthesis treatment method of increasing the effectiveness of fabricated MoS<sub>2</sub>/amino acid electrode for hydrogen evolution reaction via *in situ* anodic pretreatment (occurring in the same setup prior to HER processing, hence referred to as *pre*-treatment) is reported in section 3.4.

## 2. MATERIALS AND METHODS

### 2.1. Materials and chemicals

All chemicals used were of analytical grade and used as-received unless stated otherwise. The list of chemicals used in experiments is provided in Table 1.

**Table 1.** Materials and reagents used for the experiments in this work

Material	Formula	Purity	Source
Titanium foil (0.127 mm)	Ti	99.7%	
Molybdenum foil (0.127 mm)	Mo	≥99.9%	Sigma-Aldrich, United States of America
L-cysteine	C <sub>3</sub> H <sub>7</sub> NO <sub>2</sub> S	≥97%	
D,L-histidine	C <sub>6</sub> H <sub>9</sub> N <sub>3</sub> O <sub>2</sub>	≥99%	
Propan-2-ol	(CH <sub>3</sub> ) <sub>2</sub> CHOH	≥99.5%	Carl Roth, Germany
Ammonium fluoride	NH <sub>4</sub> F	98%	Merck, Germany
Phosphoric acid	H <sub>3</sub> PO <sub>4</sub>	85%	
Ammonium heptamolybdate tetrahydrate	(NH <sub>4</sub> ) <sub>6</sub> Mo <sub>7</sub> O <sub>24</sub> ·4H <sub>2</sub> O	≥99.5%	Reachem, Slovakia
Potassium chloride	KCl	≥99.6%	
Glycine	C <sub>2</sub> H <sub>5</sub> NO <sub>2</sub>	98.5%	
Acetone	(CH <sub>3</sub> ) <sub>2</sub> CO	99.5%	
Sulfuric acid	H <sub>2</sub> SO <sub>4</sub>	98%	Chempur, Poland
Thiourea	CH <sub>4</sub> N <sub>2</sub> S	≥99.5%	

### 2.2. Substrate preparation

Substrates for fabricated MoS<sub>2</sub> electrodes were cut from Ti or Mo foil, with their size being 7 x 7 mm (electrochemical measurements) or 10 x 10 mm (structure characterization investigations). After cutting, the surface of the substrates was cleaned in a 1:1 mixture of acetone and propan-2-ol to remove any surface contaminants. The substrates were fully submerged in the cleaning mixture and ultrasonicated for 30 minutes. Afterwards, they were thoroughly rinsed with deionized water and ultrasonicated in deionized water for 10 minutes, repeating the deionized water cleaning procedure three times.

### 2.3. Anodizing of titanium substrates

To obtain a porous TiO<sub>2</sub> structure which could provide better surface adhesion properties than pure metallic Ti, titanium nanotubes were fabricated via anodizing of Ti substrates. A solution of phosphoric acid and ammonium fluoride was prepared by dissolving 3.704 g of NH<sub>4</sub>F in 250 mL of deionized water. In a volumetric flask, filled with about 125 mL of deionized water, 67.4 mL of H<sub>3</sub>PO<sub>4</sub> was slowly added, stirred and then the resultant solution was filled with deionized water, resulting in 250 mL of acidic solution. Both solutions were mixed in a plastic bottle, stirred and left to cool down to room temperature.

Anodizing of Ti substrates was carried out using a PeakTech 6227 power supply (PeakTech Prüf- und Messtechnik, Germany) in a plastic cell filled with 2 M H<sub>3</sub>PO<sub>4</sub> and 0.2 M NH<sub>4</sub>F solution, where Ti substrates were used as an anode and two parallel Pt plates were used as a cathode. The anodizing voltage was set at 20 V and anodizing of Ti was conducted for 60 minutes, constantly maintaining 100 rpm stirring to dissipate heat. Before the start of anodizing at 20 V, the potential was set at 10 V for 1 min in order to prevent a rapid rise in temperature and current. After anodizing, the prepared anodized Ti substrates were thoroughly rinsed with copious amounts of deionized water, dried using N<sub>2</sub> gas stream and then annealed at 420 °C for two hours. During annealing, the formed Ti nanopores undergo recrystallization, resulting in the formation of anatase phase TiO<sub>2</sub> nanopores, eliminating F<sup>-</sup> ions in the process.

### 2.4. Molybdenum disulfide synthesis

Molybdenum disulfide films were fabricated via hydrothermal synthesis using a solution of ammonium heptamolybdate and thiourea. 5 mM of ammonium heptamolybdate and 90 mM of thiourea were dissolved in deionized water, stirred, and then poured into the PTFE cell of the autoclave. Additionally, different amino acids (L-cysteine, DL-histidine, glycine) were added to the synthesis solution during the fabrication of particular electrodes or MoS<sub>2</sub> powders, with the concentrations of amino acids reported in the respective sections. The prepared solution was then poured into the PTFE-lined stainless steel autoclave, while the substrate which was to be coated with MoS<sub>2</sub> was mounted in a specially made mounting point in the PTFE cell so that the substrate could be fully submerged and remain fixed in a perpendicular position throughout the whole synthesis process.

Synthesis was carried out by heating the autoclaves in a Zhermack DM40 furnace (Zhermack SpA, Italy) at 220 °C for 5 to 15 hours, with the temperature ramp being 10 °C min<sup>-1</sup>. After the autoclaves naturally cool down to ambient temperature, the fabricated electrodes were carefully removed from the mounting point, thoroughly rinsed with deionized water, and dried at room temperature using low-pressure N<sub>2</sub> gas stream.

MoS<sub>2</sub> powder synthesis was done by the same procedure described above. Key differences were: 1) no electrode substrate was placed in the autoclave during powder synthesis and 2) rinsing of MoS<sub>2</sub> powders was performed more rigorously, compared to rinsing of fabricated electrodes, as the risk of mechanically damaging the electrode surface necessitates the use of milder rinsing protocols. After the autoclave cooled down to ambient temperature, the synthesized powder was collected into a centrifuge tube, filled with 15 mL of deionized water and centrifuged at 9000 rpm for 30 minutes. The water was then carefully removed and the tube was once more filled with 15 mL of deionized water, repeating the process no less than five times. Afterwards, the rinsed MoS<sub>2</sub> powder was carefully dried at room temperature using N<sub>2</sub> gas stream and stored under Ar or N<sub>2</sub> atmosphere.

Electrochemical measurements and characterization of fabricated MoS<sub>2</sub> films and powders were conducted with minimal delays after synthesis when possible, in order to prevent any damage to the samples due to oxidation or phase conversion in air. To avoid structural changes of fabricated MoS<sub>2</sub> due to storage in air, samples for belated experiments were sealed in a tube filled with Ar or N<sub>2</sub>.

## 2.5. Electrochemical measurements

Electrochemical measurements of molybdenum disulfide HER efficiency, working stability, electrochemical impedance spectroscopy, and anodic pretreatment were performed using a Zahner Zennium electrochemical workstation (Zahner-Elektrik, Germany). A standard three-electrode cell was used for all electrochemical measurements, with the fabricated electrode used as a working electrode, Ag/AgCl, KCl<sub>sat</sub>, with a Luggin capillary used as a reference electrode, and a graphite rod used as a counter electrode. The electrolyte used in all electrochemical measurements described in this work was 0.5 M H<sub>2</sub>SO<sub>4</sub> solution. Prior to experiments, the electrolyte in a set-up cell was purged with N<sub>2</sub> gas for 60 minutes. All potentials in text refer to SHE unless stated otherwise.

The activity and stability of fabricated MoS<sub>2</sub> electrodes were investigated by cyclic voltammetry. A potential region of +0.05 V – -0.35 V was selected for HER activity measurements and stability was investigated by cycling the electrodes for up to 2000 potential cycles. All cyclic voltammetry measurements were carried out with the scan rate being 0.01 V s<sup>-1</sup> unless specified otherwise. Anodic pretreatment via linear sweep voltammetry or cyclic voltammetry was carried out by scanning the fabricated electrodes from -0.25 V or -0.35 V to different anodic switching potentials (+0.9 V, +1.7 V, +2.0 V, +2.5 V) and back at a 0.01 V s<sup>-1</sup> or 0.005 V s<sup>-1</sup> scan rate. Anodic pretreatment was also carried out at a fixed potential (+0.1 V, +0.3 V, +0.4 V, +0.6 V, +0.72 V, +0.8 V, +0.85 V, +1.2 V) for a duration of 15 s or 900 s. The anodic pretreatment and subsequent cathodic HER activity investigations were carried out in the same 0.5 M H<sub>2</sub>SO<sub>4</sub> solution without changing the electrolyte and electrode. Chronopotentiometry was also used to evaluate electrode stability, subjecting the samples to a fixed current density of -10 mA cm<sup>-2</sup> for the duration of the experiment.

The electrode kinetics during HER were investigated via electrochemical impedance spectroscopy. The spectra were recorded in a frequency range from 0.1 Hz to 50 kHz using potentiostatic mode with the sine amplitude of 10 mV. Obtained data was normalized to the geometric surface area of the working electrode, and the data fitting was carried out using Zview 2.8 (AMETEK Scientific Instruments, United States of America) software.

## 2.6. Characterization of synthesized MoS<sub>2</sub> films

**Scanning and high-resolution transmission electron microscopy.** The morphology of synthesized MoS<sub>2</sub> films was investigated using a Helios Nanolab 650 scanning electron microscope (FEI, The Netherlands) equipped with an energy dispersive X-ray spectrometer (Oxford Instruments, United Kingdom). Cross-sectional cuts were made using a 30 keV Ga ion beam. Nanoplatelet interplanar distance was investigated using Tecnai F20 transmission electron microscope (FEI, The Netherlands).

**X-ray diffraction.** Structural analysis and crystallinity of synthesized MoS<sub>2</sub> was evaluated using SmartLab X-ray diffractometer (Rigaku, Japan) equipped with a rotating CuK<sub>α</sub> anode X-ray tube. Diffractograms were obtained in Bragg-Brentano scan mode with a  $2\theta = 0.02$  deg step and a scan rate of 2 deg per minute. Obtained diffractograms were analyzed using PDXL software and PDF4+ database.

**Raman spectroscopy.** Raman spectroscopy was carried out using Renishaw inVia spectrometer (Renishaw, United Kingdom) equipped with

thermoelectrically cooled (-70 °C) CCD camera and microscope. Raman spectra were excited with either 442 nm or 532 nm radiation from diode-pumped solid-state laser. The 50x/0.75 NA objective lens and 1800 lines/mm grating were used to record the spectra, for which the accumulation time was 400 s. To avoid damaging the sample, the laser power was restricted to 0.06 mW. The laser line was focused to ~2 mm diameter spot on the sample. Raman scattering wavenumber axis was calibrated by the silicon peak at 520.7 nm. Parameters of the bands were determined by fitting the experimental spectra with the Gaussian-Lorentzian shape components using GRAMS/A1 8.0 (Thermo Scientific, United States of America) software.

**X-ray photoelectron spectroscopy.** The chemical state of elements comprising the MoS<sub>2</sub> film was studied by XPS spectroscope VERSAPROBE PHI 5000 (Physical Electronics, United States of America), equipped with a Monochromatic Al K<sub>a</sub> anode ( $\lambda = 1.540 \text{ \AA}$ ). The spectra were collected at a 45° angle with respect to the electron energy analyzer, with a sample spot size of 200  $\mu\text{m}$ . The C1s peak at 284.6 eV was used as a reference for calibration of binding energies (BE). A dual beam charge neutralization with an electron gun (~1 eV) and an Ar ion gun ( $\leq 10 \text{ eV}$ ) was used for built up charge compensation on the sample surface. Deconvolution and fitting of obtained XPS spectra were performed using CASA XPS (Casa Software, United Kingdom) software.

**Thermogravimetric analysis/Mass spectroscopy.** Investigation of the thermal decomposition of L-cysteine was carried out using a simultaneous thermal analyzer (TGA-DSC) STA PT 1600 (Linseis, Germany) equipped with a MS Thermostar GDS 320 (Linseis/Pfeiffer, Germany) mass spectrometer. 10 mg of sample were placed in a PtRh can, which was heated with 10 °C min<sup>-1</sup> ramp in an argon atmosphere. Evaluation and Quadera software v 4.62 (INFICON, Switzerland) were used for the data collection and fitting.

**Fourier-transform infrared spectroscopy.** FTIR spectra were recorded in attenuated total reflection (ATR) mode using ALPHA FTIR spectrometer (Bruker, Germany), while the pure MoS<sub>2</sub> sample spectrum was recorded in transmission mode, with the sample dispersed in KBr pellet. All spectra were acquired from 100 scans in the range of 400-4000 cm<sup>-1</sup> with the resolution of 4 cm<sup>-1</sup>. Air measurements were used as the background. Analysis of obtained spectra was performed using GRAMS/A1 8.0 (Thermo Scientific, United States of America) software.

### 3. RESULTS AND DISCUSSION

#### 3.1. Synthesis and characterization of MoS<sub>2</sub>/Glycine films

##### 3.1.1. Morphology of MoS<sub>2</sub>/Glycine films

Molybdenum disulfide was synthesized via hydrothermal synthesis at 220 °C for 5 to 15 hours using 5 mmol L<sup>-1</sup> ammonium heptamolybdate, 90 mmol L<sup>-1</sup> thiourea, and glycine, with the concentration of glycine varying from 0 to 150 mmol L<sup>-1</sup>.

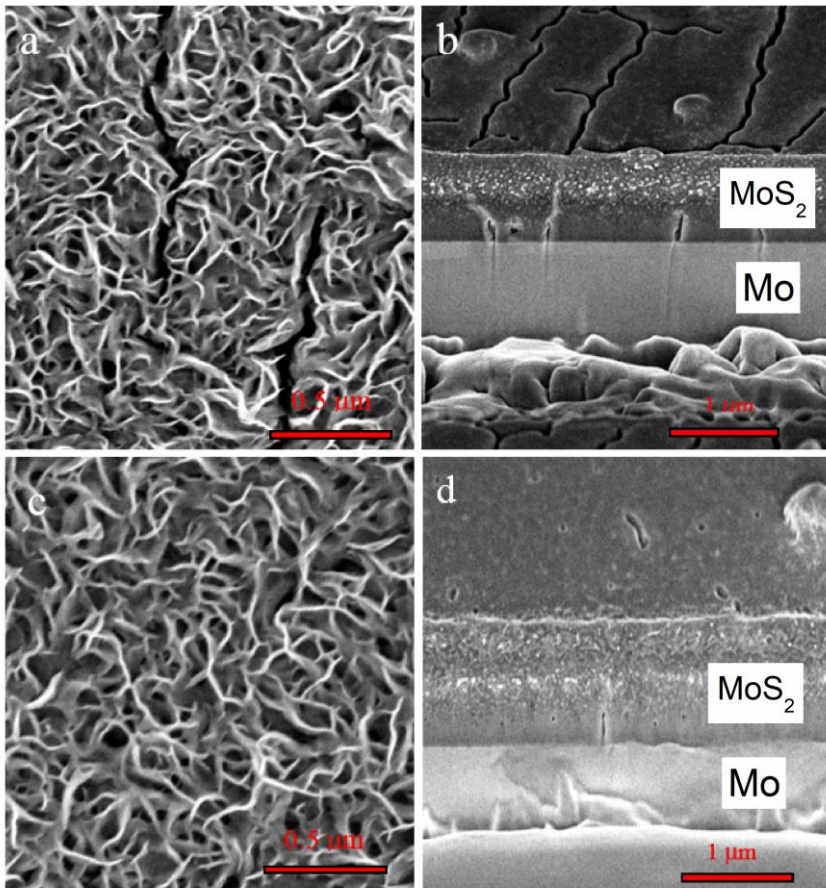


**Figure 3.1.** Topside (a,c) and cross-section (b,d) SEM images of MoS<sub>2</sub> films on Mo substrates hydrothermally synthesized for 5 hours without glycine (a,b), and containing 100 mmol L<sup>-1</sup> of glycine (c,d).

**3.1. pav.** MoS<sub>2</sub> dangų, hidrotermiškai sintetintų 5 val. be (a,b) ir su 100 mmol L<sup>-1</sup> glicino (c,d) ant Mo pagrindo paviršiaus (a,c) ir skerspjūvio (b,d) SEM nuotraukos.

Mo or Ti metal foils were used as substrates and a uniform black-coloured film was observed on the surface of the substrates after synthesis. Scanning electron microscopy (SEM) images of the hydrothermally synthesized MoS<sub>2</sub> films are shown in Fig. 3.1. It can be observed that the addition of glycine to the synthesis solution does not influence the morphology of the MoS<sub>2</sub> films – similar nanoplatelets were formed both with and without glycine. The size of a single nanoplatelet was approximated to be  $200 \pm 50$  nm, while the thickness was  $5 \pm 2$  nm. Based on the thickness, the nanoplatelet is estimated to consist of 5 to 12 stacked S-Mo-S nanosheets. Note, that the films obtained with glycine were found to be less cracked and slightly thicker than those obtained under the same conditions without glycine. However, no noticeable difference in morphology of the samples with different concentrations of glycine was determined (Fig. 3.2.). The thickness and uniformity of MoS<sub>2</sub> films were found to depend on the synthesis duration, where syntheses for 5 hours at 220 °C resulted in 0.8 – 0.9 µm thick films, while 2 µm thick films were obtained when the synthesis duration was increased to 15 hours.

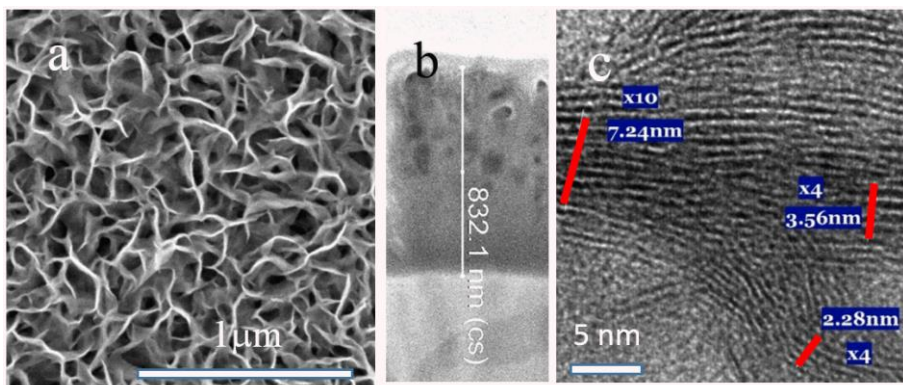


**Figure 3.2.** Topside (a) and cross-section (b) SEM, and HRTEM (c) images of the film synthesized with 40 mmol L<sup>-1</sup> of glycine for 5 hours.

**3.2. pav.** MoS<sub>2</sub> dangų, sintetintų 5 val. su 40 mmol L<sup>-1</sup> glicino, paviršiaus (a) ir skerspjūvio (b) SEM, bei HRTEM (c) nuotraukos.

Various lattice distortions and defects were observed in the HRTEM image (Fig. 3.2 c). It can be observed that the lattice spacing is non-uniform and diverges from the 0.615 nm value for pure 2H-MoS<sub>2</sub>. The estimated lattice spacing for the synthesized MoS<sub>2</sub> films with glycine reaches 0.89 nm in some areas. This implies that the intercalation of guest species into the interlayers of MoS<sub>2</sub> was achieved when glycine was used during the hydrothermal synthesis [152].

### 3.1.2. Characterization of MoS<sub>2</sub>/Glycine films

The crystallinity of synthesized molybdenum disulfide films was investigated via XRD. The obtained X-ray diffractograms of pure MoS<sub>2</sub>, grown hydrothermally without glycine (Fig. 3.3. a1) are in good agreement with the standard 2H-MoS<sub>2</sub> (molybdenite) diffractograms (PDF card 00-037-1492). The peaks at 2θ values of 14.37°, 33.51°, and 35.87° were attributed to (002), (101), and (102) planes, respectively, of a hexagonal lattice with cell constants  $a = b = 3.161 \text{ \AA}$ ,  $c = 12.298 \text{ \AA}$ , which are comparable with the values expected for 2H-MoS<sub>2</sub>. On the other hand, differences from pure 2H-MoS<sub>2</sub> are observed in the XRD patterns of MoS<sub>2</sub> synthesized with glycine (Fig. 3.3. a2-a4). The key difference is the shift of the (002) diffraction peak at  $2\theta = 14.37^\circ$ , to  $2\theta = 9.4^\circ$ . As mentioned in the literature review section 1.1.2., the shift of (002) diffraction peak to lower  $2\theta$  values is indicative of interlayer expansion via intercalation of guest species. The observed shift in XRD is in accord with the previously described HRTEM, indicating that the addition of glycine to the hydrothermal synthesis solution brings about the interlayer expansion of MoS<sub>2</sub> films.

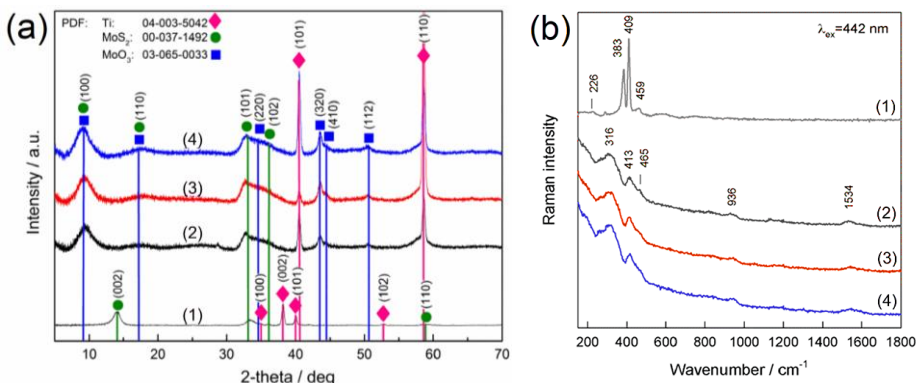


**Figure 3.3.** X-ray diffractograms (a) and Raman spectra (b) of MoS<sub>2</sub> hydrothermally synthesized on Ti substrates for 5 hours without glycine (1) and with additional 40 (2), 70 (3), and 100 (4) mmol L<sup>-1</sup> of glycine.

**3.3. pav.** MoS<sub>2</sub> dangū, susintetintū per 5 val. ant Ti pagrindo be glicino (1) ir su 40 (2), 70 (3), bei 100 (4) mmol L<sup>-1</sup> glicino, Rentgeno difraktogramos (a) ir Raman spektrai (b).

For insight into the 1T/2H phase determination of the synthesized MoS<sub>2</sub> films Raman spectroscopy measurements were performed and the obtained Raman spectra are shown in Fig. 3.3. b. In the spectrum of MoS<sub>2</sub> synthesized without additional glycine in the synthesis solution (Fig. 3.3. b1), two distinct

Raman modes, namely  $E^{1g}$  ( $383\text{ cm}^{-1}$ ), and  $A_{1g}$  ( $409\text{ cm}^{-1}$ ), were distinguished. As mentioned previously, the S atom in-plane vibration ( $E^{1g}$ ) and S atom out-of-plane stretching ( $A_{1g}$ ) modes are characteristic of crystalline 2H-MoS<sub>2</sub> [153]. In contrast, the incorporation of glycine into the synthesis solution resulted in the fabrication of MoS<sub>2</sub> films with a lower degree of crystallinity, as evidenced by less prominent Raman peaks. The  $A_{1g}$  mode experiences a redshift from  $409\text{ cm}^{-1}$  to  $413\text{ cm}^{-1}$ , while the  $E^{1g}$  disappears completely and the appearance of previously absent modes at  $316\text{ cm}^{-1}$ ,  $936\text{ cm}^{-1}$ , and  $1534\text{ cm}^{-1}$  is observed. The disappearance of  $E^{1g}$  and decrease in  $A_{1g}$  intensity could be a sign of 1T/2H phase mixture, as described in section 1.1.2. [79, 80]. The spectra of MoS<sub>2</sub> films with different concentrations of glycine appear similar, with only a slight increase of a low-intensity peak at  $1534\text{ cm}^{-1}$  attributed to glycine was determined when the concentration of glycine was increased from  $40\text{ mmol L}^{-1}$  to  $100\text{ mmol L}^{-1}$ . The small peak at  $936\text{ cm}^{-1}$  could be attributed to a small amount of ammonium heptamolybdate residue from the synthesis solution [154].

Further evaluation of MoS<sub>2</sub> film phase composition was carried out by XPS. The spectrum from  $222\text{ eV}$  to  $240\text{ eV}$  region (Fig. 3.4. a) represents the photoelectrons emitted from the Mo 3d core state and the S 2s core state. Mo 3d spectrum was deconvoluted into three doublet components, with two doublets ascribed to Mo<sup>4+</sup> of 2H-MoS<sub>2</sub> at  $229.4\text{ eV}$  ( $3d_{5/2}$ ) and  $232.5\text{ eV}$  ( $3d_{3/2}$ ), and Mo<sup>4+</sup> of 1T-MoS<sub>2</sub> at  $228.3\text{ eV}$  ( $3d_{5/2}$ ) and  $231.5\text{ eV}$  ( $3d_{3/2}$ ), and the third one ascribed to Mo<sup>6+</sup> of MoO<sub>3</sub> at  $232.2\text{ eV}$  ( $3d_{5/2}$ ) and  $235.3\text{ eV}$  ( $3d_{3/2}$ ). The relative contribution of these components was calculated, respectively, at 36%, 49%, and 15%. Two main doublets were distinguished in the S 2p spectrum (Fig. 3.4. b) at the  $157\text{ eV} - 173\text{ eV}$  region. These were ascribed to S<sup>2-</sup> of 1T-MoS<sub>2</sub> at  $161.1\text{ eV}$  ( $2p_{3/2}$ ) and  $162.2\text{ eV}$  ( $2p_{1/2}$ ), and of 2H-MoS<sub>2</sub> at  $162.1\text{ eV}$  ( $2p_{3/2}$ ) and  $163.2\text{ eV}$  ( $2p_{1/2}$ ). The small doublet at  $\sim 168\text{ eV}$  stems from SO<sub>x</sub>, likely due to a low extent of surface oxidation. Thus, it can be determined that sulfur atoms are predominantly involved in S-Mo bonds, as no other features were observed in the S 2p spectrum. The N 1s spectrum ( $390 - 410\text{ eV}$ ) overlaps with the spectrum of photoelectrons emitted from the Mo 3p core state ( $385 - 420\text{ eV}$ ), therefore the obtained spectrum (Fig 3.4. c) was deconvoluted into four components, with the first three ascribed to Mo 3p<sub>3/2</sub> components from 1T-MoS<sub>2</sub> ( $394.2\text{ eV}$ ), 2H-MoS<sub>2</sub> ( $395.1\text{ eV}$ ), and MoO<sub>3</sub> ( $397.8\text{ eV}$ ). The fourth component at  $401.2\text{ eV}$  could be due to glycine, as a peak for protonated NH<sub>3</sub><sup>+</sup> is located at  $402.4\text{ eV}$ , whereas the neutral amino group (NH<sub>2</sub>) peak is located at  $400.5\text{ eV}$  [155]. It has been suggested by Tzvetkov and Netzer that the occurrence of this peak could be attributed to adsorbed molecular fragments from partially decomposed glycine.

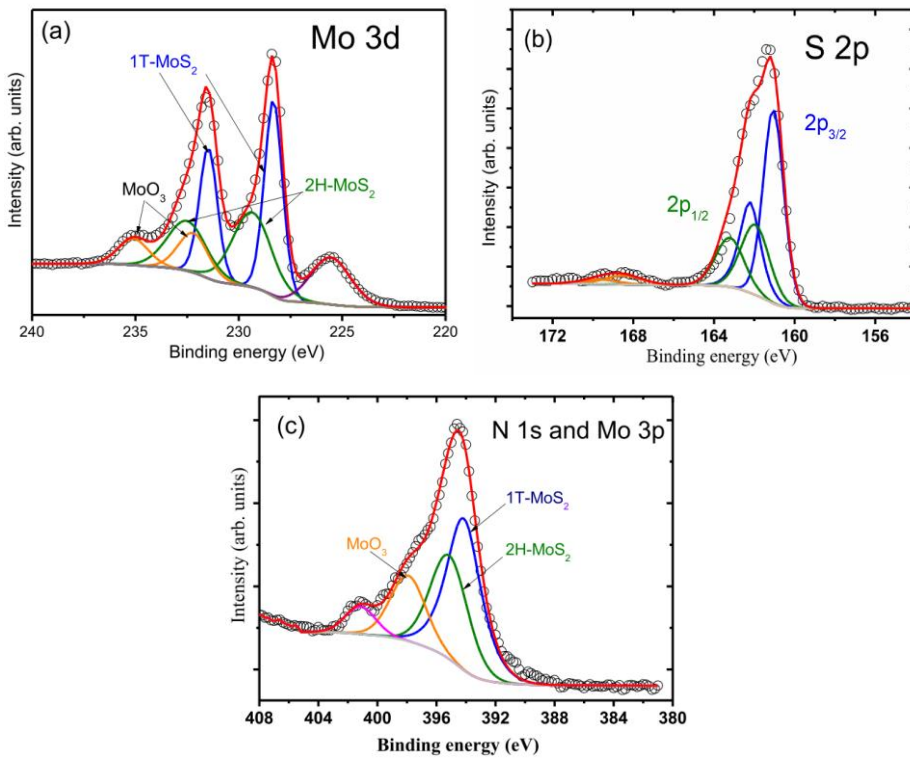


**Figure 3.4.** Deconvoluted X-ray photoelectron spectra of MoS<sub>2</sub>/Glycine films. (a) Mo 3d core state region, (b) S 2p core state region, (c) overlapping N 1s and Mo 3p core state regions.

**3.4. pav.** Išskaidyti MoS<sub>2</sub>/Glicino Rentgeno fotoelektronų spektrai: Mo 3d ir S 2s spektras (a), S 2p spektras (b), N 1s ir Mo 3p spektras (c).

### 3.1.3. Investigation of MoS<sub>2</sub>/Glycine electrode HER performance

The catalytic activity and stability of synthesized MoS<sub>2</sub>/Glycine electrodes was investigated by cyclic voltammetry in 0.5 M H<sub>2</sub>SO<sub>4</sub> and the recorded voltammograms are displayed in Fig. 3.5. It was determined that the addition of glycine has an influence on the HER activity and stability of the fabricated electrode. When no glycine was used (Fig. 3.5. a), the initial current densities at -0.35 V reached 56.8 mA cm<sup>-2</sup>, however, after more than 50 potential scan cycles the current densities at -0.35 V were substantially lower, and after 250 cycles the current density was 17.1 mA cm<sup>-2</sup> or almost one-third of the initial current density. On the other hand, MoS<sub>2</sub> electrodes with glycine did not display such poor stability. In the case of films synthesized with 40 mmol L<sup>-1</sup> of glycine (Fig. 3.5. b), the initial current densities were similar to those

observed when no glycine was used, yet, after 250 potential cycles, the drop-off in current densities at -0.35 V was determined to be no more than 10%. Increase in glycine concentration to 70 mM (Fig. 3.5. c) led to an increase in both the activity of MoS<sub>2</sub>/Glycine electrode, as initial current density was slightly higher (62.5 mA cm<sup>-2</sup> at -0.35 V), and stability, since no significant changes in current density after 500 potential cycles were distinguished.

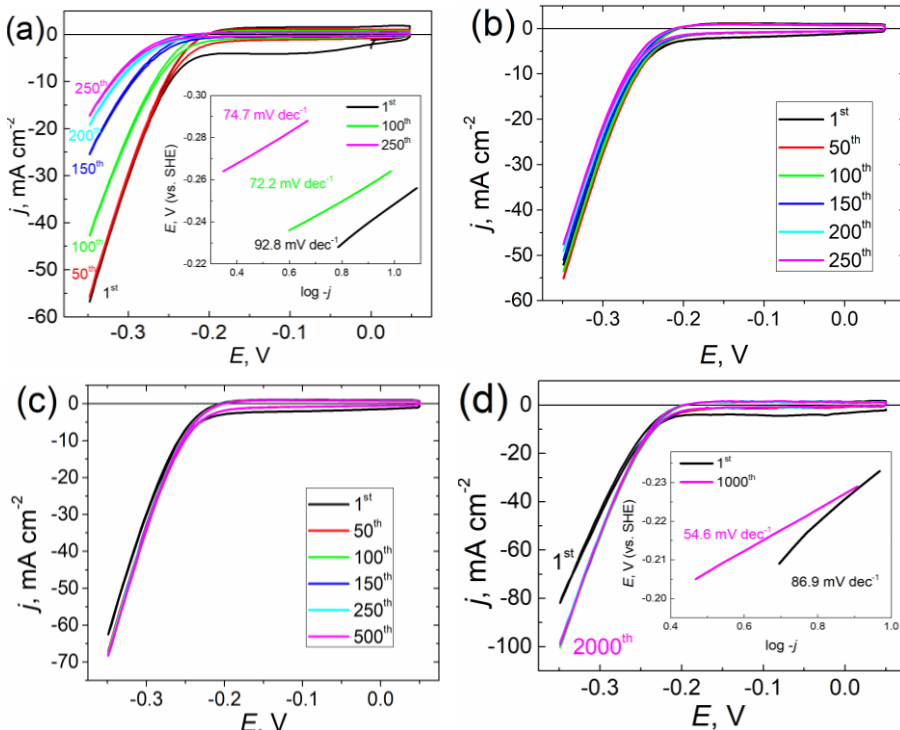


**Figure 3.5.** Cyclic voltammograms of MoS<sub>2</sub>/Glycine electrodes fabricated on Mo substrates with 0 mM (a), 40 mM (b), 70 mM (c), and 100 mM (d) of glycine. Insets in (a, d) shows the calculated Tafel slopes of the synthesized electrodes after indicated potential cycles in H<sub>2</sub>SO<sub>4</sub>.

**3.5. pav.** MoS<sub>2</sub>/Glicino elektrodo, susintetinto ant Mo pagrindo su 0 mM (a), 40 mM (b), 70 mM (c), ir 100 mM glicino (d) voltamperogramos. (a) ir (d) paveikslų intarpusose pavaizduoti Tafel nuolinkiai po atitinkamo ciklų skaičiaus.

A further increase in glycine concentration to 100 mmol L<sup>-1</sup> resulted in MoS<sub>2</sub> films with enhanced HER activity, where the initial current densities reached 82 mA cm<sup>-2</sup> and subsequently increased to ~100 mA cm<sup>-2</sup> during CV, whilst retaining the stability observed with 70 mM glycine samples for up to 2000 cycles. Calculated Tafel slopes (Fig. 3.5. d inset) were determined to be 55

$\text{mV dec}^{-1}$  for the electrode synthesized with  $100 \text{ mmol L}^{-1}$  of glycine. The onset potential was estimated at  $\sim 0.2 \text{ V}$  and was independent of the glycine concentration used, with the exception of (Fig. 3.5. a), when after potential cycling, the onset potential increased and reached  $\sim 0.24 \text{ V}$  after 250 cycles.

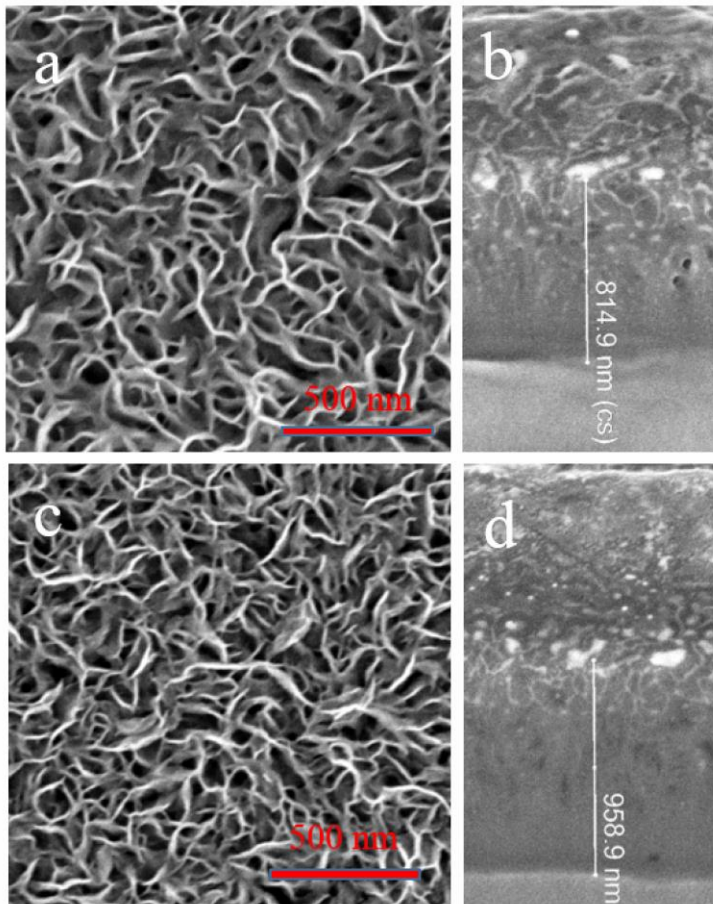


**Figure 3.6.** Topside (a, c) and cross-sectional (b, d) SEM images of  $\text{MoS}_2/\text{Glycine}$  film, fabricated with  $100 \text{ mmol L}^{-1}$  of glycine, before (a, b) and after (c, d) HER processing by CV for 2000 potential scan cycles.

**3.6. pav.**  $\text{MoS}_2/\text{Glicino}$  dangos, susintetintos su  $100 \text{ mmol L}^{-1}$  glicino paviršiaus (a, c) ir skerspjūvio (b, d) SEM nuotraukos prieš (a, b) ir po (c, d) 2000 potencialo skleidimo ciklų.

Additionally,  $\text{MoS}_2$  with  $150 \text{ mmol L}^{-1}$  of glycine was synthesized and tested. Their HER stability was found to be similar to  $100 \text{ mmol L}^{-1}$  of glycine samples, however, these electrodes possessed lesser HER activity. The stability of fabricated  $\text{MoS}_2/\text{Glycine}$  electrode was additionally confirmed by

evaluating the electrode mass loss after HER processing. When no glycine was used, the change in electrode mass ( $\Delta m$ ) was determined to be ~60% after 500 cycles, whereas the  $\Delta m$  of electrode with 100 mmol L<sup>-1</sup> of glycine was found at ~0.1% after 2000 potential sweep cycles. Visible changes to the fabricated electrode without glycine were observed, as the colour of the catalyst changed from deep black to dark gray, and black particles were seen in the electrolyte after CV tests. The SEM images of the MoS<sub>2</sub> film with glycine before and after hydrogen evolution reaction (Fig. 3.6.) did not exhibit any discernible alterations in the structural morphology of MoS<sub>2</sub>/Glycine film. Specifically, the image of post-CV film appeared highly similar to the pre-CV image, indicating the absence of any significant changes in the structure of MoS<sub>2</sub>.

### 3.2. Molybdenum disulfide films hybridized with L-cysteine

#### 3.2.1. Morphology of MoS<sub>2</sub>/Cysteine films

Molybdenum disulfide films with L-cysteine amino acid were fabricated via hydrothermal synthesis for 5 to 10 hours from ammonium heptamolybdate and thiourea solution, with up to 3 mmol L<sup>-1</sup> of L-cysteine added to the solution. The morphology of obtained films is shown in Fig. 3.7. From the SEM images, it can be determined that the structure of MoS<sub>2</sub> films remains similar, whether formed without (Fig. 3.7. a) or with (3.7. b) L-cysteine added to the synthesis solution. The substrate chosen was anodized titanium, as TiO<sub>2</sub> nanotubes (Fig. 3.7. b Inset), formed during anodizing of Ti, were found to improve the attachment of MoS<sub>2</sub> films to the substrate. The thickness of MoS<sub>2</sub> films is dependent on the synthesis duration, although films with L-cysteine were found to be somewhat thicker (Fig. 3.7. d) than their counterparts without L-cysteine. Distortion of atomically flat MoS<sub>2</sub> layers was observed from the HRTEM image (Fig 3.7. c). The interlayer spacing between adjacent S-Mo-S layers was estimated to be 8.4 Å, which is significantly larger than the 6.15 Å spacing, characteristic to crystalline 2H-MoS<sub>2</sub>. Furthermore, the HRTEM images revealed irregular distribution of atoms along with multiple twists and differences in interlayer spacing. In some areas the spacing between monolayers was greater than 10 Å, thus indicating possible intercalation of guest species.

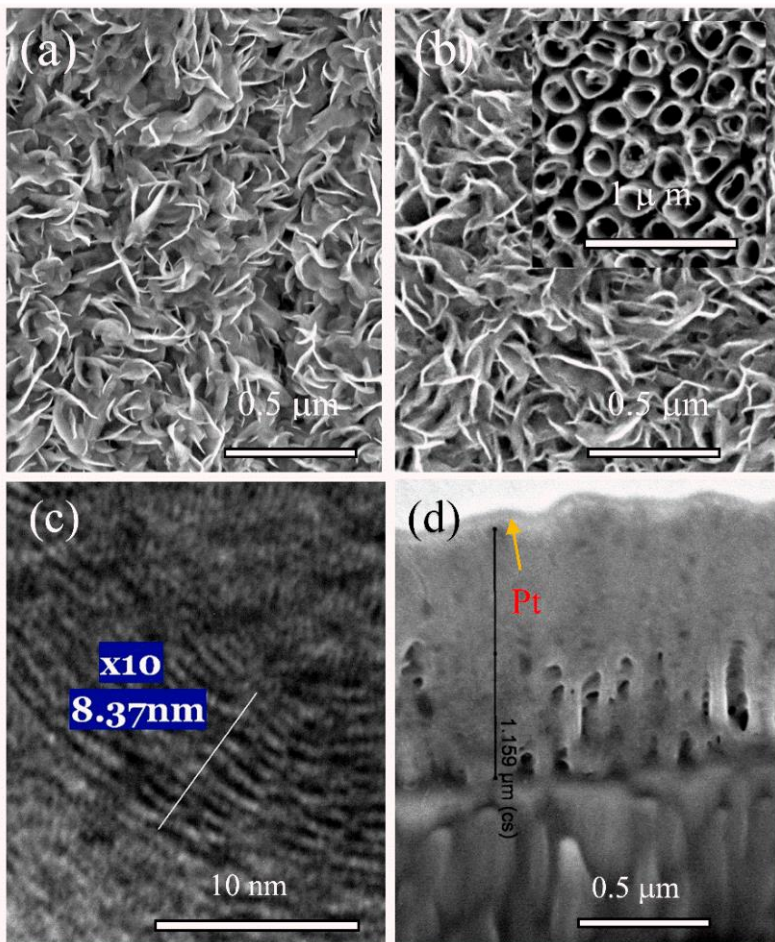


**Figure 3.7.** Topside (a,b) and cross-sectional (d) SEM and HRTEM (c) images of molybdenum disulfide film fabricated on anodized Ti (b Inset) synthesized without (a), and with 2 mM (b-d) of L-cysteine.

**3.7. pav.** MoS<sub>2</sub> dangos ant anoduoto Ti padéklo (b intarpas) be cisteino (a) ir su 2 mM cisteino (b-d) paviršiaus (a,b) bei skerspjūvio (d) SEM ir HRTEM (c) nuotraukos.

### 3.2.2. Characterization of fabricated MoS<sub>2</sub>/Cysteine films

Investigation of possible intercalation of guest species into the fabricated MoS<sub>2</sub> films was performed by Raman spectroscopy. The Raman spectra of as-grown MoS<sub>2</sub> film, as well as MoS<sub>2</sub>/Cysteine film before and after hydrogen evolution reaction processing via CV, are presented in Fig. 3.8. In the Raman spectrum of MoS<sub>2</sub> film without L-cysteine (Fig. 3.8. a), two well-defined

peaks at  $409.1\text{ cm}^{-1}$  and  $379.0\text{ cm}^{-1}$  were distinguished and attributed to  $A_{1g}$  and  $E^{1g}_{2g}$ , respectively. These two peaks in the  $\text{MoS}_2$  spectra without L-cysteine are characteristic of crystalline 2H- $\text{MoS}_2$ , as they are unambiguously observed regardless of the excitation wavelength used, as stated previously.

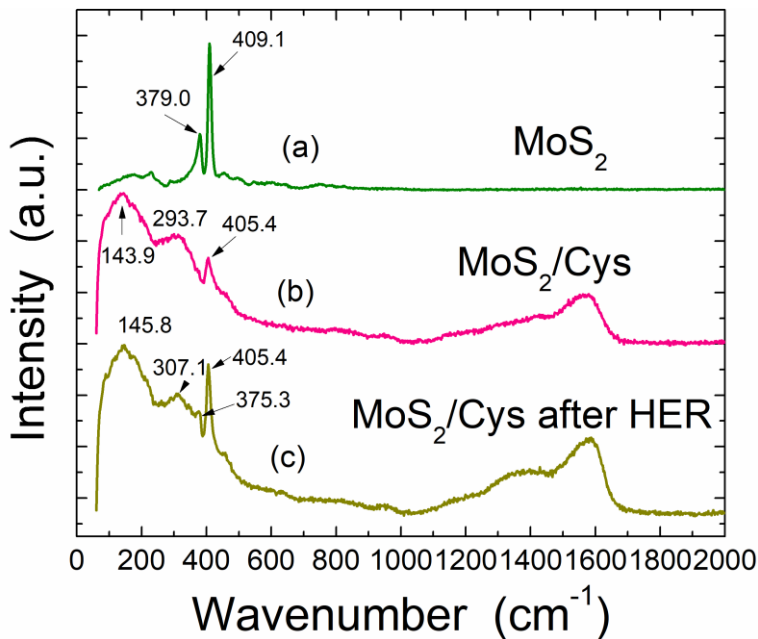


**Figure 3.8.** Raman spectra of hydrothermally synthesized  $\text{MoS}_2$  films without L-cysteine (a), with 3 mM of L-cysteine (b), and the same  $\text{MoS}_2$ /Cysteine film (abbreviated as  $\text{MoS}_2/\text{Cys}$ ) as in (b) after 1000 potential scan cycles (c). Excitation wavelength = 532 nm.

**3.8. pav.**  $\text{MoS}_2$  dangū be L-cisteino (a), su 3 mM L-cisteino (b), bei to paties  $\text{MoS}_2/\text{Cisteino}$  elektrodo (sutrum.  $\text{MoS}_2/\text{Cys}$ ) po 1000 CV ciklų (c) Raman spektrai.

The synthesized  $\text{MoS}_2/\text{Cysteine}$  sample exhibited some differences in the Raman spectrum (Fig. 3.8. b). The  $A_{1g}$  mode was found to be slightly blueshifted to  $405.4\text{ cm}^{-1}$  and possessed significantly less intensity, whereas the peak ascribed to  $E^{1g}_{2g}$  had disappeared. Two new peaks at  $143.9\text{ cm}^{-1}$  and  $293.7\text{ cm}^{-1}$  were identified, which could be ascribed to  $J_1$  and  $E_{1g}$  modes of 1T- $\text{MoS}_2$ , respectively, while a broad peak at the  $1100\text{-}1700\text{ cm}^{-1}$  region could arise due to cysteine molecules or their fragments. After subjecting the  $\text{MoS}_2/\text{Cysteine}$  sample to HER via CV for 1000 potential scan cycles, the Raman spectra (Fig 3.8. c) appears similar to the spectra of as-grown  $\text{MoS}_2/\text{Cysteine}$ . In this case, the main differences were determined to be the

increase of  $A_{1g}$  mode peak intensity and the reappearance of  $E^{1g}$ , albeit at low intensity. These findings seem consistent with reports of 1T/2H-MoS<sub>2</sub> Raman spectra, as the aforementioned changes to  $A_{1g}$  and  $E^{1g}$  and the appearance of new peaks are indicative of 1T-MoS<sub>2</sub>.

Investigation of the chemical states of the elements present in the surface region of the synthesized MoS<sub>2</sub>/Cysteine films was carried out using X-ray photoelectron spectroscopy. The surface of the MoS<sub>2</sub>/Cysteine film was found to contain Mo, S, O, N, and C elements according to the XPS survey spectrum depicted in Figure 3.9.

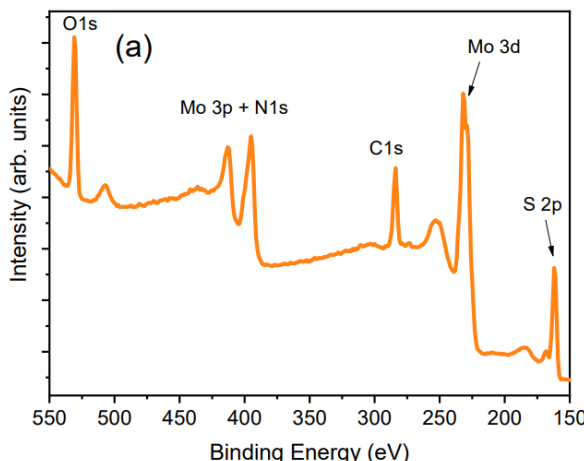


**Figure 3.9.** XPS survey spectrum of MoS<sub>2</sub>/Cysteine film hydrothermally synthesized for 5 hours at 220 °C using 3 mmol L<sup>-1</sup> of L-cysteine.

**3.9. pav.** MoS<sub>2</sub>/Cisteino dangos, susintetintos su 3 mmol L<sup>-1</sup> cisteino ties 220 °C 5 val. Rentgeno fotoelektronų tiriamasis spektras.

The Mo 3d spectrum (Fig. 3.10. a) was deconvoluted into five separate doublets. The first two doublets correspond to Mo<sup>4+</sup> of 1T-MoS<sub>2</sub> and 2H-MoS<sub>2</sub>, with the 3d<sub>5/2</sub> and 3d<sub>3/2</sub> component binding energies being 228.5 eV and 231.7 eV (1T), and 229.0 eV and 232.2 eV (2H), respectively. Another doublet was ascribed to Mo<sup>4+</sup> of MoO<sub>2</sub> with 230.4 eV (3d<sub>5/2</sub>) and 233.6 eV (3d<sub>3/2</sub>) peak binding energies. A low-intensity doublet at 229.7 eV (3d<sub>5/2</sub>) was conjectured to arise from Mo-N bonding. The last doublet observed at 232.5 eV (3d<sub>5/2</sub>) and 235.6 eV (3d<sub>3/2</sub>) was ascribed to Mo<sup>6+</sup> of MoO<sub>3</sub>.

In the deconvoluted S 2p spectrum (Fig. 3.10. b), three doublets with 2p<sub>3/2</sub> and 2p<sub>1/2</sub> components were observed. The first two doublets were ascribed to S<sup>2-</sup> of MoS<sub>2</sub>, where the component with peak binding energies at 161.5 eV (2p<sub>3/2</sub>) and 162.6 eV (2p<sub>1/2</sub>) ascribed to 1T-MoS<sub>2</sub> and the component with 163.0 eV (2p<sub>3/2</sub>) and 164.1 eV (2p<sub>1/2</sub>) peak binding energies ascribed to 2H-

$\text{MoS}_2$ . The third doublet with 168.4 eV ( $2\text{p}_{3/2}$ ) and 169.6 eV ( $2\text{p}_{1/2}$ ) peak binding energies was attributed to  $\text{SO}_x$ . As in the case of Mo 3d spectrum, the most intense peak in the S 2p spectrum is observed for the doublet ascribed to 1T- $\text{MoS}_2$ .

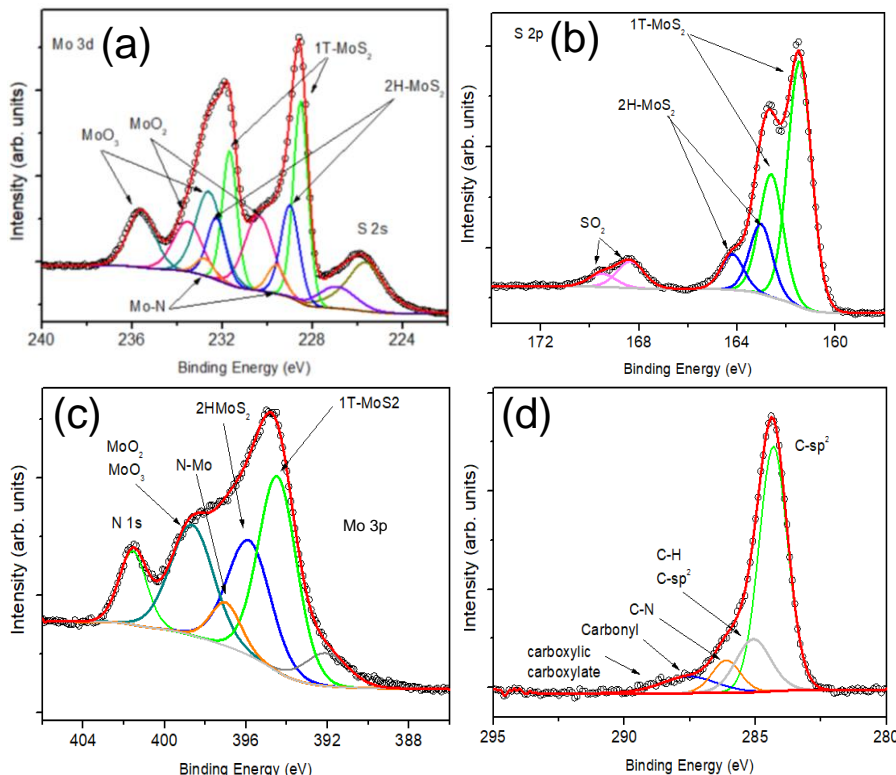


**Figure 3.10.** X-ray photoelectron spectra of  $\text{MoS}_2$ /Cysteine films: Mo 3d (a), S 2p (b), N 1s and Mo 3p (c), and C 1s (d) binding energy regions.

**3.10. pav.**  $\text{MoS}_2$ /Cisteino Rentgeno fotoelektronų spektrai: Mo 3d (a), S 2p (b), N 1s ir Mo 3p (c), bei C 1s (d) ryšio energijų ruožai.

In the N 1s and overlapping Mo 3p spectra (Fig. 3.10. c), three Mo 3p doublets were determined and attributed to  $\text{Mo}^{4+}$  of 1T- $\text{MoS}_2$  (394.2 eV), 2H- $\text{MoS}_2$  (395.9 eV), and  $\text{MoO}_x$  (398.6 eV). The peak BE values provided herein are for the  $3\text{p}_{3/2}$  component, as the doublet separation for Mo  $3\text{p}_{3/2}$  and  $3\text{p}_{1/2}$  components is  $\sim 18$  eV, thus the  $3\text{p}_{1/2}$  component is not observed in the spectrum. Additionally, two N 1s peaks were distinguished and attributed to N-Mo (397.0 eV) and  $\text{NH}_4^+$  (401.6 eV). The C 1s spectrum (Fig. 3.10. d) revealed carbon and various carbon compound derivatives, which could arise from the thermal decomposition of L-cysteine. The calculated relative

concentrations from XPS analysis was 32.8 at.% for C, 11.5 at.% for Mo, 25.3 at.% for S, 26.4 at.% for O, and 4.0 at.% for N.

### 3.2.3. Electrochemical HER performance of fabricated $\text{MoS}_2$ /Cysteine electrodes

The electrocatalytic activity of fabricated  $\text{MoS}_2$  electrodes with L-cysteine was investigated via cyclic voltammetry in 0.5 M  $\text{H}_2\text{SO}_4$  electrolyte. The stability of synthesized electrodes was examined by continuous CV cycling for up to 2000 potential sweep cycles. The obtained cyclic voltammograms are depicted in Fig. 3.11. From the cyclic voltammograms, it was determined that the initial onset potential for hydrogen evolution reaction was -0.2 V vs. SHE for the electrodes with cysteine and similar onset potential was estimated for pure  $\text{MoS}_2$  electrodes (Fig. 3.5. a). During CV, the onset potential for  $\text{MoS}_2$  with L-cysteine did not change noticeably, whereas for pure  $\text{MoS}_2$  the onset potential readily increased and reached about -0.24 V. Moreover, a difference in HER stability was observed for the electrodes fabricated with or without L-cysteine. In the case of pure  $\text{MoS}_2$  electrode (Fig. 3.5. a), the initial current densities at -0.35 V potential were  $56.8 \text{ mA cm}^{-2}$  and subsequently decreased after CV cycling, as mentioned previously.

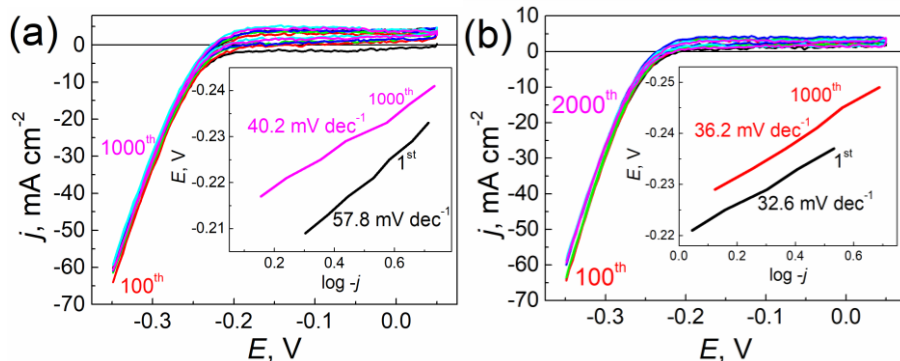


**Figure 3.11.** Cyclic voltammograms of  $\text{MoS}_2$  electrodes synthesized on anodized Ti for 10 hours with  $1 \text{ mmol L}^{-1}$  (a), and with  $3 \text{ mmol L}^{-1}$  of L-cysteine (b). The CV curves were recorded in  $0.5 \text{ M H}_2\text{SO}_4$  solution at  $10 \text{ mV s}^{-1}$  scan rate. Calculated Tafel slopes at the indicated CV cycle are depicted in the insets.

**3.11. pav.**  $\text{MoS}_2$  elektrodų, susintetintų ant anoduoto Ti pagrindo 10 val. su  $1 \text{ mmol L}^{-1}$  (a) ir  $3 \text{ mmol L}^{-1}$  (b) L-cisteino ciklinės voltamperogramos. Grafikų intarpusose pavaizduoti apskaičiuoti Tafel nuolinkiai atitinkamo ciklo metu.

On the other hand, the electrodes fabricated with L-cysteine possessed substantially better HER stability, with the current densities decreasing insignificantly over the course of cyclic voltammetry measurements. For both MoS<sub>2</sub> with 1 mmol L<sup>-1</sup> of L-cysteine (Fig. 3.11. a) and 3 mmol L<sup>-1</sup> of L-cysteine (Fig. 3.11. b) the initial current densities were about 62 mA cm<sup>-2</sup>, which were slightly higher than the initial current densities observed for pure MoS<sub>2</sub> electrode. During CV, a slight increase (~5 mA cm<sup>-2</sup>) in current densities was observed for both electrodes with L-cysteine after approximately 100 – 200 potential scan cycles, however, after 1000 or 2000 cycles the current densities were once again ~62 mA cm<sup>-2</sup>. Analysis of the Tafel slopes (insets of Fig. 3.11) revealed that electrodes with L-cysteine exhibit substantially lower Tafel slope values, compared to pure MoS<sub>2</sub> electrodes. For pure MoS<sub>2</sub> (Fig. 3.5. a inset), the Tafel slope during the first CV cycle was determined at 92.8 mV dec<sup>-1</sup> and was found to slightly decrease during HER processing, reaching ~75 mV dec<sup>-1</sup> after HER processing. In contrast, the Tafel slope values for electrodes with L-cysteine were determined to be lower both before and after potential cycling, as the slopes decreased from 57.8 mV dec<sup>-1</sup> for the sample with 1 mmol L<sup>-1</sup> of L-cysteine to 40.2 mV dec<sup>-1</sup>, and slightly increased from 32.6 mV dec<sup>-1</sup> to 36.2 mV dec<sup>-1</sup> for the sample with 3 mmol L<sup>-1</sup> of L-cysteine. Note, that the 32.6 mV dec<sup>-1</sup> Tafel slope value is close to the theoretical value of 30 mV dec<sup>-1</sup>, implying that the Tafel step ( $2\text{H}_{\text{ads}} \rightarrow \text{H}_2$ ) is the rate-determining step, whereas for pure MoS<sub>2</sub> the Tafel slope values are in between the values for rate-determining Volmer, and Heyrovsky steps (120 mV dec<sup>-1</sup> and 40 mV dec<sup>-1</sup>, respectively).

### 3.2.4. Insight into possible intercalation of L-cysteine

To study the influence of L-cysteine on the hydrothermal synthesis of molybdenum disulfide, thermogravimetry with mass spectrometry was carried out. It was determined from the thermogravimetric plot (Fig. 3.12. 1) that thermal decomposition of L-cysteine commences at ~200 °C and gaseous species with m/z = 17 (NH<sub>3</sub>), m/z = 34 (H<sub>2</sub>S), and m/z = 44 (CO<sub>2</sub>) were observed via mass spectrometry during decomposition (Fig. 3.12. 2-5), where the ionic current maximum for these species was found at 222 °C. According to Klimas *et al.* [156], only H<sub>2</sub>O and NH<sub>3</sub> evolved around 200 – 220 °C during the annealing of pure, hydrothermally synthesized MoS<sub>2</sub>, while the ionic currents of CO<sub>2</sub> and H<sub>2</sub>S were insignificantly low at this temperature interval. It was also established that emission of CS<sub>2</sub>, a possible thiourea residue, proceeds in the 200 – 400 °C temperature range with a single peak at 340 °C

for pure MoS<sub>2</sub>, while two temperature regions with peaks at 240 °C and 470 °C for CS<sub>2</sub> emission were observed for MoS<sub>2</sub> hydrothermally synthesized with L-cysteine. The thermal decomposition of cysteine was also studied by Weiss and coworkers [157]. It was reported, that the thermal decomposition of L-cysteine could occur by the removal of –COOH and –SH groups, while the remaining NH<sub>2</sub>-C<sub>a</sub>-C\* chain could undergo external cyclization. Consequently, it could be assumed that the functional groups of L-cysteine (-COOH, -SH, -NH<sub>2</sub>) should detach during hydrothermal synthesis of MoS<sub>2</sub> at 220 °C, as L-cysteine undergoes thermal decomposition at 200 °C and above. Therefore, it is difficult to expect intercalation of L-cysteine molecules between MoS<sub>2</sub> layers, yet, adsorption of fragments on and between MoS<sub>2</sub> nanoflakes could be plausible. Intercalation of charged guest species or fragments, formed due to the thermal decomposition of thiourea and L-cysteine is also plausible and would correspond well with the appearance of XPS peaks, attributed to 1T-MoS<sub>2</sub> and the increased interlayer distance observed via HRTEM.

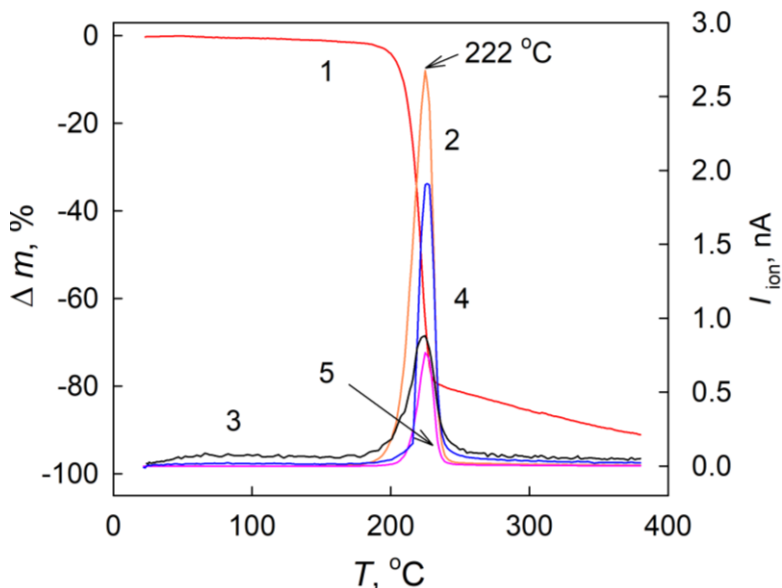


**Figure 3.12.** Thermogravimetric plot (1) and ionic currents determined by mass spectroscopy of gaseous species evolved during annealing of L-cysteine: CO<sub>2</sub> (2), H<sub>2</sub>O (3), NH<sub>3</sub> (4), and H<sub>2</sub>S (5).

**3.12. pav.** Termogravimetrinė kreivė (1) bei joninės srovės, nustatytos išsiskyrusių CO<sub>2</sub> (2), H<sub>2</sub>O (3), NH<sub>3</sub> (4), ir H<sub>2</sub>S (5) dujų masių spektroskopijos būdu, gautos kaitinant L-cisteiną.

### 3.3. Investigation of MoS<sub>2</sub>/Histidine electrochemical HER performance

#### 3.3.1. Morphology of MoS<sub>2</sub>/Histidine films

In this study, molybdenum disulfide films were synthesized onto anodized Ti substrates via hydrothermal synthesis from ammonium heptamolybdate and thiourea for 5 hours at 220 °C, adding up to 3 mmol L<sup>-1</sup> of D,L-histidine to the synthesis solution. The morphology of obtained MoS<sub>2</sub>/Histidine films is shown in Fig. 3.13.

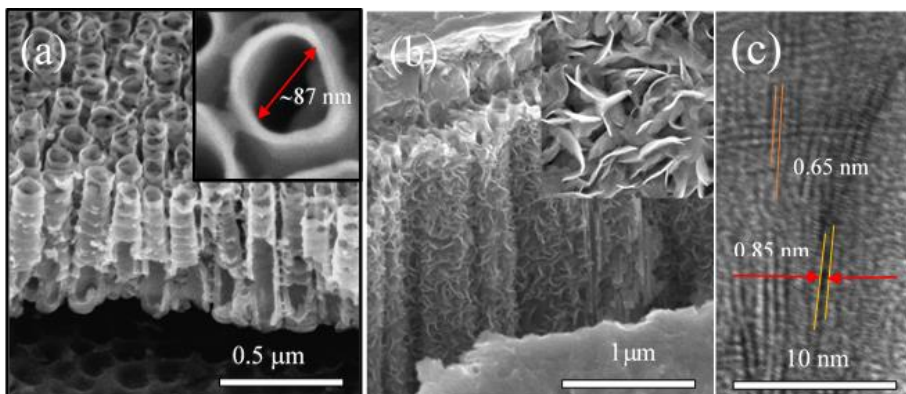


**Figure 3.13.** Cross-sectional (a,b) and top-side (Insets of a,b) SEM images of anodized Ti substrates prior to (a) and after synthesis (b) of MoS<sub>2</sub>/Histidine films, and HRTEM image of MoS<sub>2</sub>/Histidine (c).

**3.13. pav.** Anoduoto titano pagrindo skerspjūvio (a,b) ir paviršiaus (a,b intarpai) SEM nuotraukos prieš (a) ir po MoS<sub>2</sub>/Histidino dangų sintezės (b), bei MoS<sub>2</sub>/Histidino HRTEM nuotrauka (c).

From the SEM images (Fig. 3.13 a,b), the height of TiO<sub>2</sub> nanotubes was estimated to be ~0.56 μm and the average diameter of the nanotubes was 85 – 90 nm. The thickness of MoS<sub>2</sub>/Histidine film was 0.9 – 1.1 μm and the nanoplatelet morphology of the films was found to be similar to pure, hydrothermally synthesized MoS<sub>2</sub> films. A slight difference was noted, as MoS<sub>2</sub>/Histidine nanoplatelets appear longer, while for pure MoS<sub>2</sub> the nanoplatelets appear more densely packed. The layered morphology with a varied interlayer spacing of stacked layers was observed in the HRTEM image (Fig. 3.13. c). Various distortions and bends are observed, while the distance between adjacent layers was found to vary from 0.69 nm to 1.02 nm, implying possible intercalation of guest species into the interlayers of MoS<sub>2</sub>/Histidine films.

### 3.3.2. Electrochemical investigations of MoS<sub>2</sub>/Histidine electrodes

The electrocatalytic HER activity of fabricated MoS<sub>2</sub>/Histidine electrodes was investigated via cyclic voltammetry. Differences in the hydrogen electroreduction performance, as well as stability, were observed from the obtained CV curves (Fig. 3.14.). For MoS<sub>2</sub> fabricated without histidine (Fig. 3.14. a), the initial current density was determined to be 94.7 mA cm<sup>-1</sup>, however, the stability of the electrode was poor, with a decrease to 75.7 mA cm<sup>-1</sup> observed after 100 potential scan cycles, and just 8.1 mA cm<sup>-1</sup> after 1000 cycles. Concurrently, the MoS<sub>2</sub>/Histidine electrode (Fig. 3.14. b) exhibited significantly superior HER performance, compared to the MoS<sub>2</sub> electrode, fabricated without histidine. The initial current density of MoS<sub>2</sub>/Histidine was 96.6 mA cm<sup>-1</sup>, which is just slightly higher than the initial current observed for pure MoS<sub>2</sub>, yet, the current density increased during potential cycling and was determined to reach 108.4 mA cm<sup>-1</sup> after 100 cycles. Only a slight decrease of current density was observed after 1000 cycles and the electrode still retained improved HER activity for up to 2000 cycles when compared to both the initial current density of MoS<sub>2</sub>/Histidine and the overall performance of pure MoS<sub>2</sub>.

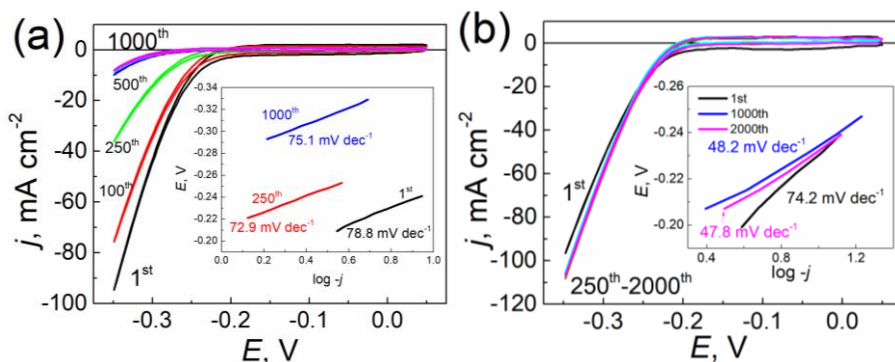


**Figure 3.14.** Cyclic voltammograms recorded in 0.5 M H<sub>2</sub>SO<sub>4</sub> solution of fabricated MoS<sub>2</sub>(a), and MoS<sub>2</sub>/Histidine (b) electrodes.

**3.14. pav.** Gryno MoS<sub>2</sub> (a) ir MoS<sub>2</sub>/Histidino (b) elektrodų ciklinės voltamperogramos, užrašytos 0.5 M H<sub>2</sub>SO<sub>4</sub> tirpale.

The calculated Tafel slopes for MoS<sub>2</sub> electrode without histidine (Fig. 3.14. Inset of a) show, that the HER reaction proceeds via Volmer – Heyrovsky mechanism, and the 75 – 79 mV dec<sup>-1</sup> value lies in between the theoretical values for the Volmer and Heyrovsky rate-determining steps. The Tafel slope of MoS<sub>2</sub>/Histidine electrode (Fig. 3.14. Inset of b) during the first

potential scan cycle was  $74.2 \text{ mV dec}^{-1}$ , similar to that of pure MoS<sub>2</sub>, although, during subsequent cycling, the Tafel slope decreased to  $48.2 \text{ mV dec}^{-1}$  after 1000 cycles and remained similar thereafter, signifying the Heyrovsky step as the rate-determining step. This suggests that the electron transfer to the reactive sites of MoS<sub>2</sub>/Histidine is improved during prolonged HER processing.

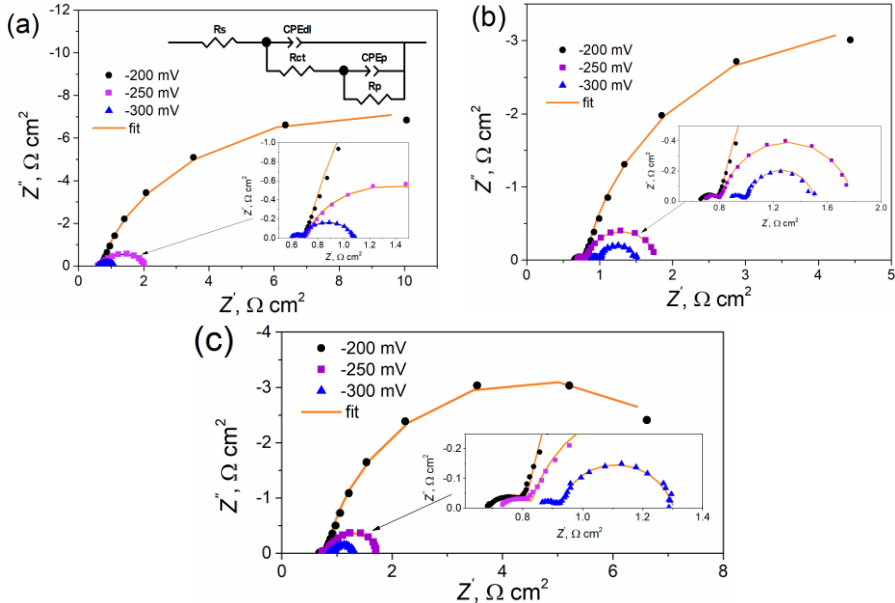


**Figure 3.15.** Nyquist plots obtained from electrochemical impedance spectroscopy of HER at fabricated electrodes: MoS<sub>2</sub> (a), MoS<sub>2</sub>/Histidino (b), and MoS<sub>2</sub>/Histidino/CV.

**3.15. pav.** Gryno MoS<sub>2</sub> (a), MoS<sub>2</sub>/Histidino (b) ir MoS<sub>2</sub>/Histidino/CV (c) Nyquist grafikai.

Further investigation of fabricated MoS<sub>2</sub> electrode HER performance was carried out via electrochemical impedance spectroscopy. The electrochemical impedance spectra were recorded at -0.2 V, -0.25 V, and -0.3 V to portray the increasing HER rate. At more negative potentials, the generated H<sub>2</sub> bubbles started to disturb the signal acquisition, therefore EIS at -0.35 V was not carried out. In the obtained Nyquist plots (Fig. 3.15) two semi-circles were distinguished in the measured potential range, with the second semi-circle becoming more apparent at higher potentials. The shapes of obtained spectra at a given potential appear similar for all investigated electrodes. This indicates that the mechanism of HER does not change, which corresponds well with the calculated Tafel slopes, where Volmer-Heyrovsky mechanism was predicted by the values of Tafel slopes for both MoS<sub>2</sub>, and MoS<sub>2</sub>/Histidine.

Both MoS<sub>2</sub>/Histidine and MoS<sub>2</sub>/Histidine/CV (electrode, subjected to 1000 potential scan cycles prior to EIS) electrodes exhibited lower impedance magnitudes at a given potential, compared to pure MoS<sub>2</sub>, signifying higher electrocatalytic activity.

As two capacitive regions were determined, the system was described using an equivalent electric circuit (EEC) with two components, one of which is attributable to electrical double layer capacitance  $C_{dl}$ , while the other,  $C_p$ , is related to the adsorption of hydrogen onto MoS<sub>2</sub> (Inset of Fig. 3.15. a). This EEC is frequently used when describing electrode processes involving one adsorbed species with subsequent desorption with  $R_p > 0$  [158]. According to Castro *et al.*, this EEC is adequate when used to simulate EIS data at higher HER overpotentials (~ -0.25 V) [159]. Surface inhomogeneity was taken into account by using constant phase elements (CPE) instead of capacitance in the EEC. The calculated EEC parameters are presented in Table 2. Calculation of  $C_p$  values was carried out using Brug *et al.*'s equation (Eq. 2) [160]:

$$C_p = T_p^{\frac{1}{n}} \left( \frac{1}{R_s + R_{ct}} + \frac{1}{R_p} \right)^{1-\frac{1}{n}} \quad (2)$$

where  $T_p$  are the values of CPE<sub>p</sub> element,  $n$  is the constant phase exponent, and  $R_{ct}$ ,  $R_s$ , and  $R_p$  are, respectively, the charge transfer, uncompensated solution and polarization resistances. The value of charge transfer resistance  $R_{ct}$  is inversely proportional to the rate of the reaction, i.e. lower  $R_{ct}$  results in higher hydrogen evolution reaction rate. Lower values of  $R_{ct}$  were observed for pure MoS<sub>2</sub> electrodes rather than for MoS<sub>2</sub>/Histidine, however MoS<sub>2</sub>/Histidine/CV also exhibited lower  $R_{ct}$  values, which was especially evident at higher potentials, inferring that the reaction rate increases during HER processing. The pseudocapacitance  $C_p$  is influenced by surface coverage of adsorbed species, which in the case of HER is H<sub>ads</sub>. According to Lasia [161], as the overpotential increases, the surface coverage  $\theta_H$  approaches unity, which indicates that  $C_p$  values should either increase or stabilize at higher overpotentials. However, the opposite was observed for MoS<sub>2</sub> electrodes with histidine. Highest  $C_p$  values were observed for MoS<sub>2</sub>/Histidine, while the lowest were, expectedly, observed for pure MoS<sub>2</sub>. At -0.2 V the MoS<sub>2</sub>/Histidine electrode had exhibited  $C_p$  values three times larger than pure MoS<sub>2</sub> (150.10 mF cm<sup>-2</sup> and 49.59 mF cm<sup>-2</sup>, respectively), which indicates that the addition of histidine to the hydrothermal synthesis solution results in a greater quantity of HER active sites at fabricated MoS<sub>2</sub> films. After HER processing, the  $C_p$  values were substantially lower, which suggests that the catalytically active surface of MoS<sub>2</sub> is affected during HER.

**Table 2.** EEC parameters obtained by fitting EIS data. **2 lentelė.** Apskaiciuoti ekvivalentinės grandinės parametrai

$E$ (vs SHE)	$R_s, \Omega \text{ cm}^2$	$CPE_{dl}, \text{F cm}^{-2}$ $S^{(\alpha-1)}$	$\alpha_{CPEll}$	$R_{ct}, \Omega \text{ cm}^2$	$CPE_p, \text{F cm}^{-2}$ $S^{(\alpha-1)}$	$\alpha_{CPEp}$	$R_p, \Omega \text{ cm}^2$	$C_p, \text{F cm}^{-2}$	$\chi^2 (\times 10^{-3})$
<b>MoS<sub>2</sub></b>									
-0.2 V	0.61	0.015	0.69	0.11	0.072	0.89	18.36	0.050	1.65
-0.25 V	0.62	0.0090	0.72	0.10	0.070	0.91	1.30	0.051	2.22
-0.3 V	0.59	0.0015	0.79	0.089	0.091	0.87	0.40	0.051	7.18
MoS <sub>2</sub> /Histidine									
-0.2 V	0.65	0.024	0.61	0.16	0.20	0.86	8.26	0.150	1.55
-0.25 V	0.69	0.011	0.68	0.12	0.19	0.88	0.96	0.136	1.53
-0.3 V	0.84	0.012	0.54	0.12	0.18	0.81	0.50	0.092	2.49
MoS <sub>2</sub> /Histidine/CV									
-0.2 V	0.69	0.020	0.66	0.13	0.090	0.88	7.75	0.062	2.65
-0.25 V	0.74	0.0047	0.79	0.089	0.11	0.85	0.91	0.063	0.89
-0.3 V	0.84	0.008	0.65	0.081	0.15	0.76	0.40	0.057	7.05

Lastly, the polarization resistance  $R_p$  was determined to markedly decrease when the potential was increased for all investigated electrodes. The most notable decrease was observed for pure MoS<sub>2</sub>, despite the fact that the  $R_p$  value of pure MoS<sub>2</sub> at -0.2 V was more than twofold higher than the  $R_p$  values observed for MoS<sub>2</sub> with histidine. Furthermore, the  $R_p$  of MoS<sub>2</sub>/Histidine/CV were lower than MoS<sub>2</sub>/Histidine at all measured potentials, which indicates that the H<sub>2</sub> adsorption/desorption rate increases after prolonged HER processing at MoS<sub>2</sub> electrodes.

As mentioned in section 1.3., the electrochemically active surface area has an influence on the hydrogen evolution reaction. Due to the nature of hydrothermally fabricated MoS<sub>2</sub> electrodes, the exact surface area can hardly be estimated. Nevertheless, double layer capacitance ( $C_{dl}$ ) can be used as an indicator to evaluate the interfacial area between an electrolyte and the surface of the electrode. To determine the  $C_{dl}$ , cyclic voltammetry was used in the potential range of -0.10 V – 0.10 V (Fig. 3.16.) with various scan rates ( $v = 25, 50, 75, 100, 125, 150, 175, 200 \text{ mV s}^{-1}$ ), where the current response is mostly due to the charging of the double layer.

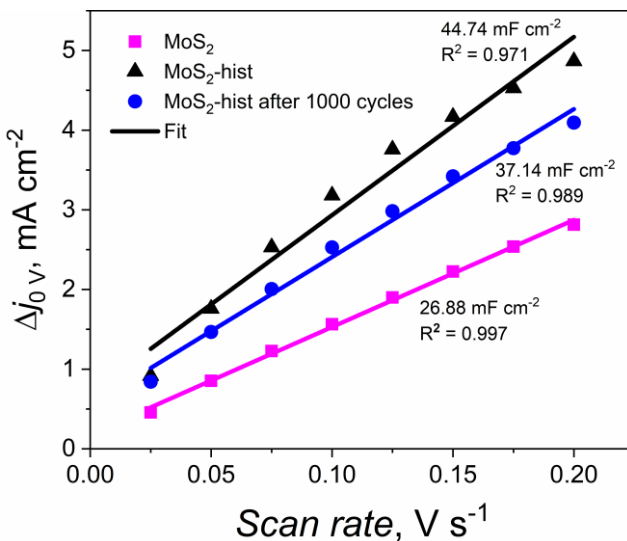


**Figure 3.16.** Current density difference  $\Delta j$  at 0 V plotted vs. the scan rate.

**3.16. pav.** Srovės tankio skirtumo ( $\Delta j$ ) ties 0V priklausomybė nuo skleidimo greičio.

The double-layer capacitance was estimated by plotting the current density difference  $\Delta j$  ( $j_a - j_c$ ) at 0 V against the scan rate, where the slope is double  $C_{dl}$ . The lowest  $C_{dl}$  ( $26.88 \text{ mF cm}^{-2}$ ) was determined from Fig. 3.16. to be for pure MoS<sub>2</sub>. Synthesis of MoS<sub>2</sub> with histidine significantly increases the

$C_{dl}$  (44.74 mF cm<sup>-2</sup>). However, utilization of MoS<sub>2</sub>/Histidine electrodes for prolonged HER results in a decrease of  $C_{dl}$  to 37.14 mF cm<sup>-2</sup>, indicating the deterioration of electrochemically active surface area.

### 3.3.3. Characterization of MoS<sub>2</sub>/Histidine films

The elemental composition of the fabricated electrode surface before and after cyclic voltammetry measurements was investigated using XPS. The obtained Mo 3d spectra are shown in Fig. 3.17. The obtained Mo 3d spectra were typically deconvoluted into four doublets with Mo 3d<sub>5/2</sub> and 3d<sub>3/2</sub> components. The doublet possessing the highest intensity with 3d<sub>5/2</sub> and 3d<sub>3/2</sub> components at 228.6 eV and 231.8 eV, respectively, was ascribed to Mo<sup>4+</sup> of 1T-MoS<sub>2</sub>, the second Mo<sup>4+</sup> doublet with components at 229.4 eV and 232.5 eV to 2H-MoS<sub>2</sub>, and the third Mo<sup>4+</sup> doublet with components at 230.6 eV and 233.8 eV to MoO<sub>2</sub>. The last doublet was ascribed to Mo<sup>6+</sup> of MoO<sub>3</sub>, with 3d<sub>5/2</sub> and 3d<sub>3/2</sub> components at 232.8 eV and 235.9 eV, respectively.

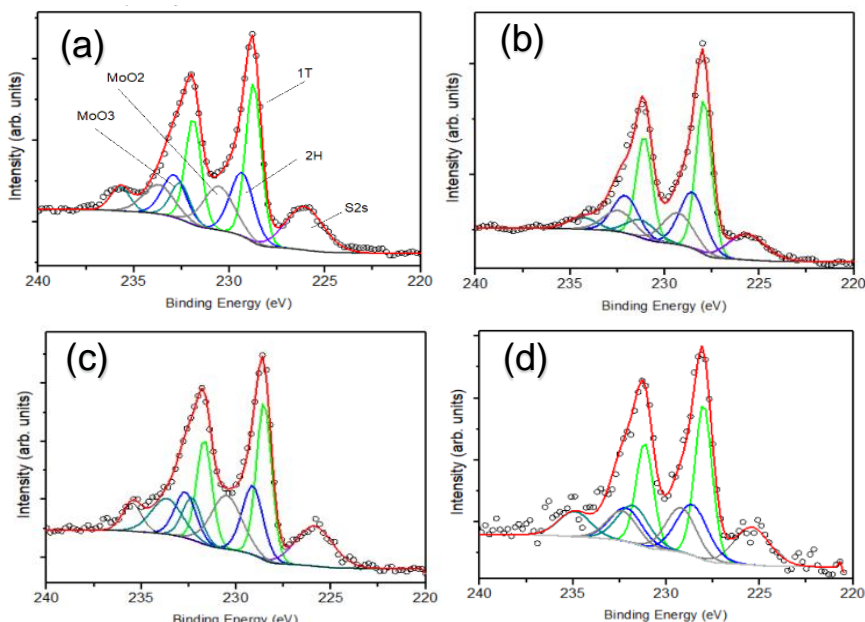


**Figure 3.17.** Mo 3d X-ray photoelectron spectra of MoS<sub>2</sub>/Histidine electrodes before (a) and after ion irradiation (c), and after CV for 50 (b), and 2000 (d) potential scan cycles.

**3.17. pav.** MoS<sub>2</sub>/Histidino elektrodų prieš (a) ir po paviršiaus valymo (c), bei po CV matavimų praskleidus 50 (b) ir 2000 ciklų (d) Mo 3d Rentgeno fotoelektronų spektrai.

As a layer of carbon was detected after continuous HER processing, mild ion irradiation was used to remove the carbon layer from the surface of the electrode. Photoelectrons from carbon were still detected after ion irradiation, suggesting that a thin layer or non-uniform regions of carbon were deposited on MoS<sub>2</sub> films with histidine.

A comparison of the calculated 1T relative content from Mo 3d spectra before and after CV, and ion irradiation is provided in Table 3. No significant difference in the content of 1T-MoS<sub>2</sub> phase was detected for the samples before and after CV measurements, which implies that the 1T phase is stabilized and does not readily transform to 2H during HER processing.

**Table 3.** The 1T-MoS<sub>2</sub> phase relative content (at. %), calculated from Mo 3d spectra of MoS<sub>2</sub>/Histidine with and without ion irradiation, before and after CV measurements.

**3 lentelė.** Santykinis 1T-MoS<sub>2</sub> fazės kiekis (at. %) apskaičiuotas iš MoS<sub>2</sub>/Histidino Mo 3d spektrų prieš ir po CV matavimų bei paviršiaus valymo.

Mo 3d ratio	1T	Before cycling	After 50 cycles	After 2000 cycles
Before irradiation	ion	61	60	60
After irradiation	ion	52	51	52

For evaluation of possible intercalation of guest species, FTIR spectroscopy was carried out. In the obtained FTIR spectra (Fig. 3.18), the band located at 605-607 cm<sup>-1</sup> was ascribed to Mo-S stretching, while the band at 928 cm<sup>-1</sup> represents S-S bonding [162]. The prominent band at 1394 cm<sup>-1</sup> for pure MoS<sub>2</sub> was ascribed to deformational N-H vibrations, while this band for MoS<sub>2</sub>/Histidine is shifted to 1400-1402 cm<sup>-1</sup>. The bands in the 750-1000 cm<sup>-1</sup> region indicate Mo-O coordination, with the band at 1090 cm<sup>-1</sup> ascribed to terminal stretch vibration of Mo-O [163]. Two broad low-intensity bands at ~1630 cm<sup>-1</sup> and ~1670 cm<sup>-1</sup> were observed for samples with histidine, and were assigned to C=O stretching in amides, indicating peptide bonding. Moreover, the band at ~1230 cm<sup>-1</sup> could be ascribed to CN stretching and NH bending vibrations in amides, while the band at 574 cm<sup>-1</sup> could be assigned to C=O out-of-plane bending in amides [164].

According to Weiss *et al.* [157], histidine molecules may undergo a condensation reaction when heated to 220 °C during hydrothermal synthesis,

with the N-terminus and C-terminus of adjacent histidine molecule reacting to form a planar peptide bond. The appearance of bands, attributable to peptide bonding suggest this to be the case. It is possible that these residues from thermal decomposition of histidine could adsorb onto MoS<sub>2</sub> nanoflakes and thus lead to improved stability of 1T-MoS<sub>2</sub>, correlating well with the XPS and electrochemical investigation results, along with intercalation of charged guest species or fragments as observed via HRTEM.

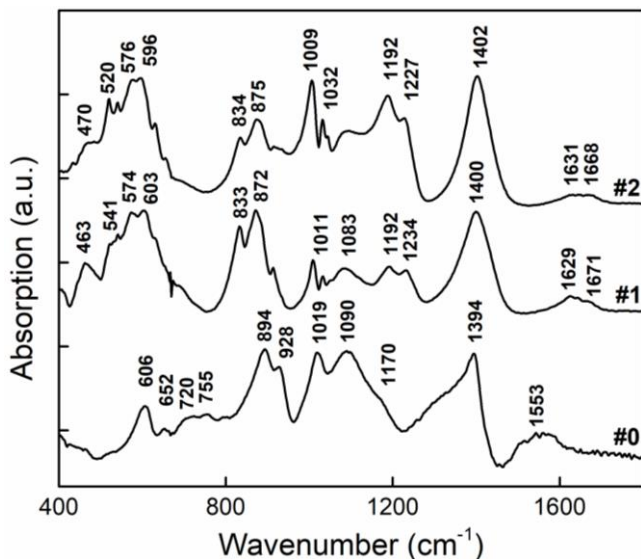


**Figure 3.18.** FTIR spectra of: pure MoS<sub>2</sub> (#0), MoS<sub>2</sub>/Histidine (#1), and MoS<sub>2</sub>/Histidine after drying for 12 h at 60 °C (#2).

**3.18. pav.** Gryno MoS<sub>2</sub> (#0), MoS<sub>2</sub>/Histidino (#1), ir išdžiovino 12 val. ties 60 °C MoS<sub>2</sub>/Histidino (#2) FTIR spektrai

### 3.4. Improving the HER performance of hydrothermally synthesized MoS<sub>2</sub> via anodic pretreatment

In addition to modification of hydrothermal synthesis, various post-synthesis treatment methods, such as electrochemical incorporation of sulfur vacancies [165], application of an external electric field [166], or engineering of grain boundaries via laser irradiation [167] could be employed to modify hydrothermally synthesized MoS<sub>2</sub>, leading to enhanced HER activity of MoS<sub>2</sub> electrocatalysts.

In this study, the MoS<sub>2</sub>/Cysteine electrodes were fabricated via hydrothermal synthesis onto anodized Ti substrates by the same procedure as the electrodes reported in sections 2.4. and 3.2., which were then subjected to

*in situ* anodic pretreatment prior to HER measurements. Anodic pretreatment was carried out by applying a positive potential to the working electrode ( $\text{MoS}_2/\text{Cysteine}$ ), by linear sweep voltammetry, or by cyclic voltammetry, as described previously, with the potential range expanded to encompass the anodic region. In the latter case, the potential was initially swept towards the anodic region before being shifted to the cathodic region.

### 3.4.1. Anodic pretreatment and electrochemical investigation of $\text{MoS}_2/\text{Cysteine}$ electrodes

Anodic sweeps from -0.2 V to +2.0 V were applied to the  $\text{MoS}_2/\text{Cysteine}$  electrodes and the obtained current-voltage curves are shown in Fig. 3.19.

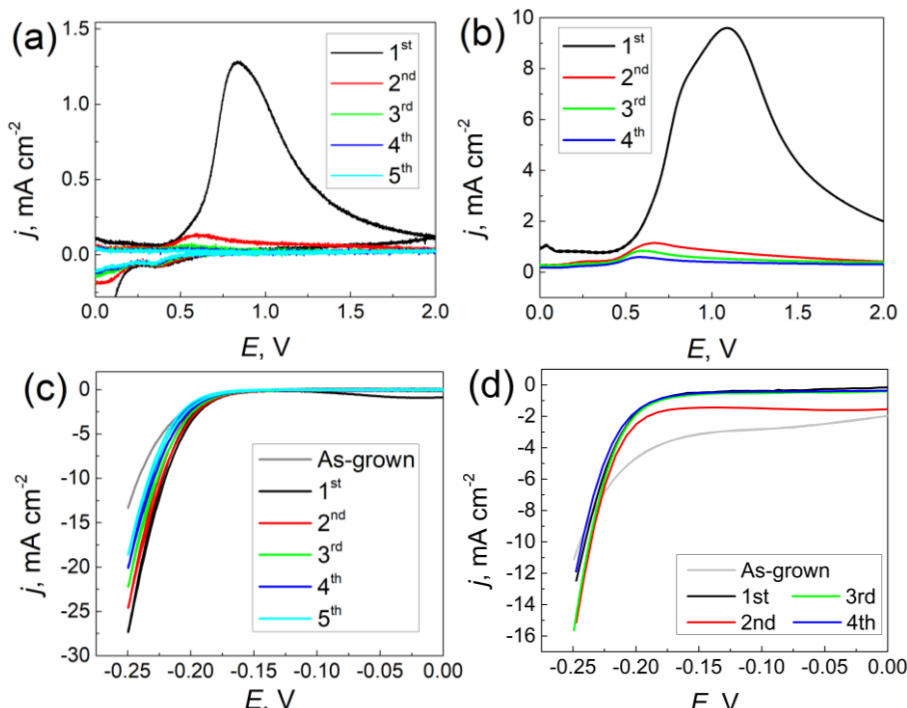


**Figure 3.19.** Anodic (a,b), and cathodic (c,d) curves of  $\text{MoS}_2/\text{Cysteine}$  obtained by CV in the -0.25 V – +2.0 V potential range at 0.5 mV s<sup>-1</sup> (a,c), and 10 mV s<sup>-1</sup> (b,d) scan rates. Numbers in the legend indicate anodic pretreatment cycle.

**3.19. pav.**  $\text{MoS}_2/\text{Cysteine}$  anodinės (a,b), bei katodinės (c,d) kreivės, gautos CV metu potencialą skleidžiant 0.5 mV s<sup>-1</sup> (a,c), bei 10 mV s<sup>-1</sup> (b,d) greičiu. Legendoje pateikti numeriai nurodo anodinio apdorojimo ciklų skaičių.

During the first anodic cycle (Fig. 3.19. a,b), an anodic peak is observed at  $\sim +1.0$  V, decreasing markedly during the following cycles. These findings correlate with Bonde *et al.* report [168], although no decrease in HER performance was observed, in contrast to what Bonde *et al.* reported. Contrarily, the MoS<sub>2</sub>/Cysteine electrode exhibited enhanced HER activity after first anodic pretreatment cycle, and the electrode retained the activity even after subsequent anodic pretreatments, where the anodic current density approaches zero. According to the aforementioned report, the decrease of the anodic current peak should indicate a decrease of MoS<sub>2</sub> content on the substrate, yet, no indication of damage to the MoS<sub>2</sub>/Cysteine samples was observed and the pretreated samples were found to possess higher HER activity, compared to as-grown MoS<sub>2</sub>/Cysteine.

It was also established that varying the anodic switching potential ( $E_{\text{switch}}$ ), i.e. the potential, at which the CV scan changes direction, during anodic pretreatment within a narrower potential range (Fig. 3.20. a) affected the HER activity during subsequent cathodic potential scans (Fig. 3.20. b).

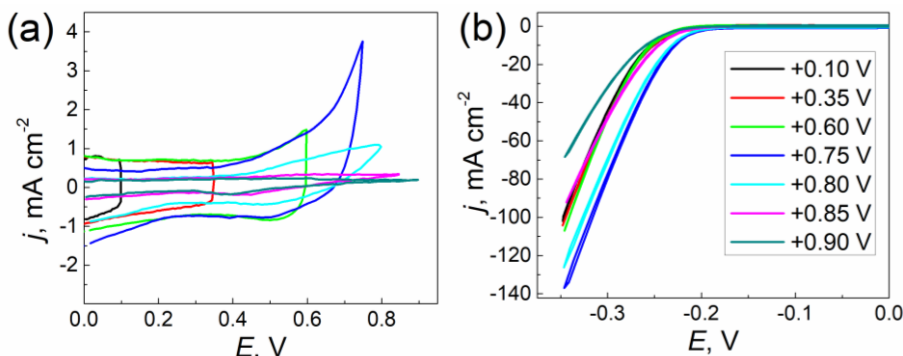


**Figure 3.20.** Anodic (a) and cathodic (b) region of cyclic voltammograms of MoS<sub>2</sub>/Cysteine electrode continuously cycled from -0.35 V to incrementally increased anodic potential range. The depicted curves are averaged from 10 CV cycles for every switching potential value.

**3.20. pav.** MoS<sub>2</sub>/Cisteino ciklinės voltamperogramos anodinė (a) bei katodinė (b) dalis. Voltamperogramos užrašytos nuo -0.35 V iki laipsniškai keičiamo anodino potencijalo ruožo. Pavaizduotos kreivės atitinka 10 ciklų vidurkį kiekvienai posūkio potencijalo vertei.

When the polarization was increased to +0.55 V, the HER efficiency either remained the same or decreased insignificantly compared to the pre-polarization values. However, when the  $E_{\text{switch}}$  was set to +0.6 V or more, enhanced HER activity was observed, with the most significant increase

observed after anodic pretreatment to +0.75 V. It was reported by Kautek *et al.* that the corrosion of MoS<sub>2</sub> edges is observed when 2D-MoS<sub>2</sub> nanoplatelet films are anodically treated in acidic solutions [169]. On that account, the anodic peak, observed at ~ +0.85 V could signify electrochemical MoS<sub>2</sub> edge etching, where the current density is proportional to the length of MoS<sub>2</sub> edges, and the peak potential depends on the anodic scan rate.

The interpretation of the second peak, observed at higher scan rate (Fig. 3.19. b) is unclear. As mentioned in reference [168], it may possibly be linked to the etching of the MoS<sub>2</sub> basal plane. However, it is important to note that MoS<sub>2</sub> etching involves not only the oxidation of molybdenum ( $\text{Mo}^{4+} \rightarrow \text{Mo}^{6+}$ ), but simultaneous oxidation of sulfur is also plausible ( $\text{S}^{2-} \rightarrow \text{S}_2^{2-}$ ;  $\text{S}_2^{2-}$  and/or  $\text{S}^{2-} \rightarrow \text{SO}_4^{2-}$ ). As a result, the anodic curve may exhibit additional peaks that could be attributed to sulfur oxidation. Kautek *et al.* did not observe etching of MoS<sub>2</sub> basal plane at +1.2 V [169], and the second peak was not distinguished in this work when lower scan rates were applied (Fig. 3.19. a). This implies that the determined increase in HER activity of MoS<sub>2</sub>/Cysteine electrodes after anodic pretreatment cannot be linked with the increase in active edge quantity via etching of the basal plane. Most likely the HER activity increase could be attributed to an increase in activity or length of MoS<sub>2</sub> nanoplatelet edges.

The reduction of HER activity after prolonged anodic pretreatment could stem from a decrease of MoS<sub>2</sub> nanoplatelet quantity on the TiO<sub>2</sub> surface or the deactivation of MoS<sub>2</sub> edges caused by the destruction of energetically more active HER positions. As reported by Kibsgaard and coworkers [170], a constant Tafel slope value and decreasing exchange current density values are observed if the electrochemically active surface area of the electrocatalyst decreases without a change in the hydrogen adsorption free energy ( $\Delta G_{\text{H}^*}$ ). Calculated Tafel slope ( $b$ ) and exchange current density ( $j_0$ ) values are presented in Table 4. It was determined from CV, that the Tafel slope did not significantly change in the +0.1 V to +0.55 V  $E_{\text{switch}}$  region. Further increase of  $E_{\text{switch}}$  resulted in a decrease of Tafel slope values, and remained relatively constant in the +0.8 V to +0.9 V  $E_{\text{switch}}$  region. The exchange current density increased up to +0.75 V, while a rapid decrease was observed at higher switching potentials. The initial increase of  $j_0$  could be attributed to an increase in HER active site quantity, while the subsequent decrease of  $j_0$  and a stable Tafel slope suggest that only the active surface area of the electrocatalyst is decreasing. Different Tafel slopes for as-grown and anodically pretreated MoS<sub>2</sub>/Cysteine infer a change in the rate-determining step of HER, and possibly a change in the characteristics of active positions, since the HER activity is directly influenced by the  $\Delta G_{\text{H}^*}$  of active positions.

**Table 4.** Tafel slope and exchange current density values of HER at various switching potentials of anodic polarization

**4 lentelė.** Tafel nuolinkio kampo bei HER mainų srovės vertės esant skirtiniems posūkio potencialams

$E_{\text{switch}}$ , V	0.55	0.60	0.65	0.70	0.75	0.80	0.85	0.9
$b$ , mA dec <sup>-1</sup>	56.5	52.9	49.7	48.9	47.2	46.0	44.2	45.1
$j_0$ , $\mu\text{A cm}^{-2}$	1.12	1.32	1.78	2.63	3.54	0.76	0.30	0.18

Constant anodic potential impulses were also applied to study the influence of passed charge on the increase of HER activity of MoS<sub>2</sub>/Cysteine electrodes (Fig. 3.21.). Initially, both the passed charge and the HER activity of the fabricated electrode increased (Fig. 3.21. a), while a decrease of passed charge during each subsequent anodic impulse was observed after the fourth anodic impulse. Only a slight HER activity decrease was observed after nine anodic potential impulses and subsequent HER processing, with the cathodic current density decreasing by ~10 mA cm<sup>-2</sup> from the maximum obtained current density throughout the course of the experiment (Fig. 3.21. b). This could be ascribed to the saturation of energetically more active positions at MoS<sub>2</sub> edges.

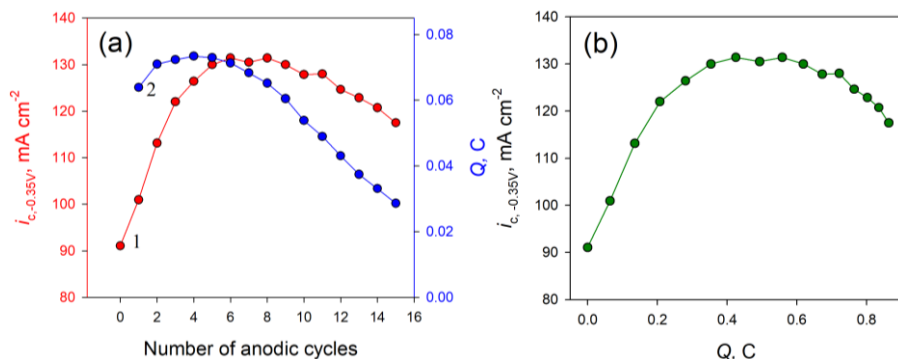


**Figure 3.21.** HER current density at -0.35 V after each anodic polarization cycle (a curve 1) and values of charge passed during anodic polarization cycles (15 s at +0.72 V) of MoS<sub>2</sub>/Cysteine (a curve 2). The dependence of HER current density at -0.35 V on the total passed charge during anodic pretreatment is depicted in (b).

**3.21. pav.** HER srovės tankis ties -0.35 V po kiekvieno anodinio poliarizavimo ciklo (a 1 kreivė) ir pratekėjusio krūvio vertė anodinio poliarizavimo (15 s at +0.72 V) metu (a 2 kreivė). HER srovės tankio priklausomybė nuo suminio pratekėjusio krūvio pateikta (b) grafike.

### 3.4.2.Characterization of anodically pretreated MoS<sub>2</sub>/Cysteine electrodes

It was determined from SEM images (Fig. 3.22.) that the MoS<sub>2</sub>/Cysteine film uniformly covers the whole Ti/TiO<sub>2</sub> surface, and is very similar to the films described in Section 3.2. After anodic pretreatment at +0.72 V for 12 minutes, the film surface appears to remain unchanged, with the only difference being the emergence of a few cracks in the MoS<sub>2</sub>/Cysteine film (Fig. 3.22. b). When the anodic potential was increased further to +2.5 V, the morphology of the film changed significantly, as a partial loss of MoS<sub>2</sub> nanoplatelets was observed. The S/Mo ratio was determined via EDX to be 1.93 – 2.03 for both as-grown MoS<sub>2</sub>/Cysteine, and the electrodes after anodic pretreatment at +0.72 V for 12 minutes.

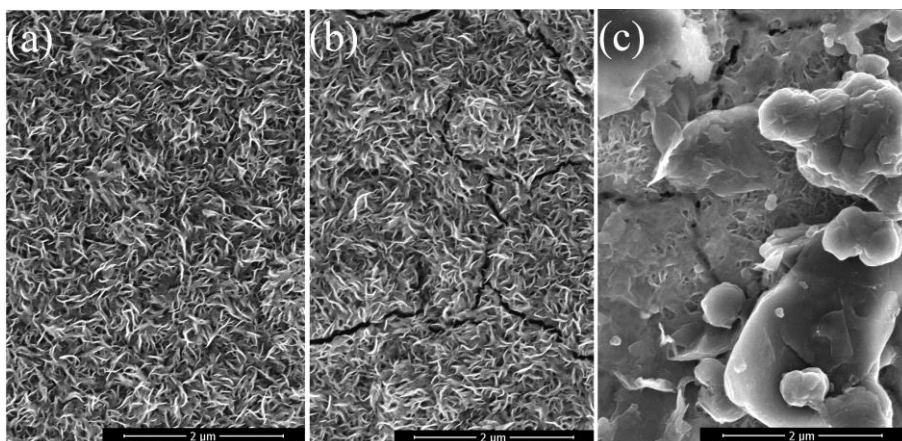


**Figure 3.22.** Top-side SEM images of MoS<sub>2</sub>/Cysteine films before (a), and after anodic pretreatment at +0.72 V for 12 min. (b), and CV scan to +2.5 V at 0.5 mV s<sup>-1</sup> scan rate (c).

**3.22. pav.** MoS<sub>2</sub>/Cisteino prieš (a), ir po anodinio apdorojimo ties +0.72 V 12 min. (b), bei po CV skleidimo iki +2.5 V skleidžiant 0.5 mV s<sup>-1</sup> greičiu (c) SEM nuotraukos.

XPS was used to investigate any compositional changes to the surface of MoS<sub>2</sub>/Cysteine after anodic pretreatment in the 0.5 M H<sub>2</sub>SO<sub>4</sub> electrolyte. The S/Mo ratio from the XPS was determined to be 2.05 for as-grown MoS<sub>2</sub>/Cysteine, while the ratio for anodically polarized to +2.5 V sample increased to 3.32. The S/Mo ratio dependence on the anodic pretreatment potential is shown in Fig. 3.23. It was determined that the S/Mo ratio and the relative content of bridging S<sub>2</sub><sup>2-</sup> and apical S<sup>2-</sup> groups increases when the

anodic potential is increased, regardless of the duration of polarization. The S/Mo ratio variations, obtained via EDX and XPS, suggest that the increase of HER activity should not stem from the formation of sulfur vacancies during anodic pretreatment.

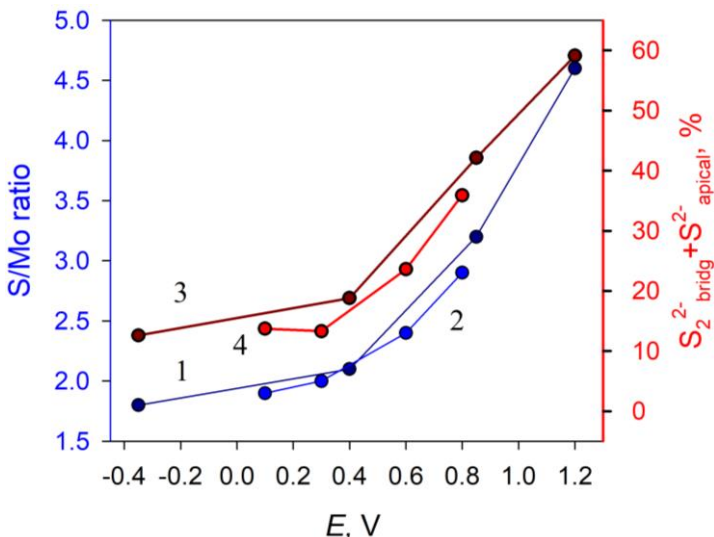


**Figure 3.23.** Variation of S/Mo ratio (1,2) and relative quantity of bridging  $S_2^{2-}$  and apical  $S^{2-}$  groups (3,4) due to varying applied anodic pretreatment potential for 15 s (1,3), and 900 s (2,4).

**3.23. pav.** S/Mo santykio (1,2) bei santykinio tiltelinių  $S_2^{2-}$  ir viršūninių  $S^{2-}$  grupių kiekių (3,4) priklausomybė nuo anodinio apdorojimo potencialo, kuomet apdorojimo trukmė 15 s (1,3), ir 900 s (2,4).

The Mo 3d and S 2p spectra (Fig. 3.24.) were subjected to deconvolution, fitting the spectra with doublets corresponding to Mo  $3d_{5/2}$  and  $3d_{3/2}$  for the Mo 3d spectrum, and S  $2p_{3/2}$  and  $2p_{1/2}$  for the S 2p spectrum. The binding energies for the Mo  $3d_{5/2}$  and S  $2p_{3/2}$  peaks are provided in Table 5. Note, that the Mo  $3d_{3/2}$  and S  $2p_{1/2}$  peak binding energies are not listed – this was done intentionally to keep Table 5 less cumbersome, as these components have a constant binding energy separation of 3.15 eV for Mo  $3d_{3/2}$  and 1.16 eV for S  $2p_{1/2}$ .

According to the literature, the Mo  $3d_{5/2}$  BE of pristine 2H-MoS<sub>2</sub> cleaved in vacuum equaled to 229.1 eV – 229.4 eV, whereas BE of S  $2p_{3/2}$  – 162.0–162.4 eV [69]. Intercalation of Li<sup>+</sup> into 2H-MoS<sub>2</sub> structure invokes the appearance of additional peaks in the Mo 3d and S 2p spectra, with the BE of the former peak being 1.1 eV and the latter 0.8 eV lower than the peaks of pristine 2H-MoS<sub>2</sub> [68]. After exfoliation with butyl-lithium derivatives and

leaching of Li, various BE of Mo 3d and S 2p spectra have been reported, with the spectra unchanged from pristine 2H-MoS<sub>2</sub> [171], comprising of broader peaks with their BE unaltered [172] or with additional peaks appearing at 0.8–0.9 eV lower BE [39, 70].

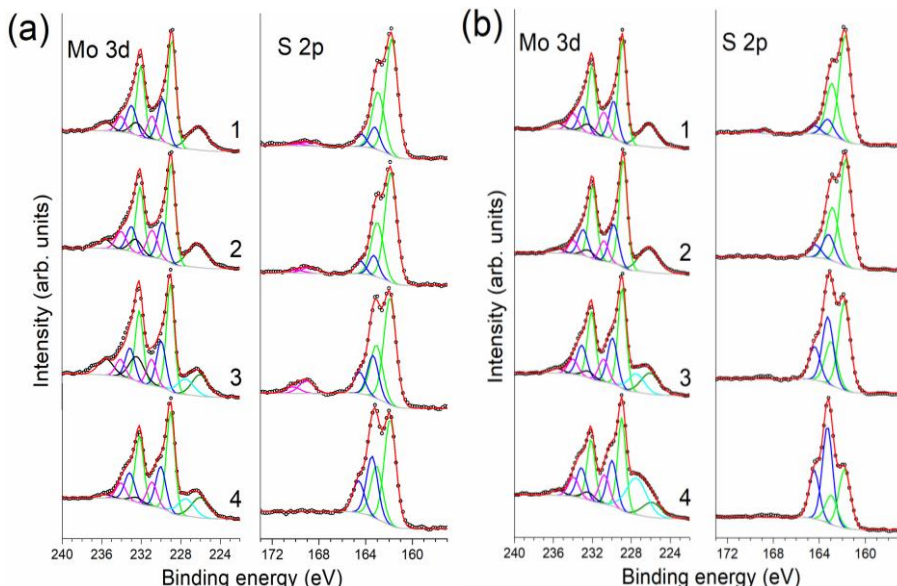


**Figure 3.24.** Deconvoluted Mo 3d and S 2p X-ray photoelectron spectra of MoS<sub>2</sub>/Cysteine electrodes after anodic pretreatment. Samples treated for 900 s (a) at +0.1 V (a1), +0.3V (a2), +0.6V (a3), +0.8 V (a4) and treated for 15 s (b) at -0.35 V (b1) +0.40 V (b2), +0.85 V (b3), and +1.2 V (b4).

**3.24. pav.** Išskaidyti MoS<sub>2</sub>/Cisteino elektrodų Mo 3d ir S 2p Rentgeno fotoelektronų spektrai po anodinio apdorojimo. Pavyzdžiai apdoroti 900 s (a) ties +0.1 V (a1), +0.3V (a2), +0.6V (a3), +0.8 V (a4) bei apdoroti 15 s (b) ties -0.35 V (b1) +0.40 V (b2), +0.85 V (b3), ir +1.2 V (b4).

In the case of hydrothermally synthesized 2D-MoS<sub>2</sub>, observation of one [173] or multiple doublets were reported [174, 175]. The Mo 3d and S 2p XPS peaks distinguished at lower binding energies than the aforementioned pristine 2H-MoS<sub>2</sub> are frequently attributed to the formation of the 1T-MoS<sub>2</sub> phase or distorted 1T'-MoS<sub>2</sub> phase. Other than Mo<sup>6+</sup> 3d<sub>5/2</sub> component at ~232.8 eV, higher Mo 3d and S 2p binding energies (229.7 eV – 230.4 eV, and 163.0 eV – 163.6 eV for Mo 3d and S 2p, respectively) were also elucidated. The peaks in the mentioned region of Mo 3d are commonly attributed to Mo<sup>5+</sup> of sulfides, oxides, or oxysulfides [71, 176, 177], while the S 2p peaks at higher binding energies are indicative of amorphous MoS<sub>x</sub>, where 2<x<6. For amorphous molybdenum sulfides, the S 2p<sub>3/2</sub> peaks at 163.1 eV – 163.5 eV could be

ascribed to bridging  $S_2^{2-}$  and apical  $S^{2-}$  groups, while the peaks at 161.6 eV – 161.8 eV could be ascribed to unsaturated  $S^{2-}$  and terminal  $S_2^{2-}$  groups [178, 179].

**Table 5.** Deconvoluted X-ray photoelectron spectra Mo 3d<sub>5/2</sub> and S 2p<sub>3/2</sub> component peak positions of MoS<sub>2</sub>/Cysteine nanoplatelet surface after anodic polarization. The numbering of the samples is the same as in Figure 3.24.

**5 lentelė.** Išskaidytų anodiškai apdoroto MoS<sub>2</sub>/Cisteino elektrodų Rentgeno fotoelektronų spektrų Mo 3d<sub>5/2</sub> ir S 2p<sub>3/2</sub> komponentų smailių padėtys. Pavyzdžių numeracija tokia pat, kaip ir 3.24. pav. legendoje. BE – ryšio energija, A – sanykinis smailės plotas.

Sample #	Mo 3d <sub>5/2</sub>		S 2p <sub>3/2</sub>		#	Mo 3d <sub>5/2</sub>		S 2p <sub>3/2</sub>	
	BE, eV	Area, %	BE, eV	Area, %		BE, eV	Area, %	BE, eV	Area, %
a1	228.9	52.0	161.8	82.2	b1	228.9	54.0	161.8	84.9
	229.8	25.5	163.2	13.7		229.8	22.5	163.3	12.6
	230.9	12.8	168.8	4.1		230.8	16.2	168.8	2.5
	232.4	9.7				232.4	7.3		
a2	228.9	50.2	161.8	81.2	b2	228.8	57.9	161.7	81.2
	229.8	21.9	163.3	13.3		229.8	24.6	163.2	18.8
	230.9	17.4	169.1	5.5		230.8	11.8		
	232.5	10.5				232.4	5.7		
a3	229.0	44.8	161.9	66.8	b3	228.9	52.1	161.8	57.9
	230.0	22.9	163.4	23.6		229.9	28.6	163.3	42.1
	230.9	12.7	169.1	9.6		230.8	14.1		
	232.4	19.6				232.4	5.2		
a4	229.0	54.1	161.9	64.1	b4	229.0	47.6	161.8	40.9
	230.0	26.7	163.4	35.9		230.0	27.3	163.3	59.1
	230.9	15.1				230.8	18.9		
	232.4					232.4	6.2		

In the Mo 3d spectra (Fig. 3.24.), the 3d<sub>5/2</sub> component with the lowest binding energy (228.8 eV – 229.0 eV) was ascribed to Mo<sup>4+</sup> of 1T-MoS<sub>2</sub>, and the 3d<sub>5/2</sub> peak at 229.7 eV – 230.0 eV BE was ascribed to Mo<sup>4+</sup> of 2H-MoS<sub>2</sub>. Peaks with higher binding energies were also distinguished, with the 3d<sub>5/2</sub> component peak at 230.8 eV – 230.9 eV ascribed to Mo<sup>5+</sup> of molybdenum oxide, oxysulfide or sulfide, while the peak at 232.4 eV – 232.5 eV was ascribed to Mo<sup>6+</sup> of MoO<sub>3</sub>. It is reported that Mo<sup>5+</sup> compounds could be observed as intermediates in the sulfidation reaction of (NH<sub>4</sub>)<sub>2</sub>Mo<sub>7</sub>O<sub>24</sub> [180], MoO<sub>3</sub> [181], and the thermal decomposition of molybdates [182], inferring

that Mo<sup>5+</sup> compounds, for instance, MoO<sub>x</sub>S<sub>4-x</sub><sup>2-</sup> [183], MoS<sub>4</sub><sup>2-</sup>, MoS<sub>3</sub> [122], [Mo<sub>2</sub>S<sub>12</sub>]<sup>2-</sup>, [Mo<sub>3</sub>S<sub>13</sub>]<sup>2-</sup> [184, 185] could be anticipated to form during hydrothermal synthesis of MoS<sub>2</sub>/Cysteine. The S 2p spectra were fitted with two doublets, with the S 2p<sub>3/2</sub> component peak at 161.6 eV – 161.9 eV found at slightly lower binding energies than those of pure 2H-MoS<sub>2</sub> (~162.2 eV), however, the binding energy values are close to those ascribed to terminal S<sub>2</sub><sup>2-</sup> and unsaturated S<sup>2-</sup> groups. The second doublet at 163.2 eV – 163.4 eV could be ascribed to bridging S<sub>2</sub><sup>2-</sup> and apical S<sup>2-</sup> groups, while in some samples a low-intensity third doublet at ~169 eV is observed, which stems from SO<sub>x</sub>, formed due to sample oxidation during storage.

No links between the different applied potentials or the duration of anodic pretreatment and the Mo 3d and S 2p X-ray photoelectron spectra were distinguished, with the only notable exception being the peak area increase of S 2p<sub>3/2</sub> component at 163.2 – 163.4 eV with an increase of applied anodic potential (Fig. 3.24. and Table 5). This implies that the HER activity increase of MoS<sub>2</sub>/Cysteine should be attributed to the increase of bridging S<sub>2</sub><sup>2-</sup> and apical S<sup>2-</sup> group quantity, which is in good agreement with the calculated Tafel slope values (Table 4), as the Tafel slopes values of 38-57 mV dec<sup>-1</sup> are, reportedly, indicative of molybdenum sulfides containing bridging S<sub>2</sub><sup>2-</sup> and apical S<sup>2-</sup> groups [111, 177]. Note, that the apical S<sup>2-</sup> groups are claimed to be ineffective for HER [179, 186], inferring that the increase of HER activity is most likely related only to the increase of bridging S<sub>2</sub><sup>2-</sup> groups when the anodic pretreatment potential is increased.

### 3.4.3. Influence of annealing on the MoS<sub>2</sub>/Cysteine electrodes and their activation via anodic pretreatment

The influence of annealing on the HER activity, the S/Mo ratio and the relative content of bridging S<sub>2</sub><sup>2-</sup> and apical S<sup>2-</sup> groups were reported in [184, 185]. Similarly, after annealing anodically polarized at +0.85 V MoS<sub>2</sub>/Cysteine for 2 hours at 300 °C in vacuum, the S/Mo ratio was determined via XPS to decrease from 3.2 to 2.2. No significant changes in the Mo 3d spectra were observed, whereas the 2p<sub>3/2</sub> component at 163.2 eV, attributed to bridging S<sub>2</sub><sup>2-</sup> and apical S<sup>2-</sup> groups, peak area was determined to decrease from 59.1 % to 27.2 % after annealing (Fig. 3.25.).

A substantial decrease in HER activity of annealed MoS<sub>2</sub>/Cysteine was observed after annealing, as the current density at -0.35 V reached 11.9 mA cm<sup>-2</sup>, which is almost ten times lower than as-grown MoS<sub>2</sub>/Cysteine. Moreover, both the HER Tafel slope and exchange current density (Table 6)

markedly increased after annealing. The Tafel slope of  $131.1 \text{ mV dec}^{-1}$  suggests that the anodically pretreated and subsequently annealed MoS<sub>2</sub>/Cysteine possesses comparable HER activity to that of bulk 2H-MoS<sub>2</sub>, as suggested in [187], while the value of Tafel slope indicates that the Volmer step is the rate-determining step of HER after annealing.

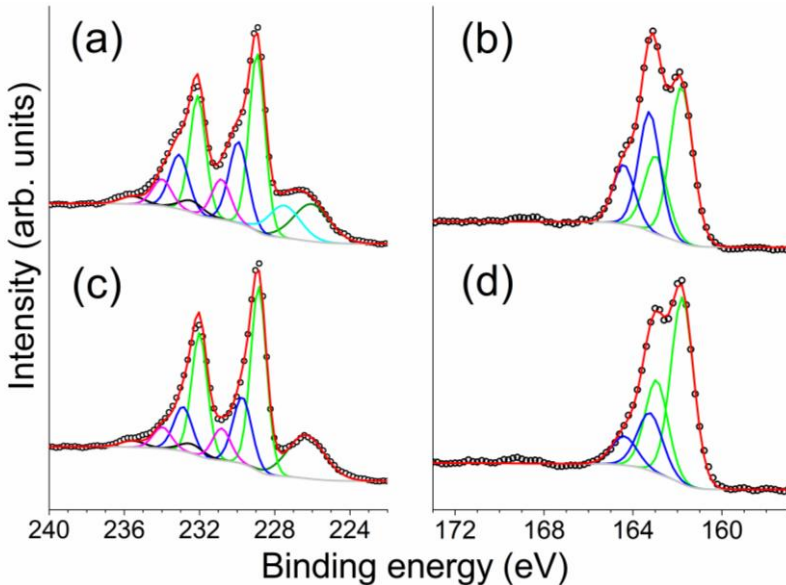


**Figure 3.25.** Mo 3d (a,c) and S 2p (b,d) X-ray photoelectron spectra of MoS<sub>2</sub>/Cysteine after anodic pretreatment for 15 s at  $+0.85 \text{ V}$  before (a,b) and after (c,d) annealing at  $300 \text{ }^\circ\text{C}$  in vacuum.

**3.25. pav.** Anodiškai apdoroto 15 s ties  $+0.85 \text{ V}$  MoS<sub>2</sub>/Cisteino elektrodo Mo 3d (a,c) ir S 2p (b,d) Rentgeno fotoelektronų spektrai prieš (a,b) ir po atkainitimo (c,d) vakuume ties  $300 \text{ }^\circ\text{C}$

After subsequent anodic cycling of pretreated and annealed MoS<sub>2</sub>/Cysteine (Fig. 3.26.), the HER activity increased once again with the current density reaching  $\sim 46 \text{ mA cm}^{-2}$  after CV scan from  $-0.05 \text{ V}$  to  $+1.15 \text{ V}$ , which albeit is still lower than as-grown MoS<sub>2</sub>/Cysteine, but almost four times higher than annealed MoS<sub>2</sub>/Cysteine. The Tafel slope and exchange current density values (Table 6) were found to decrease with an increase in  $E_{\text{switch}}$  up to  $+1.3 \text{ V}$ , while further increase of  $E_{\text{switch}}$  led to a decrease of only the exchange current density, while the Tafel slopes remained fairly constant. It is reported that the aforementioned changes should signify a decrease of MoS<sub>2</sub> quantity on the surface, rather than the decrease of 1T-MoS<sub>2</sub> relative content [126], or the decrease in length of the catalytically active edge sites [137].

**Table 6.** Calculated HER Tafel slopes exchange current density values of pretreated and annealed MoS<sub>2</sub>/Cysteine at different anodic polarization potentials.

**6 lentelė.** Apskaičiuotos anodiškai apdoroto ir atkaitinto MoS<sub>2</sub>/Cisteino elektrodo Tafel nuolinkio ir mainų srovės vertės papildomai apdorojant ties skirtiniais anodiniai potencialais.

$E_{\text{switch}}$ , V	$b$ , mV dec <sup>-1</sup>	$j_0$ , mA cm <sup>-2</sup>	$E_{\text{switch}}$ , V	$b$ , mV dec <sup>-1</sup>	$j_0$ , mA cm <sup>-2</sup>
Annealed	131.1	0.124	1.20	77.8	0.028
0.70	95.3	0.048	1.25	76.7	0.026
0.75	91.2	0.042	1.30	74.6	0.023
0.80	90.5	0.042	1.35	77.5	0.026
0.85	88.1	0.039	1.40	76.9	0.024
0.90	87.1	0.039	1.45	76.9	0.023
0.95	86.5	0.038	1.50	76.7	0.022
1.00	83.8	0.033	1.55	75.9	0.021
1.05	81.8	0.033	1.60	76.8	0.021
1.10	79.6	0.030	1.65	76.5	0.020
1.15	77.3	0.027	1.70	75.2	0.019

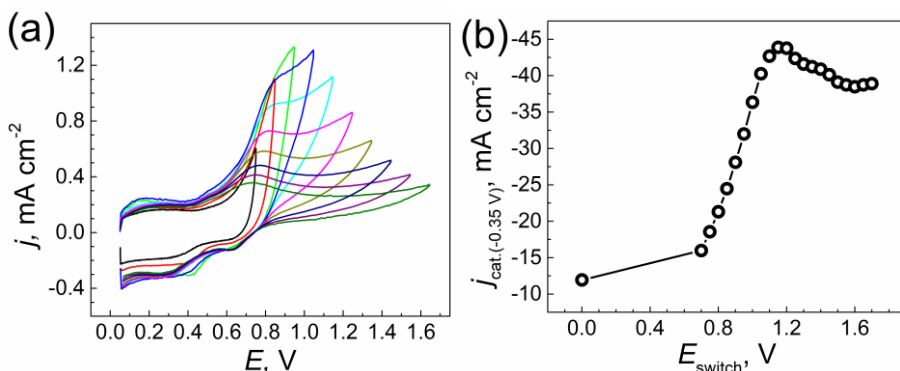


**Figure 3.26.** Cyclic voltammograms of anodic pretreatment to various  $E_{\text{switch}}$  potential values of MoS<sub>2</sub>/Cysteine (a) and the dependence of HER current densities at -0.35 V after anodic pretreatment on the  $E_{\text{switch}}$  (b). Prior to CV, the MoS<sub>2</sub>/Cysteine electrode was pretreated for 15 s at +0.85 V and annealed at 300 °C.

**3.26. pav.** MoS<sub>2</sub>/Cisteino anodinio apdorojimo ties skirtiniais posūkio potencialais ciklinės voltamperogramos (a) ir HER srovės tankio priklausomybė nuo posūkio potencijalo (b). Prieš CV, MoS<sub>2</sub>/Cisteino elektrodas apdorotas 15 s ties +0.85 V ir atkaitintas 300 °C temperatūroje.

#### 3.4.4. Investigation of HER stability of anodically pretreated MoS<sub>x</sub>/Cysteine electrodes

According to reports, the overpotential of HER for MoS<sub>x</sub> electrocatalysts increases when subjected to prolonged cathodic potentials [188, 189]. Consequently, the HER activity at a given potential decreases, along with the S/Mo ratio and the S 2p<sub>3/2</sub> XPS peak area ascribed to bridging S<sub>2</sub><sup>2-</sup> and apical S<sup>2-</sup> groups.

The HER stability of MoS<sub>2</sub>/Cysteine electrodes were investigated via chronopotentiometry (Fig. 3.27.), observing the changes in overpotential values at a fixed current density of 10 mA cm<sup>-2</sup> over 12 hour time period.

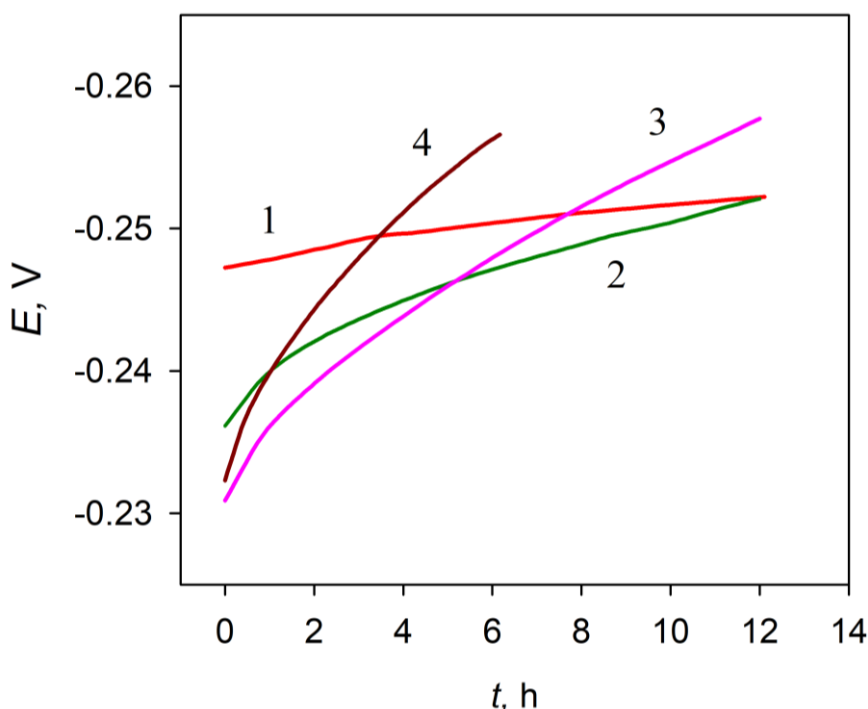


**Figure 3.27.** Chronopotentiometry curves at a constant -10 mA cm<sup>-2</sup> current density of as-grown MoS<sub>2</sub>/Cysteine (1), the same electrode after first anodic processing via CV from -0.25 V to +0.85 V at 10 mV s<sup>-1</sup> scan rate (2), and after second (3) and third (4) anodic processing along with 12 hours of HER processing cycles.

**3.27. pav.** Neapdoroto MoS<sub>2</sub>/Cisteino (1), to paties elektrodo po anodinio apdorojimo nuo -0.25 V iki +0.85 V (2), bei po antro (3), ir trečio (4) anodinio apdorojimo kartu su 12 val. katodinio polarizavimo chronopotenciometrinės kreivės, užrašytos uždavus pastovų -10 mA cm<sup>-2</sup> srovės tankį.

An initial overpotential of -0.248 V was determined for the as-grown MoS<sub>2</sub>/Cysteine electrode, with the change in overpotential ( $\Delta E$ ) over 12 hours of HER processing being negligible (Fig. 3.27. curve 1). When anodic polarization via CV from -0.25 V to +0.85 V potential range was applied to the same electrode (Fig. 3.27. curve 2), a substantial overpotential decrease was observed and determined to reach -0.236 V, while the overpotential after 12 hours of HER processing reaches the same -0.253 V value as was observed for as-grown MoS<sub>2</sub>/Cysteine after HER. Even though the initial overpotentials are lower than those observed for as-grown MoS<sub>2</sub>/Cysteine, second and subsequent anodic processing via CV from -0.25 V to +0.85 V along with 12 hours of HER processing at -10 mA cm<sup>-2</sup> of the same electrode (Fig. 3.27. curves 3,4) facilitates the increase of overpotential during 12 hour cathodic processing. It was determined that the prolonged successive anodic processing along with 12 hours of HER processing has a negative impact on the overall HER stability of the electrode, as after third cycle of such processing, the overpotential reaches the same value of -0.253 V almost three times faster compared to as-grown MoS<sub>2</sub>/Cysteine.

XRD was used to investigate the crystallinity of as-grown and anodically treated MoS<sub>2</sub>/Cysteine electrodes. From the obtained diffractograms (Fig. 3.28.), the as-grown MoS<sub>2</sub>/Cysteine (Fig. 3.28. 1) pattern is in good agreement with the PDF card of MoS<sub>2</sub>. The (002) peak is shifted from  $2\theta = 14.1$  deg to  $2\theta = 9.0$  deg due to the intercalation of guest species into the interlayers of MoS<sub>2</sub>. As described previously in section 1.1.2. the  $2\theta$  shift from ~14 deg to lower  $2\theta$  values might signify the formation of 1T-MoS<sub>2</sub>, albeit the peak shift is not conclusive evidence of the 1T-MoS<sub>2</sub> phase, as the expanded layers might still consist of 2H-MoS<sub>2</sub>. Changes in the XRD patterns were observed for the electrode after HER processing (Fig. 3.28. 2), where the diffraction peaks at  $2\theta = 9.0$  deg and  $2\theta = 18.6$  deg had disappeared, and a peak at  $2\theta = 13.2$  deg emerged, and the overall diffractogram resembles that of bulk 2H-MoS<sub>2</sub>. No discernible changes to the diffractogram were distinguished after quick anodic pretreatment cycles to +0.72 V (not shown). However, after anodic pretreatment via CV scan to +2.5 V (Fig. 3.28. 3) a broad peak at  $2\theta = 14.0$  deg is observed, whereas the (100) and (110) peaks at  $2\theta = 32.9$  deg and  $2\theta = 38.7$  deg, respectively, had disappeared, likely due to formation of amorphous MoS<sub>x</sub> with high S/Mo ratio, or a low MoS<sub>2</sub> quantity on the surface.

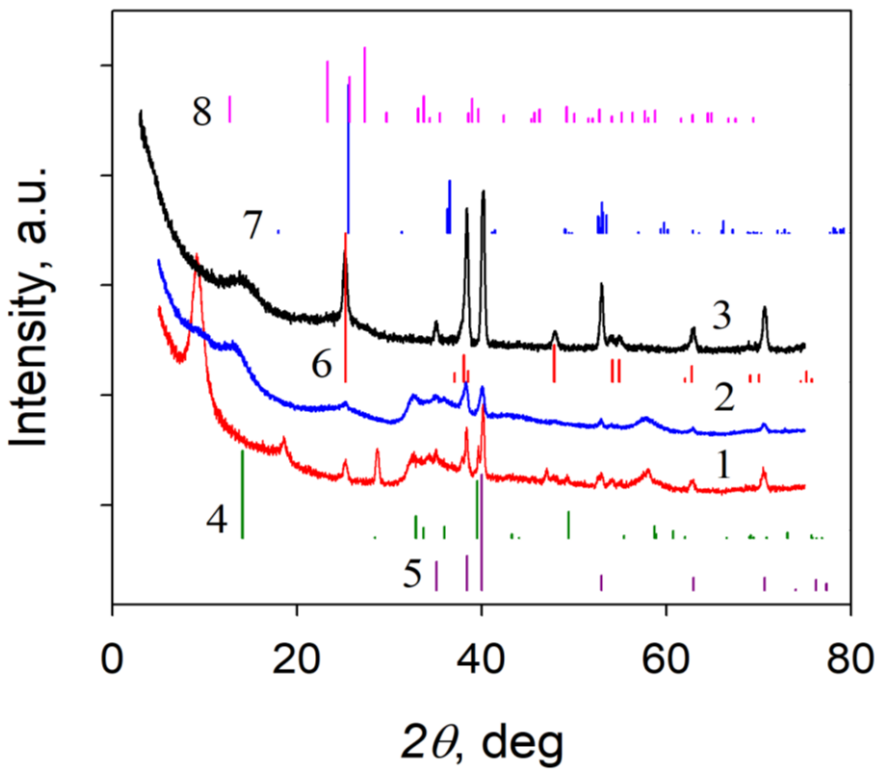


**Figure 3.28.** XRD patterns of MoS<sub>2</sub>/Cysteine before (1) and after HER processing via 1000 potential scan cycles (2), and after anodic pretreatment by potential sweep to +2.5 V at 0.5 mV s<sup>-1</sup> scan rate (3). Peak positions of PDF cards: (4) 01-075-1539 (MoS<sub>2</sub>), (5) 00-044-1294 (Ti), (6) 01-075-2544 (TiO<sub>2</sub>), (7) 04-013-3645 (MoO<sub>2</sub>), and (8) 00-005-0508 (MoO<sub>3</sub>).

**3.28. pav.** MoS<sub>2</sub>/Cisteino difraktogramos, užrašytos prieš (1) ir po HER apdorojimo praskleidžiant 1000 ciklų (2), ir po anodinio apdorojimo potencialą skleidžiant 0.5 mV s<sup>-1</sup> greičiu iki +2.5 V (3). PDF kortelių (4-8) smailių padėtys: (4) 01-075-1539 (MoS<sub>2</sub>), (5) 00-044-1294 (Ti), (6) 01-075-2544 (TiO<sub>2</sub>), (7) 04-013-3645 (MoO<sub>2</sub>), ir (8) 00-005-0508 (MoO<sub>3</sub>).

XPS was used to study the compositional changes of MoS<sub>2</sub>/Cysteine after HER processing. Aside from Mo<sup>6+</sup> component at 232.6 eV, other doublets in the Mo 3d spectra after HER processing (Fig. 3.29. c) appear at slightly lower binding energies compared to as-grown MoS<sub>2</sub>/Cysteine Mo 3d spectra (Fig. 3.29. a). Moreover, the most intense peak was observed at 228.5 eV. In the S 2p spectra (Fig. 3.29. d), only one doublet was observed after the HER processing, with the 2p<sub>3/2</sub> and 2p<sub>1/2</sub> components distinguished at 161.4 eV and 162.6 eV, respectively. The S/Mo ratio from the XPS of as-grown MoS<sub>2</sub> was 2.05, while after HER processing it was found to decrease to 1.85.

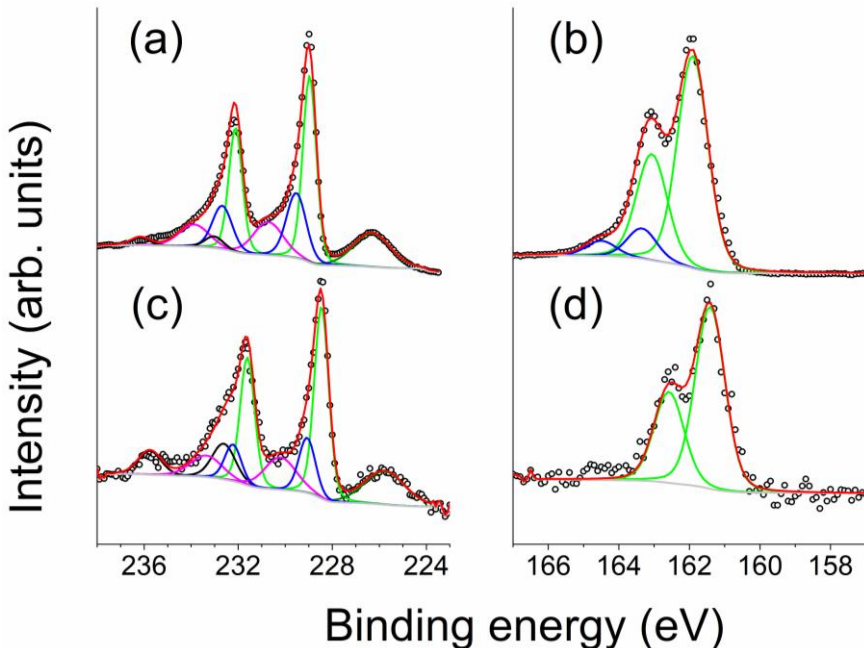
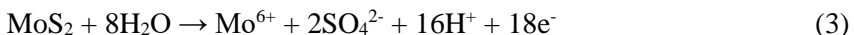


**Figure 3.29.** X-ray photoelectron spectra of as-grown MoS<sub>2</sub>/Cysteine (a,b) and the same electrode after HER processing for 12 h at 10 mA cm<sup>-2</sup> (c,d) Mo 3d (a,c) and S 2p (b,d) regions.

**3.29. pav.** MoS<sub>2</sub>/Cisteino prieš (a,b) ir po 12 val. HER ties 10 mA cm<sup>-2</sup> (c,d) Mo 3d (a,c) ir S 2p (b,d) Rentgeno fotoelektronų spektrai.

The XPS and XRD data infer that during hydrothermal synthesis of MoS<sub>2</sub>, a randomly oriented layered structure with peculiar Mo and S atom configuration is formed at the edges of nanoplatelets, similarly as reported by Joensen *et al.* in the case of Li exfoliated MoS<sub>2</sub> [190]. Moreover, the increase of HER activity after anodic pretreatment correlates with the increase of relative quantity of bridging S<sub>2</sub><sup>2-</sup> and apical S<sup>2-</sup> groups observed via XPS. During anodic treatment of MoS<sub>2</sub> two possible oxidation reactions could occur:



The former reaction (Eq. 3) suggests that the S<sup>2-</sup> oxidizes to form sulfate ions, leading to a decrease in the sulfur content on the surface of the electrode. The latter reaction (Eq. 4) indicates the formation bridging S<sub>2</sub><sup>2-</sup> groups, which are HER active and therefore could explain the increase of HER activity after anodic pretreatment. The decrease in HER activity after cathodic processing correlates with the decrease or a total loss (Fig. 3.29. d) in bridging S<sub>2</sub><sup>2-</sup> and apical S<sup>2-</sup> group XPS peak area. The structural changes observed in XRD (Fig.

3.28. patterns 1,2) and a resemblance to a possible change in Mo oxidation state (peaks of lower Mo oxidation states should appear at lower binding energies) observed in XPS (Fig. 3.29. a,c) implies that the catalytically active sites of  $\text{MoS}_2$  undergo chemical changes during HER. Despite this, the bridging  $\text{S}_2^{2-}$  and apical  $\text{S}^{2-}$  groups are not the sole HER active sites of  $\text{MoS}_2$  [191], hence the loss of the aforementioned groups does not make  $\text{MoS}_2$  incapable of electrocatalyzing the hydrogen evolution reaction [192].

### 3.5. Activity comparison of hydrothermally synthesized $\text{MoS}_2$ /amino acid electrodes

An activity comparison of different  $\text{MoS}_2$ /amino acid electrodes for hydrogen evolution reaction described in previous sections is depicted in Fig. 3.30.

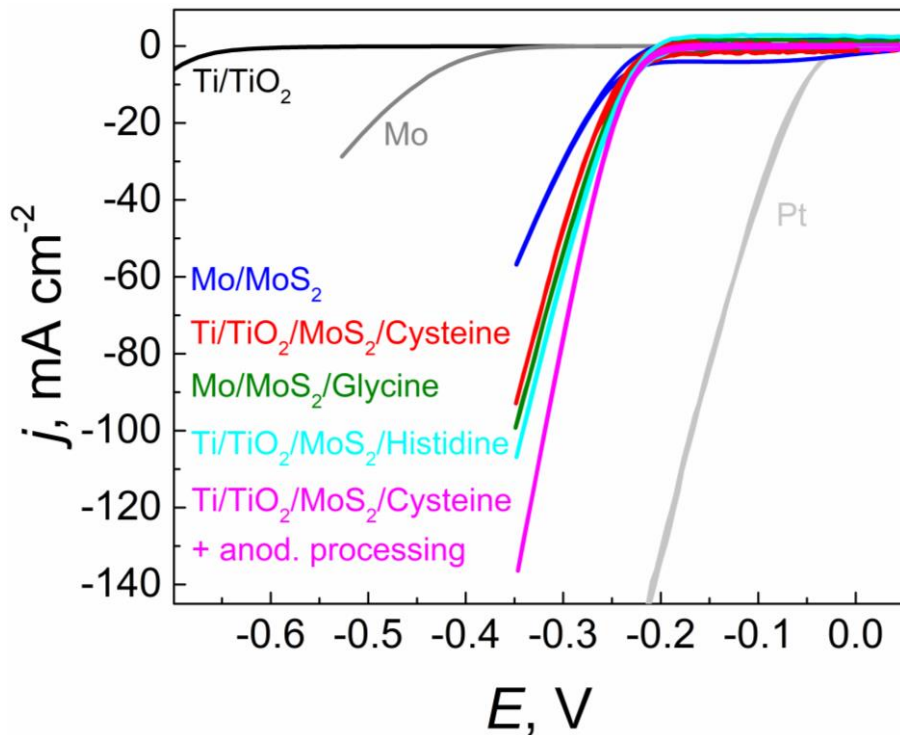


**Figure 3.30.** Cyclic voltammograms of different fabricated  $\text{MoS}_2$ /amino acid electrodes and their respective substrates. Voltammograms were recorded in 0.5 M  $\text{H}_2\text{SO}_4$  electrolyte at  $0.01 \text{ V s}^{-1}$  potential scan rate.

**3.30. pav.** Skirtingų  $\text{MoS}_2$ /aminorūgščių elektrodų bei pagrindų ciklinės voltamperogramos, užrašytos 0.5 M  $\text{H}_2\text{SO}_4$  elektrolite, potencialą skleidžiant  $0.01 \text{ V s}^{-1}$  greičiu.

## CONCLUSIONS

- Nanoplatelet molybdenum disulfide structures are formed during hydrothermal synthesis in the aqueous solutions of ammonium heptamolybdate and thiourea, with their surface morphology unaltered by the presence of amino acid additives, while the thickness is dependent on the duration of the synthesis.
- The formed MoS<sub>2</sub> films with amino acid additives exhibit larger interplanar distances, compared to MoS<sub>2</sub> films formed without amino acid additives. The interplanar distance of MoS<sub>2</sub> is increased due to charged guest species or fragment intercalation into the interlayers of MoS<sub>2</sub>.
- The addition of amino acids into the synthesis solution results in MoS<sub>2</sub> films with significantly higher quantity of metastable 1T-MoS<sub>2</sub> phase, compared to films without amino acid additives.
- Inserted amino acid fragments stabilize the metastable 1T, thus increasing the stability of fabricated electrodes
- Due to a relatively high content of 1T-MoS<sub>2</sub> phase, the fabricated MoS<sub>2</sub>/amino acid electrodes exhibit enhanced activity for hydrogen evolution reaction.
- Increase in the rate of hydrogen evolution reaction at MoS<sub>2</sub> films after anodic pretreatment is linked with the increase of bridging S<sub>2</sub><sup>2-</sup> and apical S<sup>2-</sup> sulfur group content due to anodic pretreatment.
- Anodic pretreatment could be employed as a method of increasing the activity of synthesized molybdenum disulfide electrodes for hydrogen evolution reaction. Up to 30% increase in electrocatalytic hydrogen evolution reaction activity could be obtained via application of a short anodic impulse.

## SANTRAUKA

### IVADAS

Dėl vis spartėjančios technologijų raidos bei populiacijos augimo, pasaulinis energijos poreikis nenumaldomai didėja. Tai verčia sunerimti, visų pirma dėl to, jog itin didelė energijos dalis šiuo metu yra gaunama naudojant iškastinį kurą [1]. Deginant iškastinį kurą į aplinką išmetami dideli kiekiai dujų ( $\text{CH}_4$ ,  $\text{CO}_2$ ,  $\text{N}_2\text{O}$ ), skatinančių šiltnamio efektą, dėl kurio stebimi Žemės klimato pokyčiai, kyla jūros lygis, bei daroma žala įvairioms ekosistemoms [2]. Todėl yra itin svarbu ieškoti bei vystyti tvarias alternatyvas iškastiniams kurui. Viena iš tokiu alternatyvų yra vandenilio kuras [3], kuris pasižymi aukštu gravimetriiniu energijos tankiu (~3 kartus didesnis, nei iškastinio kuro), bei tuo, jog degimo metu nesusidaro jokių aplinką teršiančių dujų [4, 5]. Tačiau, gamtoje tik <1% vandenilio randama  $\text{H}_2$  dujų pavidalu, o pagrindiniai vandenilio dujų gamybos metodai, tokie kaip garų riformingas, dalinė anglavandenilių oksidacija ar anglies dujofifikacija, naudoja iškastinį kurą ir išskiria nemažus kiekius šiltnamio dujų [6, 7]. Tvaresnis vandenilio gamybos metodas yra vandens elektrolizė, kurios metu vandens molekulės yra elektrochemiškai skaldomas į vandenilį ir deguonį [8]. Naudojant elektros energiją iš atsinaujinančių šaltinių, šis metodas galėtų būti laikomas aplinkai nekenksmingu vandenilio gamybos būdu [9], tačiau norint efektyviai išgauti vandenilį vandens elektrolizės metodu, būtina naudoti elektrokatalizatorius. Šiai dienai efektyviausiais laikomi brangūs ir gamtoje mažai paplitę tauriųjų metalų elektrokatalizatoriai, tokie kaip Pt,  $\text{RuO}_2$  ar  $\text{IrO}_2$  [10, 11], kas apsunkina pramoninį vandens elektrolizės pritaikymą vandenilio gamybai. Dėl šios priežasties naujų, prieinamų ir neturinčių tauriųjų metalų savo sudėtyje elektrokatalizatorių vystymas bei tobulinimas yra ypač aktuali tema ieškant tvareshnių energijos šaltinių.

Pastaruoju metu daug dėmesio skiriama potencialiaus HER elektrokatalizatoriais laikomiems pereinamujų metalų junginiams, tokiems kaip fosfidai [18], karbidai [19], nitridai [20], bei chalkogenidai [21]. Pereinamujų metalų dichalkogenidų nanomedžiagos, o ypač molibdeno disulfido  $\text{MoS}_2$ , yra aktualios galimam pritaikymui vandens skaldyme [22] tuo, jog pasižymi sluoksnine dvidimensine struktūra, bei nanometrinės skalės sluoksnio storai, kas lemia skirtinges šių nanomedžiagų chemines, fizikines ar elektronines savybes, lyginant su mikrometrinės eilės ir didesnėmis  $\text{MoS}_2$  medžiagomis [23, 24]. Be to,  $\text{MoS}_2$  nanomedžiagos pasižymi maža vandenilio adsorbcijos Gibbs'o laisvaja energija ( $\Delta G_{\text{H}^*}$ ), kuri yra tik vos didesnė nei Pt metalo [25]. Tačiau, siekiant jog  $\text{MoS}_2$  nanomedžiagos taptų pritaikomos

vandenilio gamybai pramoniniu mastu, reikia įveikti keletą iššūkių, tokius kaip nanomedžiagų sintezės optimizavimas bei kontroliavimas, HER efektyvumo bei elektrokatalizatoriaus stabilumo padidinimas bei MoS<sub>2</sub> nanomedžiagų integravimas į praktiškas vandens elektrolizės sistemas.

## DARBO TIKSLAS

Ištirti aminorūgščių įtaką vandenilio išskyrimo reakcijai skirtų hidrotermiškai susintetinė nanolapelinės struktūros MoS<sub>2</sub> elektrodų aktyvumui ir stabilumui bei nustatyti efektyviausią MoS<sub>2</sub> aktyvių pozicijų prigimtį.

## DARBO UŽDAVINIAI

- Susintetinti MoS<sub>2</sub> dangas su glicino, L-cisteino ir DL-histidino aminorūgštimis ir ištirti aminorūgščių įtaką suformuotų dangų aktyvumui bei stabilumui.
- Charakterizuoti MoS<sub>2</sub>/aminorūgščių dangas ir ištirti galimą priemaišų įsiterpimą į MoS<sub>2</sub> tarpsluoksnius.
- Ištirti anodinio apdorojimo įtaką hidrotermiškai susintetintiems MoS<sub>2</sub> elektrodams.
- Nustatyti aktyvių HER pozicijų prigimtį MoS<sub>2</sub> dangose ir įvertinti jų santykinio kieko padidėjimą po anodinio apdorojimo.

## MOKSLINIS NAUJUMAS

- Pirmą kartą nustatyta aminorūgščių įtaka hidroterminei molibdeno disulfido sintezei. Parodyta, jog į amonio heptamolibdato ir tiourėjos tirpalą pridėjus kai kurių aminorūgščių, hidroterminės sintezės metu susiformavusi nanolapelinės struktūros MoS<sub>2</sub> danga pasižymi santykinai dideliu metastabilios, metališkosiomis savybėmis pasižyminti 1T-MoS<sub>2</sub> fazės kiekiu.
- Pirmą kartą parodyta, jog hidrotermiškai susintetintos MoS<sub>2</sub> dangos su aminorūgštimis pasižymi didesniu vandenilio išskyrimo reakcijos greičiu bei stabilumu, lyginant su MoS<sub>2</sub> dangomis, susintetintomis be aminorūgščių.
- Atliktas bei ištirtas naujas molibdeno disulfido elektrodo aktyvumo padidinimo būdas anodiškai apdorojant susintetintas MoS<sub>2</sub> dangas.

Parodyta, jog anodinio apdorojimo metu padidėja santykinis katalitiškai aktyvių tiltelinii  $S_2^{2-}$  grupių kiekis.

## GINAMIEJI TEIGINIAI

- Hidrotermiškai susintetintos  $MoS_2$  dangos su aminorūgščių priedais pasižymi didesniu vandenilio išskyrimo reakcijos greičiu bei stabilumu, lyginant su hidrotermiškai susintetintomis  $MoS_2$  dangomis be aminorūgščių.
- Suformuotų  $MoS_2$ /aminorūgščių elektrodų aktyvumo bei stabilumo padidėjimas siejamas su metastabilios 1T- $MoS_2$  fazės susiformavimu dėl krūvį turinčių aminorūgščių skilimo fragmentų įsiterpimo į  $MoS_2$  tarpsluoksnius.
- Anodinis apdorojimas papildomai padidina  $MoS_2$ /aminorūgščių elektrodų aktyvumą dėl anodinio proceso metu padidėjusio santykinio tiltelinii  $S_2^{2-}$  grupių, kurios laikomos aktyvesnėmis vandenilio išskyrimo pozicijomis, kiekiu.

## AUTORIAUS INDĒLIS

Padėklų paruošimas, titano anodavimas,  $MoS_2$  bei nanodalelių hidroterminė sintezė atlikta disertacijos autoriaus. Autorius paruošė visus pavyzdžius šioje disertacijoje aprašytiems eksperimentams. Taip pat, autorius atliko suformuotų  $MoS_2$  elektrodų vandenilio išskyrimo reakcijos tyrimus ciklinės voltamperometrijos bei chronopotenciometrijos metodais, atliko anodinį apdorojimą ir anodiškai apdorotų elektrodų elektrocheminius matavimus. Be to, autorius atliko XPS spektrų analizę bei prisdėjo nagrinėjant kitus gautus rezultatus, kurių grafikus bei paveikslus ir prisdėjo prie moksliinių publikacijų rengimo. Autorius pats parašė šią disertaciją, o visa iš kitų šaltinių gauta informacija atitinkamai cituojama.

#### 4. EKSPERIMENTO METODIKA

MoS<sub>2</sub> dangos buvo nusodintos ant 7 x 7 mm dydžio Ti arba Mo padéklų. Prieš sintezę padéklai nuvalomi 1:1 acetono ir 2-propanolio mišiniu, plaunant padéklus ultragarsinėje vonelėje 30 min, bei po to plaunant 10 min dejonizuotu vandeniu tris kartus. Ti/TiO<sub>2</sub> padéklai pagaminti anoduojant Ti padéklus 2 M H<sub>3</sub>PO<sub>4</sub> ir 0.2 M NH<sub>4</sub>F tirpale. Ti padéklas, naudojamas kaip anodas, buvo patalpinamas į plastikinę celę, tuo tarpu dvi lygiagrečios platinos plokštelių buvo naudojamos kaip katodas. Anodavimas vykdytas 60 min uždavus 20 V įtampą bei palaikant pastovų elektrolito maišymą. Po anodavimo elektrodai kruopščiai praplauti dejonizuotu vandeniu, išdžiovinti ir tuomet atkaitinti 2 valandas 420 °C temperatūroje.

Molibdeno disulfido dangos suformuotos hidroterminės sintezės būdu naudojant amonio heptamolibdato ir tiourėjos tirpalą. 5 mM amonio heptamolibdato ir 90 mM tiourėjos tirpalas buvo supilamas į PTFE cele, papildomai pridedant įvairių amino rūgščių (L-cisteino, DL-histidino, glicino). Pagrindas, ant kurio buvo formuojamos MoS<sub>2</sub> dangos buvo įtaisomas tam skirtame PTFE celės tvirtinimo taške taip, jog būtų pilnai pamerktas į tirpalą ir būtų vertikaliuoje padėtyje visos sintezės metu. Sintezė atlakta patalpinus PTFE celę į autoklavą, kaitinant ties 220 °C temperatūra nuo 5 iki 15 valandų. Po sintezės gauti elektrodai praplauti dejonizuotu vandeniu ir išdžiovinti kambario temperatūroje naudojant N<sub>2</sub> dujas. MoS<sub>2</sub> nanodalelės buvo sintetinamos analogiška tvarka. Siekiant išvengti paviršių oksidacijos ar MoS<sub>2</sub> fazės pokyčių, gautų MoS<sub>2</sub> dangų bei dalelių tyrimai atliki nedelsiant, o nesant tokiai galimybei, susintetinti pavyzdžiai buvo patalpinti į sandarius mėgintuvėlius, užpildytus Ar arba N<sub>2</sub> dujomis.

Molibdeno disulfido elektrodų elektrocheminiai matavimai atliki naudojant Zahner Zennium potencijostatą (Zahner-Elektrik, Vokietija). Matavimai atliki trijų elektrodų celėje, kurioje darbinis elektrodas – susintetintas MoS<sub>2</sub> elektrodas, Ag/AgCl, KCl<sub>sat</sub> su Luggin'o kapiliaru – palyginamasis elektrodas ir grafito strypelis – pagalbinis elektrodas. Visuose aprašytuose elektrocheminiuose matavimuose elektrolitu naudotas 0,5 M H<sub>2</sub>SO<sub>4</sub> tirpalas. Visi potencialai, nurodyti šioje disertacijoje, yra pateikti pagal SHE skalę. Morfologijos tyrimai atliki naudojant Helios Nanolab 650 (FEI, Olandija) skenuojanči elektronų mikroskopą su Rentgeno spektrometru (Oxford Instruments, Jungtinė Karalystė). Nuotraukos, gautos naudojant Tecnai F20 peršvietimo elektronų mikroskopą (FEI, Olandija) panaudotos įvertinant MoS<sub>2</sub> tarpplokštuminius atstumus. Struktūrinė analizė atlakta naudojant SmartLab (Rigaku, Japonija) Rentgeno difraktometrą. Raman spektrai gauti naudojant Renishaw inVia (Renishaw, Jungtinė Karalystė)

spektrometru. Siekiant išvengti pavyzdžio oksidacijos, lazerio galia apribota iki 0.06 mW. MoS<sub>2</sub> dangų elementų cheminė būseną analizuota VERSAPROBE PHI 5000 (Physical Electronics, Jungtinės Amerikos Valstijos), Rentgeno fotoelektronų spektrometru. Gautų XPS duomenų analizė atlikta naudojantis CASA XPS (Casa Software, Jungtinė Karalystė) programine iranga. Terminis L-cisteino skilimas tirtas STA PT 1600 (Linseis, Vokietija) termogravimetriiniu analizatoriumi kartu su MS Thermostar GDS 320 (Linseis/Pfeiffer, Vokietija) masių spektrometru. FTIR spektrai gauti naudojant ALPHA FTIR (Bruker, Vokietija) spektrometrą.

## 5. TYRIMO REZULTATAI

### 5.1. MoS<sub>2</sub>/Glicino dangų sintezė ir charakterizavimas

#### 5.1.1. MoS<sub>2</sub>/Glicino dangų morfologija

Molibdeno disulfidas buvo susintetintas hidroterminės sintezės metodu naudojant 5 mmol L<sup>-1</sup> amonio heptamolibdato, 90 mmol L<sup>-1</sup> tiourėjos ir glicino tirpalus, kuriuose glicino koncentracija tirta nuo 0 iki 150 mmol L<sup>-1</sup>. Sintezės atliktos ties 220 °C temperatūra sintezę vykdant nuo 5 iki 15 valandų. Mo arba Ti metalų folijos naudotos kaip pagrindai, ant kurių buvo susintetinamos tolygios, juodos spalvos MoS<sub>2</sub> dangos.

Skenuojančiu elektronų mikroskopu (SEM) gautos hidrotermiškai susintetintų MoS<sub>2</sub> dangų nuotraukos pateiktos 3.1. paveiksle (žr. 40 p.). Iš jų matoma, jog glicino įdėjimas į sintezės tirpalą nedaro įtakos MoS<sub>2</sub> dangų morfologijai – tiek sintezės be glicino, tiek su 100 mmol L<sup>-1</sup> glicino metu susidaro tokios pat nanolapelinės struktūros. Aptyksliai nustatytas vieno nanolapelio dydis yra  $200 \pm 50$  nm, o storis  $5 \pm 2$  nm, kas leidžia manyti, jog vienas nanolapelis yra sudarytas iš 5-12 S-Mo-S nanosluoksniių. Pastebėta, jog dangos su glicinu yra mažiau sutrūkinėjusios, lyginant su dangomis, gautomis tokiomis pačiomis sąlygomis be glicino. Aiškių skirtumų tarp dangų morfologijos naudojant skirtinges glicino koncentracijas neaptikta (3.2. pav.; žr. 41 p.). Nustatyta, jog dangos storis bei tolygumas priklauso nuo sintezės laiko, kai sintezė atlakta 5 val. 220 °C temperatūroje, dangos storis siekia 0.8 – 0.9 μm, tuo tarpu prailginus sintezę iki 15 val. gaunamos ~2 μm storio dangos.

Gautose HRTEM nuotraukose (5.2.c pav) matomi MoS<sub>2</sub> dangos defektai bei gardelės iškraipymai, taip pat pastebima, jog tarpplokštuminiai atstumai yra išsidėstę netolygiai ir yra nukrypę nuo 0.615 nm vertės, būdingos grynai 2H-MoS<sub>2</sub> fazei. Iš MoS<sub>2</sub>/Glicino dangų HRTEM nuotraukų įvertintas tarpplokštuminis atstumas tam tikrose vietose siekia 0.89 nm, kas leidžia manyti, jog atliekant hidroterminę MoS<sub>2</sub> sintezę su glicinu, MoS<sub>2</sub> tarpsluoksniai yra išplečiami dėl galimos sąveikos su sintezės tirpale esančiais komponentais [152].

#### 5.1.2. MoS<sub>2</sub>/Glicino dangų charakterizavimas

Susintetinto molibdeno disulfido kristališkumo bei fazės tyrimai atlikti Rentgeno spindulių difrakcijos (XRD) metodu. Gauta hidrotermiškai susintetinto gryno MoS<sub>2</sub> (nenaudojant glicino) difraktograma (3.3. pav. a1; žr.

42 p.) atitinka standartinę molibdenito 2H-MoS<sub>2</sub> difraktogramą (PDF kortelė 00-037-1492). Smailės, esančios ties 14.37°, 33.51°, ir 35.87° 2θ vertėmis atitinkamai priskirtos (002), (101) ir (102) heksagoninės gardelės, kurios parametrai  $a = b = 3.161 \text{ \AA}$ ,  $c = 12.298 \text{ \AA}$ , plokštumoms, kas prilygsta teorinėms 2H-MoS<sub>2</sub> fazės vertėms. Kita vertus, susintetinto MoS<sub>2</sub> su glicinu difraktogramoje (3.3. pav. a2-a4; žr. 42 p.) pastebimi skirtumai nuo grynam 2H-MoS<sub>2</sub> būdingos difraktogramos. Esminis skirtumas yra tai, jog (002) plokštumos difrakcijos smailė ties  $2\theta = 14.37^\circ$  pasislenka į  $2\theta = 9.4^\circ$ . Toks (002) plokštumai priskiriamos smailės poslinkis link mažesnių  $2\theta$  verčių, pasak literatūros šaltinių, rodo MoS<sub>2</sub> tarpsluoksnį išsiplėtimą dėl pašalinių dalelių įsiterpimo [67]. Šis pastebėtas poslinkis atitinka anksčiau aprašytą HRTEM, o tai rodo, kad atliekant hidroterminę sintezę su glicino priedu, gaunamos MoS<sub>2</sub> dangos pasižymi išplėstu tarpsluoksniu atstumu.

Siekiant nustatyti susintetinto molibdeno disulfido fazę buvo atliki Ramano spektroskopijos matavimai, gauti Raman spektrai pateikti 3.3. b paveiksle. Gryno MoS<sub>2</sub> spektre (3.3. pav. b1; žr. 42 p.) matomos dvi aiškiai išreikštos Raman modos: E<sup>1</sup><sub>2g</sub> (383 cm<sup>-1</sup>) ir A<sub>1g</sub> (409 cm<sup>-1</sup>). Šios S atomų plokštuminei vibracijai (E<sup>1</sup><sub>2g</sub>) bei neplokštuminiam S atomų tempimui (A<sub>1g</sub>) priskiriamos modos yra charakteringos kristaliniam 2H-MoS<sub>2</sub> [153]. Tuo tarpu pridėjus glicino į hidroterminę sintezę tirpalą, gautos Raman smailės (3.3. pav. b2-b4; žr. 42 p.) yra mažiau išreikštos, kas gali reikšti, jog tokiu būdu susintetintos mažiau kristališkos MoS<sub>2</sub> dangos. A<sub>1g</sub> moda pasislenka nuo 409 cm<sup>-1</sup> iki 413 cm<sup>-1</sup>, o E<sup>1</sup><sub>2g</sub> moda išnyksta ir pastebimos naujos modos ties 316 cm<sup>-1</sup>, 936 cm<sup>-1</sup> ir 1534 cm<sup>-1</sup>. Pasak literatūros šaltinių, A<sub>1g</sub> modos poslinkis bei E<sup>1</sup><sub>2g</sub> modos intensyvumo sumažėjimas arba jos dingimas gali būti susiejamas su 1T-MoS<sub>2</sub> faze arba 1T/2H-MoS<sub>2</sub> fazų mišiniu [79, 81]. Dangų su skirtina glicino koncentracija Raman spektrai mažai skiriasi, stebimas tik neryškus smailės ties 1534 cm<sup>-1</sup>, kuri gali būti priskiriama glicinui, intensyvumo padidėjimas, kuomet glicino koncentracija padidinama nuo 40 mmol L<sup>-1</sup> iki 100 mmol L<sup>-1</sup>. Mažo intensyvumo smailė ties 936 cm<sup>-1</sup> gali būti priskiriama nesureagavusio amonio heptamolibdato likučiui iš sintezės tirpalui [154].

Papildomi MoS<sub>2</sub> dangų fazės tyrimai atliki naudojant Rentgeno fotoelektronų spektroskopiją (XPS). Spektre (3.4. pav. a; žr. 44 p.), užrašytame 240 eV – 222 eV ryšio energijos ruože, pavaizduotos išmuštų iš Mo 3d bei S 2s lygmenų fotoelektronų smailės.

Mo 3d spektras buvo išskaidytas į tris dubletus, iš kurių pirmieji du priskirti Mo<sup>4+</sup> iš 2H-MoS<sub>2</sub> su dubletiniais komponentais ties 229.4 eV (3d<sub>5/2</sub>) ir 232.5 eV (3d<sub>3/2</sub>), ir Mo<sup>4+</sup> iš 1T-MoS<sub>2</sub> ties 228.3 eV (3d<sub>5/2</sub>) ir 231.5 eV (3d<sub>3/2</sub>). Trečiasis dubletas priskirtas Mo<sup>6+</sup> iš MoO<sub>3</sub> ties 232.2 eV (3d<sub>5/2</sub>) ir 235.3 eV

( $3d_{3/2}$ ). Santykinis šiu komponentų indėlis visam Mo 3d spektrui apskaičiuotas atitinkamai 36%, 49% ir 15%. S 2p spektre (3.4. pav. b, žr. 44 p.), užrašytame 157 eV – 173 eV ruože, nustatyti du pagrindiniai dubletai. Jie priskirti  $S^{2-}$  iš 1T-MoS<sub>2</sub> ties 161.1 eV ( $2p_{3/2}$ ) ir 162.2 eV ( $2p_{1/2}$ ), bei iš 2H-MoS<sub>2</sub> ties 162.1 eV ( $2p_{3/2}$ ) ir 163.2 eV ( $2p_{1/2}$ ). Neryškus dubletas ties ~168 eV priskirtinas SO<sub>x</sub> dėl galimos nežymios paviršiaus oksidacijos. Kitų smailių nebuvinamas S 2p spektre leidžia manyti, jog sieros atomai daugiausia dalyvauja S-Mo ryšiuose. N 1s spektras (390 – 410 eV) persidengia su Mo 3p spektru (385 – 420 eV), todėl gautas spektras (3.4. pav. c, žr. 44 p.) išskaidytas į keturis komponentus, kurių pirmi trys priskirti Mo  $3p_{3/2}$  komponentams iš 1T-MoS<sub>2</sub> (394.2 eV), 2H-MoS<sub>2</sub> (395.1 eV), ir MoO<sub>3</sub> (397.8 eV). Ketvirtasis komponentas ties 401.2 eV priskirtinas glicinui, kadangi NH<sub>3</sub><sup>+</sup> smailė stebima ties 402.4 eV, o neutralios amino grupės NH<sub>2</sub> smailė stebima ties 400.5 eV [155]. Tzvetkov ir Netzer teigimu, šios smailės atsiradimas gali būti susijęs su adsorbuotais dalinai suskilusio glicino molekuliniams fragmentams.

#### 5.1.3. MoS<sub>2</sub>/Glicino elektrodų HER savybių tyrimas

Susintetintų MoS<sub>2</sub>/Glicino elektrodų katalizinis aktyvumas bei stabilumas ištirti ciklinės voltamperometrijos būdu 0.5 M H<sub>2</sub>SO<sub>4</sub> elektrolite; gautos voltamperogramos pavaizduotos 3.5. paveiksle. Nustatyta, jog glicino pridėjimas daro įtaką suformuoto elektrodo aktyvumui bei stabilumui. Gryno MoS<sub>2</sub> atveju (3.5. pav. a; žr. 45 p.) pradinis srovės tankis ties -0.35 V siekė 56.8 mA cm<sup>-2</sup>, tačiau po 50 skleidimo ciklų stebimas ryškus srovės tankio sumažėjimas, o po 250 ciklų srovės tankis ties -0.35 V sumažėja beveik triskart iki 17.1 mA cm<sup>-2</sup>. Tuo tarpu MoS<sub>2</sub>/Glicino elektrodai pasižymėjo ženkliai geresniu stabilumu. Kuomet dangos buvo susintetintos su 40 mmol L<sup>-1</sup> glicino (3.5. pav. b; žr. 45 p.), pradinis srovės tankis registratorius panašus į gryno MoS<sub>2</sub>, tačiau po 250 ciklų srovės tankio ties -0.35 V sumažėjimas nesiekė 10%. Padidinus glicino koncentraciją iki 70 mmol L<sup>-1</sup> (3.5. pav. c; žr. 45 p.) buvo pastebėtas didesnis pradinis srovės tankis (62.5 mA cm<sup>-2</sup>), o praskleidus 500 ciklų srovės tankio sumažėjimas neužfiksotas. Dangos su 100 mmol L<sup>-1</sup> glicino (3.5. pav. d; žr. 45 p.) atveju pradinis srovės tankis buvo 82 mA cm<sup>-2</sup>, toliau skleidžiant išaugo iki ~100 mA cm<sup>-2</sup>, bei išliko pastovus praskleidus 2000 ciklų.

Apskaičiuoti Tafel nuolinkiai elektrodiui su 100 mM glicino po 1000 ciklų buvo 54.6 mV dec<sup>-1</sup>. Ivertintas reakcijos pradžios potencialas lygus ~0.2 V ir nepriklauso nuo glicino koncentracijos, tuo tarpu gryno MoS<sub>2</sub> atveju, po 250 ciklų reakcijos pradžios potencialas padidėjo iki ~0.24 V. Papildomai

buvo atlikti tyrimai, kuomet  $\text{MoS}_2$  dangos susintetintos su  $150 \text{ mmol L}^{-1}$  glicino. Šių dangų stabilumas panašus kaip ir  $100 \text{ mmol L}^{-1}$  glicino atveju, tačiau šios dangos pasižymėjo mažesniu HER greičiu.

Pagamintų elektrodų su glicinu stabilumas papildomai patvirtintas įvertinus elektrodų masės pokyčius po HER apdorojimo. Gryno  $\text{MoS}_2$  elektrodo atveju, elektrodo masė po 500 ciklų sumažėjo apie 60%, tuo tarpu elektrodo, susintetinto su  $100 \text{ mmol L}^{-1}$  glicino masės pokytis buvo ~0.1% po 2000 ciklų. Glynas  $\text{MoS}_2$  elektrodas ciklinės voltamperometrijos metu prarado savo juodą spalvą ir buvo pilkos, metališkos spalvos, o elektrolite buvo matomos nedidelės juodos spalvos dalelės.  $\text{MoS}_2/\text{Glicino}$  elektrodo SEM nuotraukose prieš ir po vandenilio išskyrimo reakcijos struktūrinių pokyčių nepastebėta.

## 5.2. $\text{MoS}_2$ dangos su L-cisteinu

### 5.2.1. $\text{MoS}_2/\text{Cisteino}$ dangų morfologija

Molibdeno disulfido elektrodai su L-cisteino amino rūgštimi buvo susintetinti hidroterminės sintezės būdu iš amonio heptamolibdato, tiourėjos ir L-cisteino tirpalo, kur L-cisteino koncentracija neviršijo  $3 \text{ mmol L}^{-1}$ , o pasirinktas sintezės laikas – 5 valandos. Gautų dangų morfologiją pateikta 3.7. paveiksle (žr. 48 p.).

Pateiktose SEM nuotraukose matoma, jog L-cisteino įdejimas į sintezės tirpalą neturi įtakos  $\text{MoS}_2$  dangos struktūrai. Pagrindu buvo pasirinktas anoduotas titanas, dėl geresnio  $\text{MoS}_2$  dangų sankabumo su anodavimo metu susiformavusiais  $\text{TiO}_2$  nanovamzdėliais (3.7. pav. b intarpas; žr. 48 p.). Buvo nustatyta, jog dangos storis priklauso nuo sintezės laiko, tačiau dangos su L-cisteinu buvo nežymiai storesnės, lyginant su gryno  $\text{MoS}_2$  dangomis. HRTEM nuotraukoje matomas  $\text{MoS}_2$  sluoksnių iškraipymas, nustatytas tarpplokštuminis atstumas tarp gretimų S-Mo-S sluoksnių buvo  $8.4 \text{ \AA}$ , o tai yra žymiai didesnis atstumas, nei kristaliniam  $2\text{H}-\text{MoS}_2$  būdingas  $6.15 \text{ \AA}$  atstumas. Be to, HRTEM nuotraukose galima ižvelgti netvarkingą atomų išsidėstymą, įvairius posūkius ir skirtingus tarpplokštuminius atstumus. Kai kuriose vietose atstumas tarp sluoksnių viršijo  $10 \text{ \AA}$ , kas galėtų būti galimo pašalinių dalelių įsiterpimo indikacija.

### 5.2.2. Susintetintos MoS<sub>2</sub>/Cisteino dangos charakterizavimas

Galimas MoS<sub>2</sub> fazės pokytis dėl priemaišų įsiterpimo į pagamintų dangų tarp sluoksnius tirtas Raman spektroskopijos būdu. MoS<sub>2</sub> dangų po sintezės bei po elektrocheminių matavimų užregistruoti Raman spektrai pateikti 3.8. paveiksle (žr. 49 p.).

Grynos MoS<sub>2</sub> dangos Raman spektre (3.8. pav. a; žr. 49 p.), matomos dvi aiškiai išreikštos smailės ties 409.1 cm<sup>-1</sup> bei 379.0 cm<sup>-1</sup>, kurios atitinkamai priskirtos A<sub>1g</sub> bei E<sup>1</sup><sub>2g</sub> modoms. Šios modos būdingos kristaliniam 2H-MoS<sub>2</sub> ir yra stebimos nepriklausomai nuo sužadinimo spinduliuotės bangos ilgio, dėl to yra laikomos charakteringomis puslaidininkinei 2H fazei [77]. MoS<sub>2</sub>/Cisteino spektruose (3.8. pav. b,c; žr. 49 p.) matomi pokyčiai nuo gryno MoS<sub>2</sub> Raman spektro. Buvo nustatyta, jog A<sub>1g</sub> modai priskirtina smailė pasislenka nuo 409.1 cm<sup>-1</sup> iki 405.4 cm<sup>-1</sup>, o E<sup>1</sup><sub>2g</sub> išnyksta. Taip pat, stebimos naujos smailės ties 143.9 cm<sup>-1</sup> bei 293.7 cm<sup>-1</sup>, kurios gali būti priskiriamos J<sub>1</sub> ir E<sub>1g</sub> modoms iš 1T-MoS<sub>2</sub>. Išplatėjusi smailė 1100-1700 cm<sup>-1</sup> ruože gali būti stebima dėl cisteino molekulių ar jų fragmentų virpesių. Po ciklinės voltamperometrijos užrašyti Raman spektrai (3.8. pav. c; žr. 49 p.) nežymiai skiriasi nuo ką tik susintetinto MoS<sub>2</sub>/Cisteino spektro. Pagrindinis skirtumas yra padidėjęs A<sub>1g</sub> modai priskiriamos smailės intensyvumas, bei E<sup>1</sup><sub>2g</sub> modai priskiriamos smailės atsiradimas, nepaisant pastarosios smailės itin mažo intensyvumo. Šie rezultatai koreliuoja su literatūroje pateiktais 1T/2H-MoS<sub>2</sub> Raman spektrais, o tokie A<sub>1g</sub> bei E<sup>1</sup><sub>2g</sub> modų pokyčiai parodo, jog MoS<sub>2</sub>/Cisteino sintezės metu formuoja 1T arba 1T/2H fazų mišinys [80, 81].

MoS<sub>2</sub>/Cisteino dangų paviršiaus elementų cheminė būsena įvertinta Rentgeno fotoelektronų spektroskopijos metodu. Užrašius tiriamajį spektrą, dangose buvo nustatyti Mo, S, O, N ir C elementai. Mo 3d spektras (3.10. pav. a; žr. 51 p.) buvo išskaidytas į penkis dubletus. Pirmieji du dubletai priskirti Mo<sup>4+</sup> iš 1T-MoS<sub>2</sub> ir 2H-MoS<sub>2</sub>, kurių 3d<sub>5/2</sub> bei 3d<sub>3/2</sub> komponentų ryšio energijos atitinkamai nustatytos: 228.5 eV ir 231.7 eV (1T), bei 229.0 eV ir 232.2 eV (2H). Sekantis dubetas priskirtas Mo<sup>4+</sup> iš MoO<sub>2</sub> su 230.4 eV (3d<sub>5/2</sub>) bei 233.6 eV (3d<sub>3/2</sub>) smailių ryšio energijomis. Mažo intensyvumo dubetas ties 229.7 eV (3d<sub>5/2</sub>) greičiausiai matomas dėl Mo-N ryšių. Paskutinis matomas dubetas ties 232.5 eV (3d<sub>5/2</sub>) ir 235.6 eV (3d<sub>3/2</sub>) buvo priskirtas Mo<sup>6+</sup> iš MoO<sub>3</sub>.

Išskaidytame S 2p spektre (3.10. pav. b; žr. 51 p.) matomi trys dubletai, sudaryti iš 2p<sub>3/2</sub> bei 2p<sub>1/2</sub> komponentų. Pirmi du dubletai priskirti S<sup>2-</sup> iš MoS<sub>2</sub>, kur 161.5 eV (2p<sub>3/2</sub>) bei 162.6 eV (2p<sub>1/2</sub>) priskirtas 1T-MoS<sub>2</sub>, o dubetas su 163.0 eV (2p<sub>3/2</sub>) bei 164.1 eV (2p<sub>1/2</sub>) ryšio energijomis priskirtas 2H-MoS<sub>2</sub>. Trečiasis dubetas su 168.4 eV (2p<sub>3/2</sub>) bei 169.6 eV (2p<sub>1/2</sub>) komponentais

priskirtas  $\text{SO}_x$ . Kaip ir Mo 3d spektre, intensyviausia smailė S 2p spektre stebima 1T- $\text{MoS}_2$  priskirtam dubletui.

Persidengiančiam N 1s bei Mo 3p spektre (3.10. pav. c; žr. 51 p.) buvo išskirti trys Mo 3p dubletai, kurie priskirti  $\text{Mo}^{4+}$  iš 1T- $\text{MoS}_2$  (394.2 eV), 2H- $\text{MoS}_2$  (395.9 eV), bei  $\text{MoO}_x$  (398.6 eV). Pateikiamos tik  $3p_{3/2}$  komponento smailės ryšio energijos, kadangi Mo  $3p_{1/2}$  ryšio energijos skiriasi ~18 eV ir nėra matomos šiame spekto ruože. Papildomai buvo išskirtos dvi N 1s smailės, kurios priskirtos N-Mo (397.0 eV) bei  $\text{NH}_4^+$  (401.6 eV). C 1s spektre (3.10. pav. d; žr. 51 p.) matomos anglies ir anglinių darinių, kurie galėtų būti L-cisteino terminio skilimo produktais, smailės. Apskaičiuotos santykinės koncentracijos iš XPS analizės buvo: 32.8 at.% C, 11.5 at.% Mo, 25.3 at.% S, 26.4 at.% O, ir 4.0 at.% N.

### 5.2.3. $\text{MoS}_2$ /Cisteino elektrodų HER savybių tyrimas

Elektrokatalizinis  $\text{MoS}_2$ /Cisteino dangų aktyvumas tirtas ciklinės voltamperometrijos būdu. Siekiant įvertinti susintetintų elektrodų stabilumą tyrimas buvo atliekamas iki 2000 potencijalo skleidimo ciklų, gautos voltamperogrammos pateiktos 3.11. paveiksle (žr. 52 p.). Nustatyta, jog pradinis reakcijos pradžios potencialas yra -0.2 V tiek grynom, tiek  $\text{MoS}_2$ /Cisteino dangoms. Vykdant CV, vandenilio išskyrimo reakcijos pradžios potencialas išliko pastovus  $\text{MoS}_2$ /Cisteino atveju, o gryno  $\text{MoS}_2$  dangoms padidėjo iki -0.24 V. Negana to, buvo nustatyta, jog dangos su cisteinu pasižymi didesniu kataliziniu aktyvumu, lyginant su gryno  $\text{MoS}_2$  dangomis. Kuomet  $\text{MoS}_2$  buvo susintetintas su cisteinu, pradiniai srovės tankiai ties -0.35 V potencialu tiek 1 mM (3.11. pav. a; žr. 52 p.), tiek 3 mM cisteino (3.11. pav. b; žr. 52 p.) atvejais buvo  $\sim 62 \text{ mA cm}^{-2}$ , tai yra  $\sim 10\%$  didesnės, nei gryno  $\text{MoS}_2$  atveju. Vykdant CV, srovės tankiai išaugo per  $\sim 5 \text{ mA cm}^{-2}$  per pirmus 100 – 200 ciklų, tačiau tolimesniu skleidimų metu sugrįžo netoli pradinės verčių.

Atlikus Tafel nuolinkę skaičiavimus (3.11. pav. intarpai; žr. 52 p.) nustatyta, jog elektrodai su cisteinu pasižymi ženkliai mažesnėmis Tafel nuolinkų vertėmis, lyginant su gryno  $\text{MoS}_2$  elektrodais. Gryno  $\text{MoS}_2$  atveju, pradiniai Tafel nuolinkiai yra  $\sim 90 \text{ mV dec}^{-1}$ , o vykstant vandenilio išskyrimo reakcijai sumažėja iki  $\sim 75 \text{ mV dec}^{-1}$ . Tuo tarpu elektrodai su L-cisteinu pasižymi mažesnėmis vertėmis tiek prieš, tiek po HER apdorojimo. 1 mM glicino atveju pradiniai Tafel nuolinkiai buvo  $57.8 \text{ mV dec}^{-1}$  ir po 1000 ciklų sumažėjo iki  $40.2 \text{ mV dec}^{-1}$ , tuo tarpu 3 mM glicino atveju pradiniai nuolinkiai buvo  $32.6 \text{ mV dec}^{-1}$ , o po 1000 ciklų siekė  $36.2 \text{ mV dec}^{-1}$ . Verta paminėti, jog gauta  $32.6 \text{ mV dec}^{-1}$  Tafel nuolinkio vertė yra artima teorinei  $30 \text{ mV dec}^{-1}$ .

vertei, parodančiai, jog Tafel stadija ( $2H_{ads} \rightarrow H_2$ ) yra vandenilio išskyrimo reakcijos greitį lemianti stadija, tuo tarpu nustatytos Tafel nuolinkų vertės grynam MoS<sub>2</sub> patenka tarp teorinių verčių, būdingų Volmer (120 mV dec<sup>-1</sup>) ir Heyrovsky (40 mV dec<sup>-1</sup>) reakcijos greitį lemiančioms stadijoms.

#### 5.2.4. Ižvalgos apie galimą L-cisteino įsiterpimą

Siekiant nustatyti L-cisteino įtaką hidroterminei molibdeno disulfido sintezei buvo naudota termogravimetrija su masių spektroskopija. Iš gautos termogravimetrinės kreivės (3.12. pav. 1; žr. 54 p.) matyti, jog terminis L-cisteino skilimas prasideda ties ~200 °C, o terminio skilimo metu masių spektroskopijos būdu (3.12. pav. 2-5; žr. 54 p.) nustatytos išsiskyrusios dujos, kurių m/z = 17 (NH<sub>3</sub>), m/z = 34 (H<sub>2</sub>S), bei m/z = 44 (CO<sub>2</sub>), joninės srovės maksimumas nustatytas ties 222 °C.

Pasak Klimo ir bendraautorių [156], kaitinant gryną, hidrotermiškai susintetintą molibdeno disulfidą, 200 – 220 °C temperatūroje stebimas tik H<sub>2</sub>O ir NH<sub>3</sub> išsiskyrimas, tuo tarpu CO<sub>2</sub> bei H<sub>2</sub>S joninės srovės yra be galio mažos šiame temperatūrų intervale. Taip pat nustatyta, jog CS<sub>2</sub>, galimo tiourėjos skilimo produkto, išsiskyrimas vyksta 200 – 400 °C temperatūrų intervale, kuriame gyno MoS<sub>2</sub> atveju stebima viena smailė ties 340 °C, tuo tarpu MoS<sub>2</sub>/Cisteino atveju matomos dvi smailės ties 240 °C bei 470 °C. Terminis cisteino skilimas taip pat nagrinėtas Weiss *et al.* publikacijoje [157]. Teigiami, jog terminis L-cisteino skilimas gali vykti pašalinant –COOH ir –SH grupes, o likusi NH<sub>2</sub>-C<sub>α</sub>-C\* grandinė gali dalyvauti ciklizacijos reakcijoje. Kadangi L-cisteino skilimas prasideda nuo 200 °C, galima daryti prielaidą, jog cisteino funkcinės grupės (-COOH, -SH, -NH<sub>2</sub>) turėtų būti pašalintos MoS<sub>2</sub> hidroterminę sintezę atliekant 220 °C temperatūroje. Todėl, L-cisteino molekulių įsiterpimas į MoS<sub>2</sub> tarpsluoksnius mažai tikėtinas, tačiau adsorbacija ant ir tarp MoS<sub>2</sub> nanolapelių gali būti įmanoma. Kitų krūvų turinčių priemaišinių dalelių ar fragmentų, susidariusių skylant L-cisteinui ar tiourėjai, įsiterpimas yra labiau tikėtinas ir koreliuotų su nustatytu padidėjusiui tarpplokštuminiu atstumu užfiksuoju HRTEM, bei 1T-MoS<sub>2</sub> priskirtinoms smailėms Mo 3d Rentgeno fotoelektronų spektre.

### 5.3. MoS<sub>2</sub>/Histidino dangų elektrocheminių HER savybių tyrimas

#### 5.3.1. MoS<sub>2</sub>/Histidino dangų morfologija

Šio tyrimo metu, molibdeno disulfido elektrodai susintetinti ant anoduoto Ti padėklų hidroterminės sintezės metodu iš amonio heptamolibdato ir tiourėjos tirpalų. Sintezė atlikta 5 val. papildomai pridėjus iki 3 mmol L<sup>-1</sup> D,L-histidino į sintezės tirpalą. Gautų MoS<sub>2</sub>/Histidino dangų morfologija pavaizduota 3.13. paveiksle (žr. 55 p.).

Iš SEM nuotraukų (3.13. pav. a,b; žr. 55 p.) nustatyta, jog TiO<sub>2</sub> nanovamzdelių aukštis yra ~0.56 μm, o vidutinis skersmuo 85 – 90 nm. Nustatytas MoS<sub>2</sub>/Histidino dangos storis yra 0.9 – 1.1 μm, o paviršiaus morfologija panaši į hidrotermiškai susintetinto gryno MoS<sub>2</sub>. Vienintelis pastebėtas skirtumas buvo tai, jog MoS<sub>2</sub>/Histidino nanolapeliai atrodo ilgesni, tuo tarpu gryno MoS<sub>2</sub> atveju nanolapeliai atrodo išsiidėstę tankiau. Sluoksninė MoS<sub>2</sub>/Histidino morfologija buvo matoma HRTEM nuotraukoje (3.13. pav. c; žr. 55 p.). Joje pastebėti įvairūs plokštuminiai iškraipymai bei linkiai, o tarpplokštuminis atstumas variuoja nuo 0.69 nm iki 1.02 nm, kas galėtų būti dėl pašalinių dalelių įsiterpimo MoS<sub>2</sub>/Histidino dangų tarpaluoksniuose.

#### 5.3.2. MoS<sub>2</sub>/Histidino elektrodų elektrocheminiai tyrimai

Suformuotų MoS<sub>2</sub>/Histidino dangų elektrokatalizinės HER savybės tyrinėtos ciklinės voltamperometrijos būdu. Gautose voltamperogramose (3.14. pav.; žr. 56 p.) matomi tiek elektrodų aktyvumo, tiek stabilumo skirtumai, lyginant su gryno MoS<sub>2</sub> dangomis.

Nustatytas elektrodo be histidino (3.14. pav. a; žr. 56 p.) pradinis srovės tankis buvo 94.7 mA cm<sup>-1</sup>, tačiau šio elektrodo stabilumas buvo prastas, kadangi po 100 ciklų srovės tankis sumažėjo iki 75.7 mA cm<sup>-1</sup>, o po 1000 ciklų siekė tik 8.1 mA cm<sup>-1</sup>. Tuo tarpu MoS<sub>2</sub>/Histidino elektrodas (3.14. pav. b; žr. 56 p.) pasižymėjo ženkliai geresniu aktyvumu bei stabilumu. Pradinis srovės tankis beveik nesiskyrė nuo gryno MoS<sub>2</sub> ir buvo 96.6 mA cm<sup>-1</sup>, tačiau tolimesniu skleidimų metu didėjo ir po 100 ciklų pasiekė 108.4 mA cm<sup>-1</sup>. Po 1000 ciklų buvo pastebėtas nežymus srovės tankio sumažėjimas, tačiau skleidžiant iki 2000 ciklų, MoS<sub>2</sub>/Histidino elektrodas pasižymėjo geresniu aktyvumu, lyginant tiek su pradiniais srovės tankiais MoS<sub>2</sub>/Histidino atveju, tiek su gryno MoS<sub>2</sub> srovės tankiais viso CV matavimo metu.

Apskaičiuotos Tafel nuolinkų vertės gryno MoS<sub>2</sub> elektrodiui (3.14. pav. a intarpas; žr. 56 p.) parodo, jog HER vyksta pagal Volmer – Heyrovsky

mechanizmą, o gautos  $75 - 79 \text{ mV dec}^{-1}$  vertės patenka tarp teorinių verčių reakcijos greitį lemiančioms Volmer ir Heyrovsky stadijoms.  $\text{MoS}_2/\text{Histidino}$  elektrodo Tafel nuolinkai po pirmojo ciklo buvo  $74.2 \text{ mV dec}^{-1}$ , tai yra, panašūs kaip ir gryno  $\text{MoS}_2$  atveju. Tačiau, po ciklinimo, Tafel nuolinkai sumažėjo iki  $48.2 \text{ mV dec}^{-1}$  (po 1000 ciklų) ir mažai keitėsi praskleidus iki 2000 ciklų. Tai leidžia manyti, jog būtent Heyrovsky stadija yra reakcijos greitį lemianti stadija, o vykstant vandenilio išskyrimo reakcijai yra pagerinama krūvio pernaša į  $\text{MoS}_2/\text{Histidino}$  aktyviąsias pozicijas.

Papildomi susintetintų elektrodų tyrimai atliki naudojant elektrocheminio impedanso spektroskopiją. Elektrocheminio impedanso spektrai užrašyti ties  $-0.2 \text{ V}$ ,  $-0.25 \text{ V}$ , ir  $-0.3 \text{ V}$  siekiant atvaizduoti greitėjančią vandenilio išskyrimo reakciją. Gautuose Nyquist grafikuose (3.15. pav. ; žr. 57 p.) buvo matomi du pusrutuliai, o gautų spektrų kreivės visiems tertiems elektrodams buvo panašios, kas gali reikšti, jog HER mechanizmas nesikeičia, o tai koreliuoja su anksčiau minėtu Tafel nuolinkų apskaičiavimu. Tieki šviežiai susintetintas  $\text{MoS}_2/\text{Histidino}$  elektrodas, tiek  $\text{MoS}_2/\text{Histidino}/\text{CV}$  (prieš EIS matavimus atlikta 1000 potencialo skleidimo ciklų) elektrodas pasižymėjo mažesniu impedanso dydžiu ties konkrečiu potencialu, lyginant su grynu  $\text{MoS}_2$ , kas parodo, jog  $\text{MoS}_2/\text{Histidino}$  elektrodai pasižymi didesniu elektrokataliziniu aktyvumu.

Sistemai aprašyti buvo naudojama ekvivalentinė grandinė, pavaizduota 3.15. paveiksle (a intarpas; žr. 57 p.). Tokia ekvivalentinė grandinė dažnai naudojama aprašant HER rūgštiniuose ar šarminiuose elektrolituose [158]. Atsižvelgiant į paviršiaus nehomogeniškumą, ekvivalentinėje grandinėje vietoje talpos naudojami pastovios fazės elementai (CPE). Apskaičiuoti ekvivalentinės grandinės parametrai pateikiami 2 lentelėje (žr. 59 p.).

Krūvio pernašos varža  $R_{ct}$  yra atvirkščiai proporcinga reakcijos greičiui, t.y. mažesnė  $R_{ct}$  reiškia greitesnę vandenilio išskyrimo reakciją. Grynas  $\text{MoS}_2$  elektrodas pasižymėjo mažesne  $R_{ct}$  už  $\text{MoS}_2/\text{Histidino}$  elektrodą, tačiau,  $\text{MoS}_2/\text{Histidino}/\text{CV}$  elektrodai taip pat pasižymėjo mažesnėmis  $R_{ct}$ , ypač ties aukštesniais potencialais, kas leidžia manyti, jog vykstant vandenilio išskyrimo reakcijai, šios greitis didėja. Pseudotalpa  $C_p$  priklauso nuo adsorbuotų dalelių, kas vandenilio išskyrimo reakcijoje yra  $\text{H}_{\text{ads}}$ , paviršiaus padengimo laipsnio.  $C_p$  vertės apskaičiuotos naudojant Brug *et al.* lygtį (1 lygtis) [160]:

$$C_p = T_p^{\frac{1}{n}} \left( \frac{1}{R_s + R_{ct}} + \frac{1}{R_p} \right)^{1-\frac{1}{n}} \quad (1)$$

Čia  $T_p$  – CPE<sub>p</sub> elemento vertė,  $n$  – pastovios fazės eksponentė, o  $R_{ct}$ ,  $R_s$ , bei  $R_p$  – atitinkamai, krūvio pernašos, tirpalo ir poliarizacinės varžos. Pasak Lasia

[161], kylant virštampiui, paviršiaus padengimo laipsnis  $\theta_H$  artėja link 1, o  $C_p$  vertės turėtų arba didėti, arba nesikeisti aukštesniuose virštampiuose. Tačiau MoS<sub>2</sub> katalizatorių su histidino atvejis stebima priešinga tendencija. Didžiausios  $C_p$  vertės nustatytos MoS<sub>2</sub>/Histidino elektrodiui, o mažiausios – grynam MoS<sub>2</sub>. Ties -0.2 V MoS<sub>2</sub>/Histidino elektrodas pasižymėjo triskart didesnėmis  $C_p$  vertėmis (150.10 mF cm<sup>-2</sup>) nei grynas MoS<sub>2</sub> (49.59 mF cm<sup>-2</sup>), kas parodo, jog hidroterminės sintezės su histidinu metu susiformuoja MoS<sub>2</sub> dangos su daugiau katalitiškai aktyvių HER pozicijų. MoS<sub>2</sub>/Histidino/CV elektrodas pasižymėjo ženkliai mažesnėmis  $C_p$  vertėmis, o tai gali reikšti, jog vykstant vandenilio išskyrimo reakcijai yra paveikiamas katalitiškai aktyvus MoS<sub>2</sub> paviršius. Nustatyta, jog didinant potencialą polarizacijos varža  $R_p$  ženkliai sumažėjo visiems tertiems elektrodams. Didžiausias pokytis pastebėtas grynam MoS<sub>2</sub> elektrodiui, nepaisant to, jog ties -0.2 V šio elektrodo  $R_p$  vertės buvo kiek daugiau nei dvigubai didesnės už MoS<sub>2</sub> elektrodotu su histidinu. Taip pat, MoS<sub>2</sub>/Histidino/CV elektrodo  $R_p$  vertės buvo mažesnės nei MoS<sub>2</sub>/Histidino elektrodo, kas leidžia manyti, jog vykstant HER greitėja H<sub>2</sub> adsorbcija/desorbcija.

Elektrokatalizatorių aktyvumas taip pat priklauso nuo elektrochemiškai aktyvaus paviršiaus ploto. Tikslų hidrotermiškai susintetinto MoS<sub>2</sub> paviršiaus plotą nustatyti sunku, tačiau dvigubo elektrinio sluoksnio talpos  $C_{dl}$  apskaičiavimais galima įvertinti tarpfazinį plotą tarp elektrolito ir elektrodo paviršiaus. Siekiant nustatyti  $C_{dl}$  buvo atlikta ciklinė voltamperometrija -0.10 – 0.10 V potencialų ruože keičiant skleidimo greitį ( $v = 25, 50, 75, 100, 125, 150, 175, 200 \text{ mV s}^{-1}$ ).  $C_{dl}$  nustatyta iš grafiko (3.16. pav. ; žr. 60 p.), kuriamo pavaizduota srovės tankio skirtumo priklausomybė nuo skleidimo greičio, o šios tiesės nuolinkis yra dviguba  $C_{dl}$ . Mažiausia  $C_{dl}$  (26.88 mF cm<sup>-2</sup>) nustatyta grynam MoS<sub>2</sub> elektrodiui. MoS<sub>2</sub>/Histidino elektrodas pasižymėjo beveik dvigubai didesne  $C_{dl}$  (44.74 mF cm<sup>-2</sup>), tačiau po HER apdorojimo  $C_{dl}$  sumažėjo iki 37.14 mF cm<sup>-2</sup>, kas rodo, jog vykstant HER elektrochemiškai aktyvus paviršiaus plotas mažėja.

### 5.3.3. MoS<sub>2</sub>/Histidino dangų charakterizavimas

Suformuotų elektrodų paviršiaus prieš ir po ciklinės voltamperometrijos matavimų elementinės sudėties analizei atlikta Rentgeno fotoelektronų spektroskopija. Gauti Mo 3d spektrai (3.17. pav. ; žr. 61 p.) išskaidyti į keturis dubletus su 3d<sub>5/2</sub> ir 3d<sub>3/2</sub> komponentais. Didžiausio intensyvumo dubletas ties 228.6 eV (3d<sub>5/2</sub>) ir 231.8 eV (3d<sub>3/2</sub>) buvo priskirtas Mo<sup>4+</sup> iš 1T-MoS<sub>2</sub>, sekantis Mo<sup>4+</sup> dubletas, kurio komponentai buvo ties 229.4 eV ir 232.5 eV priskirtas

$2\text{H-MoS}_2$ , o trečiasis  $\text{Mo}^{4+}$  dubletas ties 230.6 eV ir 233.8 eV priskirtas  $\text{MoO}_2$ . Paskutinysis dubletas, kurio  $3d_{5/2}$  ir  $3d_{3/2}$  komponentai stebimi ties 232.8 eV ir 235.9 eV, priskirtas  $\text{Mo}^{6+}$  iš  $\text{MoO}_3$ .

Galimam priemaišinių dalelių įsiterpimui į tarpsluoksnius įvertinti buvo atlikti FTIR spektroskopijos tyrimai. Gautame FTIR spektre (3.18. pav. ; žr. 63 p.) matoma smailė ties  $605\text{-}607 \text{ cm}^{-1}$  priskirta Mo-S tempimo vibracijai, tuo tarpu smailė ties  $928 \text{ cm}^{-1}$  sietina su S-S ryšiais [162]. Aiškiai išreikšta smailė ties  $1394 \text{ cm}^{-1}$  gryno  $\text{MoS}_2$  atveju priskirta N-H deformacinėms vibracijoms, tuo tarpu  $\text{MoS}_2/\text{Histidino}$  atveju ši smailė pasilenka į  $1400\text{-}1402 \text{ cm}^{-1}$ . Smailės, esančios  $750\text{-}1000 \text{ cm}^{-1}$  ruože priskirtinos Mo-O ryšiams, o pasak literatūros, smailė ties  $1090 \text{ cm}^{-1}$  priskirtina terminalinio Mo-O tempimo vibracijai. Dvi mažo intensyvumo smailės ties  $\sim 1630 \text{ cm}^{-1}$  bei  $\sim 1670 \text{ cm}^{-1}$  matomos pavyzdžiuose su histidinu ir priskiriamos amidinio C=O ryšio vibracijoms. Be to, smailė ties  $\sim 1230 \text{ cm}^{-1}$  gali būti priskiriama CN tempimo ir NH lenkimo vibracijoms amidoose, tuo tarpu smailė ties  $574 \text{ cm}^{-1}$  gali būti priskiriama neplokštuminio C=O lenkimo vibracijai [164].

Pasak Weiss *et al.* [157], kaitinant  $220 \text{ }^{\circ}\text{C}$  temperatūroje histidino molekulės N galas gali reaguoti su gretimos molekulės C galu ir sudaryti peptidinį ryšį, o tai galėtų paaiškinti FTIR spektruose matomas peptidiniamis ryšiams būdingas smailės. Yra tikėtina, jog šie terminio histidino skilimo produktai galėtų adsorbuotis ant  $\text{MoS}_2$  nanolapelių, taip padidindami 1T fazės stabilumą, o tai koreliuotų su XPS bei elektrocheminės analizės metu gautais duomenimis.

#### 5.4. Elektrocheminių HER savybių pagerinimas anodiškai apdorojant hidrotermiškai susintetintą $\text{MoS}_2$

Siekiant padidinti  $\text{MoS}_2$  elektrokatalizines vandenilio išskyrimo reakcijos savybes be hidroterminės sintezės sąlygų modifikavimo taip pat yra naudojami ir įvairūs jau susintetintų molibdeno disulfidų apdorojimo metodai, tokie kaip elektrocheminis sieros vakansijų įterpimas [165], apdorojimas išoriniu elektriniu lauku [166] ar tarpkristalitinių sričių generavimas apšvitinant lazerine spinduliuote [167].

Šiame darbe  $\text{MoS}_2/\text{Cisteino}$  elektrodai buvo sintetinami hidroterminės sintezės būdu ant anoduoto Ti pagrindų, naudojant tokią pačią procedūrą, kaip aprašyta 4 bei 5.2.1. skyriuose, po sintezės juos anodiškai apdorojant ir po to nagrinėjant elektrodų HER savybes. Anodinis apdorojimas buvo atliekamas darbiniui elektrodai ( $\text{MoS}_2/\text{Cisteinui}$ ) užduodant teigiamą potencialą ciklinės voltamperometrijos metu, iš pradžių skleidžiant į anodinę pusę, o vėliau į katodinę pusę.

#### 5.4.1. MoS<sub>2</sub>/Cisteino elektrodų anodinis apdorojimas ir elektrocheminiai matavimai

MoS<sub>2</sub>/Cisteino elektrodai anodiškai praskleisti nuo -0.2 V iki +2.0 V, o gautos srovės tankio priklausomybės nuo įtampos kreivės pavaizduotos 3.19 paveiksle (žr. 64 p.). Pirmojo anodinio ciklo metu (3.19. pav. a,b; žr. 64 p.) matoma anodinė smailė ties ~+1.0 V, kuri ženkliai sumažėja sekančių skleidimo ciklų metu. Tai atitinka Bonde *et al.* aprašytus matavimus [168], tačiau, skirtingai nei minėtoje publikacijoje, vandenilio išskyrimo reakcijos greičio sumažėjimas nestebimas. Priešingai, po pirmo anodinio apdorojimo ciklo MoS<sub>2</sub>/Cisteino elektrodas pasižymėjo geresnėmis HER savybėmis ir išlaikė didesnį aktyvumą po papildomų anodinio apdorojimo ciklų, kurių metu anodinės srovės tankis artėjo link nulio. Pasak [168] anodinės srovės tankio smailės mažėjimas turėtų reikšti, jog ant pagrindo mažėja MoS<sub>2</sub> kiekis, tačiau ženklų, jog MoS<sub>2</sub>/Cisteino dangos būtų pažeistas nepastebėta, o anodiškai apdoroti elektrodai pasižymėjo didesniais HER greičiais, lyginant su anodiškai neapdorotu MoS<sub>2</sub>/Cisteino elektrodu.

Taip pat nustatyta, jog elektrodo aktyvumui (3.20. pav; žr. 65 p.) turi įtakos ir pasirinktas anodinio apdorojimo posūkio potencialas, t.y. potencialas, kurį pasiekus CV metu keičiama skleidimo kryptis (iš anodinio skleidimo į katodinį arba atvirkščiai). Kuomet anodinio apdorojimo metu potencialas skleistas iki +0.55 V, elektrodo aktyvumas nesikeitė nuo prieš apdorojimą registruotų verčių. Padidinus posūkio potencialą virš +0.6 V buvo stebimas padidėjęs elektrodo aktyvumas, o didžiausias aktyvumas gautas apdorojant iki +0.75 V posūkio potenciale. Pasak Kautek *et al.* anodiškai apdorojant 2D-MoS<sub>2</sub> nanolapelines dangas rūgštiniuose elektrolituose vyksta MoS<sub>2</sub> kristalo briaunų korozija [169]. Remiantis tuo, anodinę smailę, stebimą ties ~+0.85 V, galima priskirti elektrocheminiam MoS<sub>2</sub> briaunų ēsdinimui, kur srovės tankis yra proporcingsas MoS<sub>2</sub> briaunų ilgiui, o smailės potencialas priklauso nuo anodinio skleidimo greičio.

Antrosios smailės, stebimos prie didesnių skleidimo greičių (3.19. pav b; žr. 64 p.) prigimtis nėra aiški. Pasak [168] šios smailės atsiradimas galimai yra MoS<sub>2</sub> bazinės plokštumos ēsdinimo indikacija. Tačiau verta paminėti, jog MoS<sub>2</sub> ēsdinimo metu gali oksiduotis ne tik molibdenas ( $\text{Mo}^{4+} \rightarrow \text{Mo}^{6+}$ ), bet ir sieros oksidaciją yra tikėtina ( $\text{S}^{2-} \rightarrow \text{S}_2^{2-}$ ;  $\text{S}_2^{2-}$  ir/ar  $\text{S}^{2-} \rightarrow \text{SO}_4^{2-}$ ). Todėl anodinėje kreivėje gali atsirasti papildomų smailių, kurias galima būtų priskirti sieros oksidacijai. Kautek *et al.* savo publikacijoje MoS<sub>2</sub> bazinės plokštumos ēsdinimo ties +1.2 V neregistravo, o antroji smailė nėra išskiriama esant

mažesniems skleidimo greičiams (3.19. pav. a; žr. 64 p.). Tai leidžia manyti, jog nustatytais MoS<sub>2</sub>/Cisteino elektrodų aktyvumo padidinimas neturėtū būti siejamas su aktyvių briaunų kieko padidinimu ēsdinant bazinę MoS<sub>2</sub> plokštumą. Tikėtina, jog HER greičio padidėjimas sietinas su MoS<sub>2</sub> nanolapelių briaunų ilgio ar aktyvumo padidinimu.

Elektrodo aktyvumo sumažėjimas po ilgo anodinio apdorojimo gali atsirasti dėl sumažėjusio MoS<sub>2</sub> nanolapelių kieko ant TiO<sub>2</sub> paviršiaus, arba dėl energetiškai aktyvesnių pozicijų ēsdinimo iššaukiama MoS<sub>2</sub> briaunų deaktyvacijos. Pasak Kibsgaard ir bendraautorių [170], keičiantis elektrochemiškai aktyviam elektrokatalizatoriaus paviršiaus plotui ir nesikeičiant vandenilio adsorbcijos laisvajai energijai ( $\Delta G_{H^*}$ ), stebimas mainų srovės mažėjimas bei nesikeičiantis Tafel nuolinkis. Iš CV matavimų nustatyta, jog Tafel nuolinkis išlieka beveik nepakitus nuo +0.1 V iki +0.55 V posūkio potencialų ruože. Toliau didinant posūkio potencialą stebimas Tafel nuolinkio sumažėjimas, o +0.8 V – +0.9 V ruože Tafel nuolinkis vėl nesikeičia. Mainų srovės didėja iki +0.75 V, o tolimesniuose posūkio potencialuose stebimas staigus mainų srovės sumažėjimas. Tokia tendencija galėtų reikšti, jog iš pradžių yra padidinamas aktyviųjų HER pozicijų skaičius, o aukštesniuose posūkio potencialuose stebimas elektrokatalizatoriaus elektrochemiškai aktyvaus paviršiaus ploto mažėjimas. Tafel nuolinkio pokytis leidžia teigti, jog anodinio apdorojimo metu kinta HER greitį lemianti stadija. HER greitis yra tiesiogiai siejamas su aktyviųjų pozicijų  $\Delta G_{H^*}$ , o tai leidžia manyti, jog kinta aktyviųjų pozicijų prigimtis.

Anodinio apdorojimo metu pratekėjusio krūvio įtaka MoS<sub>2</sub>/Cisteino elektrodo aktyvumo padidinimui įvertinta užduodant pastovaus anodinio potencialo impulsus (3.21. pav.; žr. 67 p.). Iš pradžių, tiek pratekėjęs krūvis, tiek HER greitis didėja (3.21. pav. a; žr. 67 p.), o nuo ketvirtrojo anodinio impulso pratekėjęs krūvis mažėja kiekvieno sekancio impulso metu. Tuo tarpu elektrodo aktyvumo mažėjimas pastebėtas tik po 9 anodinių impulsų, o viso eksperimento metu HER srovės tankiai sumažėjo ~10 mA cm<sup>-2</sup> nuo maksimalaus registratorio srovės tankio (3.21. pav. b; žr. 67 p.). Tai galėtų reikšti jog pasiekiamas energetiškai aktyvesnių pozicijų MoS<sub>2</sub> briaunose įsisotinimas.

#### 5.4.2. Anodiškai apdorotų MoS<sub>2</sub>/Cisteino elektrodų charakterizavimas

Iš SEM nuotraukų (3.22. pav.; žr. 68 p.) matyti, jog MoS<sub>2</sub>/Cisteino dangos pilhai padengia visą Ti/TiO<sub>2</sub> pagrindo paviršių ir atrodo identiškai 5.2.

skyriuje aprašytoms dangoms. Atlikus anodinį apdorojimą 12 minučių ties +0.72 V potencialu, dangų paviršius išlieka nepakitęs, vienintelis skirtumas yra tai, jog šiose dangose matoma keletas įtrūkimų (3.22. pav. b; žr. 68 p.). Kuomet anodinis potencialas padidintas iki +2.5 V, dangų morfologija ženkliai skiriasi, matomas dalinis MoS<sub>2</sub> nanolapelių praradimas. EDX metodu nustatyta, jog S/Mo santykis, tiek neapdorotam, tiek poliarizuotam 12 min prie +0.72 V MoS<sub>2</sub>/Cisteinui buvo 1.93 – 2.03.

MoS<sub>2</sub>/Cisteino elektrodo paviršiaus struktūriniai pokyčiai anodinio apdorojimo metu įvertinti naudojant Rentgeno fotoelektronų spektroskopiją. XPS nustatytas S/Mo santykis neapdorotam MoS<sub>2</sub>/Cisteino elektrodai buvo 2.05, tuo tarpu anodiškai poliarizuoto iki +2.5 V MoS<sub>2</sub>/Cisteino S/Mo santykis padidėjo iki 3.32. S/Mo santykio priklausomybė nuo anodinio apdorojimo potencijalo pateikta 3.23. paveiksle (žr. 69 p.). Nustatyta, jog S/Mo santykis bei santykinis tilteliniių S<sub>2</sub><sup>2-</sup> (angl. *bridging*) ir viršūninių (angl. *apical*) S<sup>2-</sup> grupių kiekis tiesiogiai priklauso nuo anodinio potencijalo ir nepriklauso nuo apdorojimo trukmės. EDX bei XPS nustatyti S/Mo santykiai parodo, jog MoS<sub>2</sub>/Cisteino elektrodo aktyvumo padidėjimas nėra sietinas su sieros vakansijų suformavimu anodinio apdorojimo metu.

Pasak literatūros šaltinių, vakuumė perskelto gryno 2H-MoS<sub>2</sub> kristalo Mo 3d<sub>5/2</sub> komponento ryšio energija yra 229.1 eV – 229.4 eV, tuo tarpu S 2p<sub>3/2</sub> komponento ryšio energijos yra 162.0 eV – 162.4 eV [69]. Li<sup>+</sup> įterpimas į 2H-MoS<sub>2</sub> struktūrą iššaukia papildomų smailių atsiradimą Mo 3d ir S 2p spektruose, kuriuose papildomos smailės registruoamos, atitinkamai ties 1.1 eV ir 0.8 eV mažesnėmis ryšio energijomis lyginant su grynu 2H-MoS<sub>2</sub> [68]. Po eksfoliavimo butilličio junginiai ir pašalinus Li, literatūros šaltiniuose pateikiami įvairūs MoS<sub>2</sub> Rentgeno fotoelektronų spektrų aprašymai: nepakitę nuo gryno 2H-MoS<sub>2</sub> [171] ar tik stebimas smailių išplatėjimas [172], iki papildomai atsirandančių smailių ties 0.8 – 0.9 eV mažesnėmis ryšio energijomis [39, 70]. Hidrotermiškai susintetintų 2D-MoS<sub>2</sub> atveju XPS spektrai aprašyti vienu [173] ar keliais dubletais [174, 175]. Mo 3d ir S 2p spektruose registruoamos smailės su mažesne už grynam 2H-MoS<sub>2</sub> būdinga ryšio energija dažnai priskiriamos 1T-MoS<sub>2</sub> arba netvarkiai 1T'-MoS<sub>2</sub> fazėms. Apart 3d<sub>5/2</sub> komponento ties ~232.8 eV priskirtino Mo<sup>6+</sup>, taip pat pateikiamos ir kitos, aukštesnės ryšio energijos smailės, stebimos ties 229.7 eV – 230.4 eV Mo 3d spektre ir 163.0 eV – 163.6 eV S 2p spektre. Šios Mo 3d smailės literatūroje priskiriamos Mo<sup>5+</sup> esančio sulfiduose, oksiduose, ar oksisulfiduose [71, 176, 177], tuo tarpu S 2p smailės stebimos amorfiniuose MoS<sub>x</sub>, kur 2<x<6. Amorfiniams molibdeno sulfidams būdingos S 2p smailės ties 163.1 eV – 163.5 eV gali būti priskiriamos tiltelinėms S<sub>2</sub><sup>2-</sup> ir viršūninėms S<sup>2-</sup> grupėms, tuo tarpu smailės ties 161.6 eV – 161.8 eV gali būti priskiriamos

neprisotintoms (angl. *unsaturated*)  $S^{2-}$  ir galinėms (angl. *terminal*)  $S_2^{2-}$  grupėms [178, 179].

Gauti Mo 3d ir S 2p spektrai (3.24. pav.; žr. 70 p.) buvo išskaidyti į Mo  $3d_{5/2}$  ir  $3d_{3/2}$  bei S  $2p_{3/2}$  ir  $2p_{1/2}$  komponentus, Mo  $3d_{5/2}$  ir S  $2p_{3/2}$  smailių ryšio energijos pateikiamos 5 lentelėje (žr. 71 p.), o Mo  $3d_{3/2}$  bei S  $2p_{1/2}$ , pasižymintys atitinkamai 3.15 eV ir 1.16 eV didesnėmis ryšio energijomis paprastumo dėlei 5 lentelėje nėra pateikiami. Mo 3d spektre matomas  $3d_{5/2}$  komponentas su mažiausia ryšio energija (228.8 eV – 229.0 eV) priskirtas  $Mo^{4+}$  iš 1T-MoS<sub>2</sub>,  $3d_{5/2}$  komponentas su 229.7 eV – 230.0 eV priskirtas  $Mo^{4+}$  iš 2H-MoS<sub>2</sub>. Taip pat nustatytos aukštesnių ryšio energijų  $3d_{5/2}$  komponentų smailės, kur ties 230.8 eV – 230.9 eV matoma smailė priskirta  $Mo^{5+}$  iš molibdeno oksidui, oksisulfidui ar sulfidui, o smailė ties 232.4 eV – 232.5 eV ryšio energija priskirta  $Mo^{6+}$  iš MoO<sub>3</sub>.

Literatūroje teigama, jog  $Mo^{5+}$  junginiai gali būti tarpiniai  $(NH_4)_2Mo_7O_{24}$  [180] ar MoO<sub>3</sub> [181] sulfidinimo bei terminio molibdatų skilimo [182] junginiai, kas leidžia daryti išvadą, jog  $Mo^{5+}$  junginiai, pavyzdžiu  $MoO_xS_{4-x}^{2-}$  [183],  $MoS_4^{2-}$ ,  $MoS_3$  [122],  $[Mo_2S_{12}]^{2-}$ ,  $[Mo_3S_{13}]^{2-}$  [184, 185] gali susidaryti hidroterminės MoS<sub>2</sub>/Cisteino sintezės metu. S 2p spektras išskaidytas į du dubletus, kurių S  $2p_{3/2}$  komponentų smailės stebimos ties 161.6 eV – 161.9 eV. Ši ryšio energijos vertė yra kiek nutolusi nuo grynam 2H-MoS<sub>2</sub> būdingų verčių (~162.2 eV), tačiau pakankamai artima smailių, priskiriamų neprisotintoms  $S^{2-}$  ir galinėms  $S_2^{2-}$  grupėms, verčių. Antrasis dubletas ties 163.2 eV – 163.4 eV gali būti priskiriamas tiltelinėms  $S_2^{2-}$  ir viršūninėms  $S^{2-}$  grupėms, tuo tarpu keliuose pavyzdžiuose papildomai išskiriamas trečiasis, mažo intensyvumo dubletas ties ~169 eV, kuris atsiranda dėl SO<sub>x</sub>, susiformavusio dėl pavyzdžio oksidacijos laikant juos ore prieš tyrimą.

Aiškių sąsajų tarp Mo 3d Rentgeno fotoelektronų spektrų ir anodinio apdorojimo trukmės ar naudoto potencijalo nenustatyta. Tuo tarpu S 2p spektre pastebėta, jog S  $2p_{3/2}$  komponento smailės ties 163.2 – 163.4 eV plotas tiesiogiai priklauso nuo užduoto anodinio potencijalo apdorojimo metu (3.24. pav.; žr. 70 p. ir 5 lentelę; žr. 71 p.). Tai leidžia daryti išvadą, jog MoS<sub>2</sub>/Cisteino elektrodo aktyvumo padidinimas turėtų būti siejamas su tiltelių  $S_2^{2-}$  ir viršūnių  $S^{2-}$  grupių kieko padidinimu anodiškai apdorojant pagamintą elektrodą, o tai koreliuoja ir su apskaičiuotomis Tafel nuolinkio vertėmis, kur, pasak literatūros, 38–57 mV dec<sup>-1</sup> Tafel nuolinkio vertės yra būdingos tiltelines  $S_2^{2-}$  ir viršūnines  $S^{2-}$  grupes turintiems molibdeno sulfidams [111, 177]. Verta paminėti, jog laikoma, kad viršūninės  $S^{2-}$  grupės nėra aktyvios HER [179, 186], todėl labiausiai tikėtina, jog elektrodo aktyvumo

padidėjimas susijęs tik su tiltelinės  $S_2^{2-}$  grupės kieko padidėjimu anodinio apdorojimo metu.

#### 5.4.3. Atkaitinimo įtaka $\text{MoS}_2/\text{Cisteino}$ elektrodams ir jų aktyvavimas anodiniu apdorojimu

Atkaitinimo įtaka elektrodo aktyvumui, S/Mo santykui ir santykiniam tiltelinių  $S_2^{2-}$  ir viršūninių  $S^{2-}$  grupių kiekiui aprašyta literatūroje [184, 185]. Kaip ir pateiktose publikacijose, atkaitinus anodiškai apdorotą ties +0.85 V  $\text{MoS}_2/\text{Cisteino}$  elektrodą vakuume ties 300 °C, pastebėtas S/Mo santykio sumažėjimas nuo 3.2 iki 2.2. Mo 3d spektre didelių pokyčių nepastebėta, tuo tarpu  $2p_{3/2}$  komponento ties 163.2 eV, priskirto tiltelinėms  $S_2^{2-}$  ir viršūninėms  $S^{2-}$  grupėms, smailės plotas po atkaitinimo sumažėjo beveik dvigubai nuo 59.1 % iki 27.2 % (3.25. pav.; žr. 73 p.).

Po atkaitinimo,  $\text{MoS}_2/\text{Cisteino}$  elektrodo aktyvumas ženkliai sumažėjo, srovės tankis ties -0.35 V siekė 11.9 mA cm<sup>-2</sup>, t.y. beveik dešimt kartų mažesnis, nei neapdoroto  $\text{MoS}_2/\text{Cisteino}$ . Taip pat nustatyta, jog po atkaitinimo padidėjo Tafel nuolinkio ir mainų srovės vertės (6 lentelė; žr. 74 p.). Nustatytais 131.1 mV dec<sup>-1</sup> Tafel nuolinkis rodo, jog anodiškai apdoroto ir atkaitinto  $\text{MoS}_2/\text{Cisteino}$  elektrodo aktyvumas panašus į gryno 2H- $\text{MoS}_2$  elektrodo aktyvumą [187], o Volmer stadija tampa reakcijos greitį lemiančia stadija.

Apdorotiems ir atkaitintiems  $\text{MoS}_2/\text{Cisteino}$  elektrodams papildomai atlikus anodinį apdorojimą, HER greitis (3.26. pav.; žr. 74 p.) vėl padidėjo. Kuomet anodinis ciklas praskleistas nuo -0.05 V iki +1.15 V, HER srovės tankis išaugo iki ~46 mA cm<sup>-2</sup>, kas yra nors ir mažesnė vertė, nei nekaitinto elektrodo atveju, tačiau beveik tris kartus didesnė, lyginant su  $\text{MoS}_2/\text{Cisteino}$  elektrodu iškart po atkaitinimo. Nustatyta, jog Tafel nuolinkio bei mainų srovės vertės (6 lentelė; žr. 74 p.) mažėja didinant posūkio potencialą iki +1.3 V, toliau didinant potencialą mažėja tik mainų srovė, o Tafel nuolinkio vertės nusistovi ties ~76 mV dec<sup>-1</sup>. Kaip minėta anksčiau, tokius pokyčius reikėtų sieti su  $\text{MoS}_2$  kieko ant paviršiaus sumažėjimu, o ne 1T- $\text{MoS}_2$  fazės [126] ar aktyviųjų briaunų ilgio sumažėjimu [137].

#### 5.4.4. $\text{MoS}_2/\text{Cisteino}$ elektrodo HER stabilumo tyrimas po anodinio apdorojimo

Pasak literatūros,  $\text{MoS}_x$  elektrokatalizatoriams uždavus katodinius potencinalus ilgainiui matomas HER viršūtampio didėjimas [188, 189]. To pasekoje,

mažėja HER greitis prie tam tikro potencijalo, kaip ir S/Mo santykis bei S 2p<sub>3/2</sub> Rentgeno fotoelektronų spektro smailė, priskiriamą tiltelinėms S<sub>2</sub><sup>2-</sup> ir viršūninėms S<sup>2-</sup> grupėms.

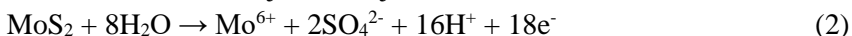
MoS<sub>2</sub>/Cisteino elektrodų stabilumas įvertintas chronopotenciometrijos metodu (3.27 pav.; žr. 75 p.), stebint virštampio pokytį ties fiksuotu -10 mA cm<sup>-2</sup> srovės tankiu 12 valandų laikotarpyje. Tik susintetinto MoS<sub>2</sub>/Cisteino pradinis virštampis buvo -0.248 V ir mažai kito 12 valandų laikotarpyje (3.27. pav. 1 kreivė; žr. 75 p.). Tam pačiam elektrodui praskleidus potencialą nuo -0.25 V iki +0.85 V, o po to registruojant virštampio kitimą laike (3.27. pav. 2 kreivė; žr. 75 p.) pastebėta, jog pradinis virštampis sumažėjo iki -0.236 V, o po 12 valandų pasiekia tokią pat vertę, kaip ir neapdoroto MoS<sub>2</sub>/Cisteino atveju. Pakartojus šią procedūrą (skleidimo iki +0.85 V ir 12 val. katodinio poliarizavimo ties -10 mA cm<sup>-2</sup>) dar du kartus (3.27. pav. 3 ir 4 kreivės; žr. 75 p.) stebimas greitesnis virštampio didėjimas, tačiau pradiniai virštampiai yra mažesni, lyginant su neapdorotu MoS<sub>2</sub>/Cisteino elektrodu. Nustatyta, jog ilgalaikis nuoseklus anodinis apdorojimas kartu su 12 val. katodiniu poliarizavimu daro neigiamą įtaką elektrodo HER stabilumui, kadangi po trečio anodinio-katodinio apdorojimo -0.253 V virštampis pasiekiamas beveik triskart greičiau, lyginant su neapdorotu MoS<sub>2</sub>/Cisteinu.

MoS<sub>2</sub>/Cisteino dangų kristališumas prieš ir po anodinio apdorojimo įvertintas XRD. Gautose difraktogramose matoma, jog neapdoroto MoS<sub>2</sub>/Cisteino difraktograma (3.28. pav. 1; žr. 77 p.) atitinka MoS<sub>2</sub> priskiriamą PDF kortelę, o smailė, priskiriamą (002) plokštumai pasislinkusi nuo įprastinės  $2\theta = 14.4^\circ$  vertės į  $2\theta = 9.0^\circ$  dėl galimo priemaišinių dalelių įsiterpimo. Po HER MoS<sub>2</sub>/Cisteino difraktogramoje (3.28. pav. 2; žr. 77 p.) matomi skirtumai, nėra išskiriama smailė ties  $2\theta = 9.0^\circ$  ir  $2\theta = 18.6^\circ$ , atsiranda smailė ties  $2\theta = 13.2^\circ$ , o visa difraktograma panaši į gryno 2H-MoS<sub>2</sub>. Po trumpo anodinio apdorojimo difraktograma išlieka nepakitusi, tačiau praskleidus iki +2.5 V (3.28. pav. 3; žr. 77 p.) stebima išplatėjusi smailė ties  $2\theta = 14.0^\circ$ , o (100) ir (110) plokštumoms priskiriamos smailės, atitinkamai ties  $2\theta = 32.9^\circ$  ir  $2\theta = 38.7^\circ$ , išnyksta, kaip manoma, arba dėl per mažo MoS<sub>2</sub> kieko ant pagrindo, arba dėl besiformuojančio amorfino MoS<sub>x</sub>, pasižyminčiu didesniu S/Mo santykiu.

Galimi struktūriniai MoS<sub>2</sub>/Cisteino pokyčiai po HER apdorojimo įvertinti XPS metodu. MoS<sub>2</sub>/Cisteino elektrodo po HER Mo 3d spektre (3.29. pav. c; žr. 78 p.) intensyviausia smailė matoma ties 228.5 eV. Visi Mo 3d spektro po HER dubletai, apart Mo<sup>6+</sup> priskiriamam dubletui ties Mo 3d<sub>5/2</sub> komponento 232.6 eV ryšio energija, matomi mažesnėse ryšio energijose, lyginant su neapdoroto MoS<sub>2</sub>/Cisteino Mo 3d spektru (3.29. pav. a; žr. 78 p.). Verta paminėti, jog žemesnio oksidacinių laipsnio Mo junginių XPS smailės

matomos prie mažesnių ryšio energijų. S 2p spektre po HER (3.29. pav. d; žr. 78 p.) stebimas tik vienas dubletas, kurio  $2p_{3/2}$  ir  $2p_{1/2}$  komponentų ryšio energija nustatyta atitinkamai ties 161.4 eV ir 162.6 eV. Apskaičiuotas S/Mo santykis po HER buvo 1.85, tuo tarpu neapdoroto MoS<sub>2</sub>/Cisteino elektrodo S/Mo santykis yra 2.05.

XPS ir XRD analizės metu gauti duomenys leidžia manyti, jog hidroterminės molibdeno disulfido sintezės metu formuojasi atsitiktinai orientuota sluoksninė struktūra, kurios briaunose gali būti netipinė Mo ir S atomų konfigūracija, panašiai kaip ir Joensen *et al.* aprašyto Li eksfoliuoto MoS<sub>2</sub> atveju [190]. Stebimas HER greičio padidėjimas po anodinio apdorojimo koreliuoja su tiltelinių S<sub>2</sub><sup>2-</sup> ir viršūninės S<sup>2-</sup> grupių santykinio kieko padidėjimu, užfiksuotu XPS. Anodinio MoS<sub>2</sub> apdorojimo metu gali vykti dvi tikėtinės oksidacijos reakcijos:



Pirmosios reakcijos (2 lygtis) metu S<sup>2-</sup> oksiduoja iki sulfato jonų, taip sumažinant bendrą sieros kiekį ant elektrodo paviršiaus. Antroji reakcija (3 lygtis) parodo tiltelinių S<sub>2</sub><sup>2-</sup> grupių susiformavimo būdą, o šios yra aktyvios HER ir tai paaiškintų stebimą HER greičio padidėjimą po anodinio apdorojimo. Po ilgalaikio katodinio apdorojimo stebimas elektrodo aktyvumo kritimas koreliuoja su šių grupių kieko sumažėjimu (3.29. pav. b; žr. 78 p.). XRD matomi struktūriniai pokyčiai (3.28. pav. 1,2; žr. 77 p.), bei XPS matoma galima Mo oksidacijos laipsnio pokyčio tendencija (3.29. pav. ; žr. 78 p.) leidžia manyti, jog HER metu galimi katalitiškai aktyvios MoS<sub>2</sub> pozicijos cheminiai pokyčiai. Nepaisant to, tiltelinės S<sub>2</sub><sup>2-</sup> ir viršūninės S<sup>2-</sup> grupės nėra vienintelės aktyviosios HER pozicijos [191] ir jų pašalinimas nepadaro MoS<sub>2</sub> neveiksniu vandenilio išskyrimo reakcijos elektrokatalizatoriumi [192].

## IŠVADOS

- Hidroterminės sintezės metu susiformuoja nanolapelinės molibdeno disulfido struktūros, kurių paviršiaus morfologija nepriklauso nuo papildomai pridėtų aminorūgščių bei jų koncentracijos, o storis priklauso nuo sintezės laiko.
- Suformuotos  $\text{MoS}_2$  dangos su aminorūgštimis pasižymi didesniu nei būdingas gamtiniam  $2\text{H}\text{-}\text{MoS}_2$  tarpplokštuminiu atstumu. Tarpplokštuminis atstumas padidėja dėl krūvį turinčių amino rūgščių skilimo fragmentų įsiterpimo į  $\text{MoS}_2$  tarpsluoksnius.
- $\text{MoS}_2$  dangose, susintetintose su aminorūgštimis, nustatyta padidėjęs metastabilių  $1\text{T}\text{-}\text{MoS}_2$  fazės kiekis, lyginant su  $\text{MoS}_2$  dangomis suformuotomis be aminorūgščių.
- Įsiterpę aminorūgščių fragmentai stabilizuojant metastabilą  $1\text{T}$  fazę, tuo padidindami šių elektrodų stabiliumą.
- Santykinai didelis  $1\text{T}\text{-}\text{MoS}_2$  fazės kiekis nulemia didesnį suformuotų  $\text{MoS}_2$ /aminorūgščių elektrodų vandenilio išskyrimo reakcijos greitį.
- Po anodinio  $\text{MoS}_2$  apdorojimo nustatyta vandenilio išskyrimo reakcijos greičio padidėjimas sietinas su tiltelinėms  $\text{S}_2^{2-}$  ir viršūninėms  $\text{S}^{2-}$  grupėms priskirtinos sieros kiekiu padidėjimu.
- $\text{MoS}_2$  paveikus trumpu anodiniu impulsu, elektrodo aktyvumas padidėja iki 30%, todėl anodinis apdorojimas gali būti naudojamas vandenilio išskyrimo reakcijai skirtų hidrotermiškai susintetinto molibdeno disulfido elektrodų aktyvumo padidinimui.

## CURRICULUM VITAE

Name	PAULIUS GAIGALAS
Date of birth	1994 06 08
Address	Taikos g. 177-10, Vilnius, Lithuania
Phone No.	+37060009832
E-mail	gaigalas.paulius@gmail.com

### EDUCATION:

- **2013 m. – 2017 m.**

Vilnius University

Bachelor's degree in Chemistry

- **2017 m. – 2019 m.**

Vilnius University

Master's degree in Physical Sciences

- **2019 m. –**

Center for Physical Sciences and Technology

Doctoral degree in Chemistry

### TRAINEESHIPS:

**2016-09 – 2016-11** Erasmus+ traineeship, European Institute of Membranes, Montpellier, France

**2022-10 – 2022-11** XPS Traineeship at Chimie des Interactions Plasma-Surface laboratory (ChIPS), University of Mons, Mons, Belgium

## LIST OF PUBLICATIONS

### Publications for doctoral dissertation

1. A. Naujokaitis, **P. Gaigalas**, C. Bittencourt, S. Mickevičius, A. Jagminas, 1T/2H MoS<sub>2</sub>/MoO<sub>3</sub> hybrid assembles with glycine as highly efficient and stable electrocatalyst for water splitting, International Journal of Hydrogen Energy 44(44) (2019) 24237-24245. DOI:10.1016/j.ijhydene.2019.07.161
2. A. Jagminas, **P. Gaigalas**, C. Bittencourt, V. Klimas, Cysteine-Induced Hybridization of 2D Molybdenum Disulfide Films for Efficient and Stable Hydrogen Evolution Reaction, Materials 14 (2021) 1165. DOI:10.3390/ma14051165
3. **P. Gaigalas**, T. Sabirovas, I. Matulaitienė, A. Jagminas, Impact of histidine amino acid on 2D molybdenum disulfide catalytic properties for hydrogen evolution reaction, Journal of Applied Electrochemistry 53 (2023) 85-94. DOI: 10.1007/s10800-022-01762-2

### Other publications

1. T. Ma, **P. Gaigalas**, M. Lepoitevin, I. Plikusienė, M. Bechelany, J.M. Janot, E. Balanzat, S. Balme, Impact of Polyelectrolyte Multilayers on the Ionic Current Rectification of Conical Nanopores, Langmuir 34 (2018) 3405-3412. DOI: 10.1021/acs.langmuir.8b00222
2. A. Jagminas, A. Naujokaitis, **P. Gaigalas**, S. Ramanavičius, M. Kurtinaitienė, R. Trusovas, Substrate Impact on the Structure and Electrocatalyst Properties of Molybdenum Disulfide for HER from Water. Metals 10(9) (2020) 1251. DOI: 10.3390/met10091251

### Conference reports

1. **P. Gaigalas**, V. Klimas, A. Jagminas, Impact of L-cysteine on the composition and electrocatalytic properties of MoS<sub>2</sub> films, 64<sup>th</sup> International conference for students of Physics and Natural Sciences „Open Readings 2021“, Saulėtekio al. 3, LT-10257, Vilnius, 2021 (Oral presentation).
2. **P. Gaigalas**, A. Jagminas, Impact of amino acids on the electrocatalytic properties of MoS<sub>2</sub> films, 23<sup>rd</sup> International conference-school „Advanced

Materials and Technologies 2021“, Vytauto g. 40, Palanga, 2021 (Poster presentation).

3. **P. Gaigalas**, A. Jagminas, V. Klimas, Cisteinu hibridizuotų molibdeno disulfido dangų sintezė ir elektrokatalizinio aktyvumo tyrimas, 11-oji Fizinių ir technologijos mokslų centro doktorantų ir jaunųjų mokslininkų konferencija „FizTeCh 2021“, Saulėtekio al. 3, LT-10257, Vilnius, 2021 (Oral presentation).
4. **P. Gaigalas**, A. Jagminas, Intercalation of Histidine into Molybdenum Disulfide Films for Efficient Hydrogen Evolution Reaction, 65<sup>th</sup> International conference for students of Physics and Natural Sciences „Open Readings 2022“, Saulėtekio al. 3, LT-10257, Vilnius, 2022 (Poster presentation).
5. **P. Gaigalas**, Histidino įtaka molibdeno disulfido elektrokataliziniam aktyvumui vandenilio išskyrimo reakcijoje, 12-oji Fizinių ir technologijos mokslų centro doktorantų ir jaunųjų mokslininkų konferencija „FizTeCh 2022“, Saulėtekio al. 3, LT-10257, Vilnius, 2022 (Oral presentation).

## REFERENCES

- [1] A.G. Olabi, M.A. Abdelkareem, Renewable energy and climate change, *Renewable and Sustainable Energy Reviews* 158 (2022) 112111. <https://doi.org/10.1016/j.rser.2022.112111>
- [2] Y. Cao, Roadmap and Direction toward High-Performance MoS<sub>2</sub> Hydrogen Evolution Catalysts, *ACS Nano* 15(7) (2021) 11014-11039. <https://doi.org/10.1021/acsnano.1c01879>
- [3] L. Schlapbach, A. Züttel, Hydrogen-storage materials for mobile applications, *Nature* 414(6861) (2001) 353-358. <https://doi.org/10.1038/35104634>
- [4] M.S. Dresselhaus, I.L. Thomas, Alternative energy technologies, *Nature* 414(6861) (2001) 332-337. <https://doi.org/10.1038/35104599>
- [5] G. Marbán, T. Valdés-Solís, Towards the hydrogen economy?, *International Journal of Hydrogen Energy* 32(12) (2007) 1625-1637. <https://doi.org/10.1016/j.ijhydene.2006.12.017>
- [6] J. Tang, J. Huang, D. Ding, S. Zhang, X. Deng, Research progress of 1T-MoS<sub>2</sub> in electrocatalytic hydrogen evolution, *International Journal of Hydrogen Energy* 47(94) (2022) 39771-39795. <https://doi.org/10.1016/j.ijhydene.2022.09.162>
- [7] J.A. Turner, Sustainable Hydrogen Production, *Science* 305(5686) (2004) 972-974. <https://doi.org/10.1126/science.1103197>
- [8] A.J. Bard, M.A. Fox, Artificial Photosynthesis: Solar Splitting of Water to Hydrogen and Oxygen, *Accounts of Chemical Research* 28(3) (1995) 141-145. <https://doi.org/10.1021/ar00051a007>
- [9] P.P. Edwards, V.L. Kuznetsov, W.I.F. David, N.P. Brandon, Hydrogen and fuel cells: Towards a sustainable energy future, *Energy Policy* 36(12) (2008) 4356-4362. <https://doi.org/10.1016/j.enpol.2008.09.036>
- [10] M.A. Abbas, J.H. Bang, Rising Again: Opportunities and Challenges for Platinum-Free Electrocatalysts, *Chemistry of Materials* 27(21) (2015) 7218-7235. <https://doi.org/10.1021/acs.chemmater.5b03331>
- [11] B. Huang, Y. Zhao, Iridium-based electrocatalysts toward sustainable energy conversion, *EcoMat* 4(2) (2022) e12176. <https://doi.org/10.1002/eom2.12176>
- [12] S.W. Lee, C. Carlton, M. Risch, Y. Surendranath, S. Chen, S. Furutsuki, A. Yamada, D.G. Nocera, Y. Shao-Horn, The Nature of Lithium Battery Materials under Oxygen Evolution Reaction Conditions, *Journal of the American Chemical Society* 134(41) (2012) 16959-16962. <https://doi.org/10.1021/ja307814j>
- [13] G.S. Hutchings, Y. Zhang, J. Li, B.T. Yonemoto, X. Zhou, K. Zhu, F. Jiao, In Situ Formation of Cobalt Oxide Nanocubanes as Efficient Oxygen Evolution Catalysts, *Journal of the American Chemical Society* 137(12) (2015) 4223-4229. <https://doi.org/10.1021/jacs.5b01006>
- [14] M.S. Burke, L.J. Enman, A.S. Batchellor, S. Zou, S.W. Boettcher, Oxygen Evolution Reaction Electrocatalysis on Transition Metal Oxides and (Oxy)hydroxides: Activity Trends and Design Principles, *Chemistry of Materials* 27(22) (2015) 7549-7558. <https://doi.org/10.1021/acs.chemmater.5b03148>
- [15] J.-I. Jung, H.Y. Jeong, J.-s. Lee, M.G. Kim, J. Cho, A Bifunctional Perovskite Catalyst for Oxygen Reduction and Evolution, *Angewandte Chemie (International ed. in English)* 53(18) (2014) 4582-4586. <https://doi.org/10.1002/anie.201311223>
- [16] Y. Liu, H. Cheng, M. Lyu, S. Fan, Q. Liu, W. Zhang, Y. Zhi, C. Wang, C. Xiao, S. Wei, B. Ye, Y. Xie, Low Overpotential in Vacancy-Rich Ultrathin CoSe<sub>2</sub> Nanosheets for Water Oxidation, *Journal of the American Chemical Society* 136(44) (2014) 15670-15675. <https://doi.org/10.1021/ja5085157>

- [17] S.A. Patil, E.-K. Kim, N.K. Shrestha, J. Chang, J.K. Lee, S.-H. Han, Formation of Semimetallic Cobalt Telluride Nanotube Film via Anion Exchange Tellurization Strategy in Aqueous Solution for Electrocatalytic Applications, *ACS Applied Materials & Interfaces* 7(46) (2015) 25914-25922. <https://doi.org/10.1021/acsami.5b08501>
- [18] J.F. Callejas, C.G. Read, C.W. Roske, N.S. Lewis, R.E. Schaak, Synthesis, Characterization, and Properties of Metal Phosphide Catalysts for the Hydrogen-Evolution Reaction, *Chemistry of Materials* 28(17) (2016) 6017-6044. <https://doi.org/10.1021/acs.chemmater.6b02148>
- [19] Y. Zhong, X. Xia, F. Shi, J. Zhan, J. Tu, H. Fan, Transition Metal Carbides and Nitrides in Energy Storage and Conversion, *Advanced Science* 3(5) (2017) 1500286. <https://doi.org/10.1002/advs.201500286>
- [20] J. Xie, Y. Xie, Transition Metal Nitrides for Electrocatalytic Energy Conversion: Opportunities and Challenges, *Chemistry - A European Journal* 22(11) (2015) 3588-3598. <https://doi.org/10.1002/chem.201501120>
- [21] F. Wang, T.A. Shifa, X. Zhan, Y. Huang, K. Liu, Z. Cheng, C. Jiang, J. He, Recent advances in transition-metal dichalcogenide based nanomaterials for water splitting, *Nanoscale* 7(47) (2015) 19764-19788. <https://doi.org/10.1039/C5NR06718A>
- [22] A.B. Laursen, S. Kegnæs, S. Dahl, I. Chorkendorff, Molybdenum sulfides—efficient and viable materials for electro - and photoelectrocatalytic hydrogen evolution, *Energy & Environmental Science* 5(2) (2012) 5577-5591. <https://doi.org/10.1039/c2ee02618j>
- [23] X. Huang, Z. Zeng, H. Zhang, Metal dichalcogenide nanosheets: preparation, properties and applications, *Chemical Society Reviews* 42(5) (2013) 1934-1946. <https://doi.org/10.1039/C2CS35387C>
- [24] R. Kappera, D. Voiry, S.E. Yalcin, B. Branch, G. Gupta, A.D. Mohite, M. Chhowalla, Phase-engineered low-resistance contacts for ultrathin MoS<sub>2</sub> transistors, *Nature Materials* 13(12) (2014) 1128-1134. <https://doi.org/10.1038/nmat4080>
- [25] B. Hinnemann, P.G. Moses, J. Bonde, K.P. Jørgensen, J.H. Nielsen, S. Horch, I. Chorkendorff, J.K. Nørskov, Biomimetic Hydrogen Evolution: MoS<sub>2</sub> Nanoparticles as Catalyst for Hydrogen Evolution, *Journal of the American Chemical Society* 127(15) (2005) 5308-5309. <https://doi.org/10.1021/ja0504690>
- [26] B. Radisavljevic, A. Radenovic, J. Brivio, V. Giacometti, A. Kis, Single-layer MoS<sub>2</sub> transistors, *Nature Nanotechnology* 6(3) (2011) 147-150. <https://doi.org/10.1038/nnano.2010.279>
- [27] M. Chhowalla, H.S. Shin, G. Eda, L.-J. Li, K.P. Loh, H. Zhang, The chemistry of two-dimensional layered transition metal dichalcogenide nanosheets, *Nature Chemistry* 5(4) (2013) 263-275. <https://doi.org/10.1038/nchem.1589>
- [28] A. Zak, Y. Feldman, V. Lyakhovitskaya, G. Leitus, R. Popovitz-Biro, E. Wachtel, H. Cohen, S. Reich, R. Tenne, Alkali Metal Intercalated Fullerene-Like MS<sub>2</sub> (M = W, Mo) Nanoparticles and Their Properties, *Journal of the American Chemical Society* 124(17) (2002) 4747-4758. <https://doi.org/10.1021/ja012060q>
- [29] B. King, Minerals explained 39: Molybdenite, *Geology Today* 20(1) (2004) 34-37. <https://doi.org/10.1111/j.1365-2451.2004.00444.x>
- [30] J.A. Wilson, A.D. Yoffe, The transition metal dichalcogenides discussion and interpretation of the observed optical, electrical and structural properties, *Advances in Physics* 18(73) (1969) 193-335. <https://doi.org/10.1080/00018736900101307>
- [31] T. Böker, R. Severin, A. Müller, C. Janowitz, R. Manzke, D. Voß, P. Krüger, A. Mazur, J. Pollmann, Band structure of MoS<sub>2</sub>, MoSe<sub>2</sub>, and  $\alpha$ -MoTe<sub>2</sub>: Angle-resolved

- photoelectron spectroscopy and ab initio calculations, *Physical Review B* 64(23) (2001) 235305. <https://doi.org/10.1103/PhysRevB.64.235305>
- [32] K.F. Mak, C. Lee, J. Hone, J. Shan, T.F. Heinz, Atomically Thin MoS<sub>2</sub> : A New Direct-Gap Semiconductor, *Physical Review Letters* 105(13) (2010) 136805. <https://doi.org/10.1103/PhysRevLett.105.136805>
- [33] F. Wypych, R. Schöllhorn, 1T-MoS<sub>2</sub>, a new metallic modification of molybdenum disulfide, *Journal of the Chemical Society, Chemical Communications* (19) (1992) 1386-1388. <https://doi.org/10.1039/C39920001386>
- [34] L.F. Mattheiss, Energy Bands for 2H-NbSe<sub>2</sub> and 2H-MoS<sub>2</sub>, *Physical Review Letters* 30(17) (1973) 784-787. <https://doi.org/10.1103/PhysRevLett.30.784>
- [35] U. Maitra, U. Gupta, M. De, R. Datta, A. Govindaraj, C.N.R. Rao, Highly Effective Visible-Light-Induced H<sub>2</sub> Generation by Single-Layer 1T-MoS<sub>2</sub> and a Nanocomposite of Few-Layer 2H-MoS<sub>2</sub> with Heavily Nitrogenated Graphene, *Angewandte Chemie International Edition* 52(49) (2013) 13057-13061. <https://doi.org/10.1002/anie.201306918>
- [36] M. Acerce, D. Voiry, M. Chhowalla, Metallic 1T phase MoS<sub>2</sub> nanosheets as supercapacitor electrode materials, *Nature Nanotechnology* 10(4) (2015) 313-318. <https://doi.org/10.1038/nnano.2015.40>
- [37] K.E. Dungey, M.D. Curtis, J.E. Penner-Hahn, Structural Characterization and Thermal Stability of MoS<sub>2</sub> Intercalation Compounds, *Chemistry of Materials* 10(8) (1998) 2152-2161. <https://doi.org/10.1021/cm980034u>
- [38] J. Heising, M.G. Kanatzidis, Exfoliated and Restacked MoS<sub>2</sub> and WS<sub>2</sub>: Ionic or Neutral Species? Encapsulation and Ordering of Hard Electropositive Cations, *Journal of the American Chemical Society* 121(50) (1999) 11720-11732. <https://doi.org/10.1021/ja991644d>
- [39] G. Eda, H. Yamaguchi, D. Voiry, T. Fujita, M. Chen, M. Chhowalla, Photoluminescence from Chemically Exfoliated MoS<sub>2</sub>, *Nano Letters* 11(12) (2011) 5111-5116. <https://doi.org/10.1021/nl201874w>
- [40] J. Strachan, A.F. Masters, T. Maschmeyer, 3R-MoS<sub>2</sub> in Review: History, Status, and Outlook, *ACS Applied Energy Materials* 4(8) (2021) 7405-7418. <https://doi.org/10.1021/acsaem.1c00638>
- [41] M. Py, R.R. Haering, Structural destabilization induced by lithium intercalation in MoS<sub>2</sub> and related compounds, *Canadian Journal of Physics* 61 (1983) 76-84. <https://doi.org/10.1139/P83-013>
- [42] L. Cai, J. He, Q. Liu, T. Yao, L. Chen, W. Yan, F. Hu, Y. Jiang, Y. Zhao, T. Hu, Z. Sun, S. Wei, Vacancy-Induced Ferromagnetism of MoS<sub>2</sub> Nanosheets, *Journal of the American Chemical Society* 137(7) (2015) 2622-2627. <https://doi.org/10.1021/ja5120908>
- [43] G. Gao, Y. Jiao, F. Ma, Y. Jiao, E. Waclawik, A. Du, Charge Mediated Semiconducting-to-Metallic Phase Transition in Molybdenum Disulfide Monolayer and Hydrogen Evolution Reaction in New 1T' Phase, *The Journal of Physical Chemistry C* 119(23) (2015) 13124-13128. <https://doi.org/10.1021/acs.jpcc.5b04658>
- [44] K.-A.N. Duerloo, Y. Li, E.J. Reed, Structural phase transitions in two-dimensional Mo- and W-dichalcogenide monolayers, *Nature Communications* 5(1) (2014) 4214. <https://doi.org/10.1038/ncomms5214>
- [45] G. Eda, T. Fujita, H. Yamaguchi, D. Voiry, M. Chen, M. Chhowalla, Coherent Atomic and Electronic Heterostructures of Single-Layer MoS<sub>2</sub>, *ACS Nano* 6(8) (2012) 7311-7317. <https://doi.org/10.1021/nn302422x>

- [46] Q. Jin, N. Liu, B. Chen, D. Mei, Mechanisms of Semiconducting 2H to Metallic 1T Phase Transition in Two-dimensional MoS<sub>2</sub> Nanosheets, *The Journal of Physical Chemistry C* 122(49) (2018) 28215-28224. <https://doi.org/10.1021/acs.jpcc.8b10256>
- [47] C. Guo, H. Li, W. Zhao, J. Pan, T. Lin, J. Xu, M. Chen, F. Huang, High-quality single-layer nanosheets of MS<sub>2</sub> (M = Mo, Nb, Ta, Ti) directly exfoliated from AMS<sub>2</sub> (A = Li, Na, K) crystals, *Journal of Materials Chemistry C* 5(24) (2017) 5977-5983. <https://doi.org/10.1039/C7TC00838D>
- [48] B. Pal, A. Singh, S. G. P. Mahale, A. Kumar, S. Thirupathaiah, H. Sezen, M. Amati, L. Gregoratti, U.V. Waghmare, D.D. Sarma, Chemically exfoliated MoS<sub>2</sub> layers: Spectroscopic evidence for the semiconducting nature of the dominant trigonal metastable phase, *Physical Review B* 96(19) (2017) 195426. <https://doi.org/10.1103/PhysRevB.96.195426>
- [49] W.O. Winer, Molybdenum disulfide as a lubricant: A review of the fundamental knowledge, *Wear* 10(6) (1967) 422-452. [https://doi.org/10.1016/0043-1648\(67\)90187-1](https://doi.org/10.1016/0043-1648(67)90187-1)
- [50] J.P. Oviedo, S. Kc, N. Lu, J. Wang, K. Cho, R.M. Wallace, M.J. Kim, In Situ TEM Characterization of Shear-Stress-Induced Interlayer Sliding in the Cross Section View of Molybdenum Disulfide, *ACS Nano* 9(2) (2015) 1543-1551. <https://doi.org/10.1021/nn506052d>
- [51] H.G.M. Fischer, R.P. Russell, Treatment of motor fuels, U.S. Patent and Trademark Office (1943) US2322622A. <https://patents.google.com/patent/US2322622A/en>
- [52] M.-L. Tsai, S.-H. Su, J.-K. Chang, D.-S. Tsai, C.-H. Chen, C.-I. Wu, L.-J. Li, L.-J. Chen, J.-H. He, Monolayer MoS<sub>2</sub> Heterojunction Solar Cells, *ACS Nano* 8(8) (2014) 8317-8322. <https://doi.org/10.1021/nn502776h>
- [53] T. Stephenson, Z. Li, B. Olsen, D. Mitlin, Lithium ion battery applications of molybdenum disulfide (MoS<sub>2</sub>) nanocomposites, *Energy & Environmental Science* 7(1) (2014) 209-231. <https://doi.org/10.1039/C3EE42591F>
- [54] D.J. Late, Y.-K. Huang, B. Liu, J. Acharya, S.N. Shirodkar, J. Luo, A. Yan, D. Charles, U.V. Waghmare, V.P. Dravid, C.N.R. Rao, Sensing Behavior of Atomically Thin-Layered MoS<sub>2</sub> Transistors, *ACS Nano* 7(6) (2013) 4879-4891. <https://doi.org/10.1021/nn400026u>
- [55] S. Desai, S. Madhvapathy, A. Sachid, J. Llinas, Q. Wang, G. Ahn, G. Pitner, M. Kim, J. Bokor, C. hu, H.S.P. Wong, A. Javey, MoS<sub>2</sub> transistors with 1-nanometer gate lengths, *Science* 354 (2016) 99-102. <https://doi.org/10.1126/science.aah4698>
- [56] J. Pu, Y. Yomogida, K.-K. Liu, L.-J. Li, Y. Iwasa, T. Takenobu, Highly Flexible MoS<sub>2</sub> Thin-Film Transistors with Ion Gel Dielectrics, *Nano Letters* 12(8) (2012) 4013-4017. <https://doi.org/10.1021/nl301335q>
- [57] J. Shi, P. Yu, F. Liu, P. He, R. Wang, L. Qin, J. Zhou, X. Li, J. Zhou, X. Sui, S. Zhang, Y. Zhang, Q. Zhang, T.C. Sum, X. Qiu, Z. Liu, X. Liu, 3R MoS<sub>2</sub> with Broken Inversion Symmetry: A Promising Ultrathin Nonlinear Optical Device, *Advanced Materials* 29(30) (2017) 1701486. <https://doi.org/10.1002/adma.201701486>
- [58] I. Marriam, M. Tebyetekerwa, H. Chen, H. Chathuranga, N. Motta, J.A. Alarco, Z.-J. He, J.-C. Zheng, A. Du, C. Yan, Few-layer MoS<sub>2</sub> nanosheets with and without silicon nanoparticles as anodes for lithium-ion batteries, *Journal of Materials Chemistry A* 11(6) (2023) 2670-2678. <https://doi.org/10.1039/D2TA08886J>
- [59] N.H. Attanayake, A.C. Thenuwara, A. Patra, Y.V. Aulin, T.M. Tran, H. Chakraborty, E. Borguet, M.L. Klein, J.P. Perdew, D.R. Strongin, Effect of Intercalated Metals on the Electrocatalytic Activity of 1T-MoS<sub>2</sub> for the Hydrogen

Evolution Reaction, ACS Energy Letters 3(1) (2018) 7-13.  
<https://doi.org/10.1021/acsenergylett.7b00865>

[60] A.P. Singh, S. Balayan, S. Gupta, U. Jain, R.K. Sarin, N. Chauhan, Detection of pesticide residues utilizing enzyme-electrode interface via nano-patterning of TiO<sub>2</sub> nanoparticles and molybdenum disulfide (MoS<sub>2</sub>) nanosheets, *Process Biochemistry* 108 (2021) 185-193. <https://doi.org/10.1016/j.procbio.2021.06.015>

[61] X. Zhao, S. Ning, W. Fu, S.J. Pennycook, K.P. Loh, Differentiating Polymorphs in Molybdenum Disulfide via Electron Microscopy, *Advanced Materials* 30(47) (2018) 1802397. <https://doi.org/10.1002/adma.201802397>

[62] Y. Qi, Q. Xu, Y. Wang, B. Yan, Y. Ren, Z. Chen, CO<sub>2</sub>-Induced Phase Engineering: Protocol for Enhanced Photoelectrocatalytic Performance of 2D MoS<sub>2</sub> Nanosheets, *ACS Nano* 10(2) (2016) 2903-2909.  
<https://doi.org/10.1021/acsnano.6b00001>

[63] R. Naz, M. Imtiaz, Q. Liu, L. Yao, W. Abbas, T. Li, I. Zada, Y. Yuan, W. Chen, J. Gu, Highly defective 1T-MoS<sub>2</sub> nanosheets on 3D reduced graphene oxide networks for supercapacitors, *Carbon* 152 (2019) 697-703.  
<https://doi.org/10.1016/j.carbon.2019.06.009>

[64] S. Palsaniya, H.B. Nemade, A.K. Dasmahapatra, Synthesis of polyaniline/graphene/MoS<sub>2</sub> nanocomposite for high performance supercapacitor electrode, *Polymer* 150 (2018) 150-158.  
<https://doi.org/10.1016/j.polymer.2018.07.018>

[65] X. Du, J. Huang, X. Guo, X. Lin, J.-Q. Huang, H. Tan, Y. Zhu, B. Zhang, Preserved Layered Structure Enables Stable Cyclic Performance of MoS<sub>2</sub> upon Potassium Insertion, *Chemistry of Materials* 31(21) (2019) 8801-8809.  
<https://doi.org/10.1021/acs.chemmater.9b02678>

[66] X. Geng, W. Sun, W. Wu, B. Chen, A. Al-Hilo, M. Benamara, H. Zhu, F. Watanabe, J. Cui, T.-p. Chen, Pure and stable metallic phase molybdenum disulfide nanosheets for hydrogen evolution reaction, *Nature Communications* 7(1) (2016) 10672. <https://doi.org/10.1038/ncomms10672>

[67] J. Zheng, H. Zhang, S. Dong, Y. Liu, C. Tai Nai, H. Suk Shin, H. Young Jeong, B. Liu, K. Ping Loh, High yield exfoliation of two-dimensional chalcogenides using sodium naphthalenide, *Nature Communications* 5(1) (2014) 2995.  
<https://doi.org/10.1038/ncomms3995>

[68] C.A. Papageorgopoulos, W. Jaegermann, Li intercalation across and along the van der Waals surfaces of MoS<sub>2</sub>(0001), *Surface Science* 338(1) (1995) 83-93.  
[https://doi.org/10.1016/0039-6028\(95\)00544-7](https://doi.org/10.1016/0039-6028(95)00544-7)

[69] D. Ganta, S. Sinha, R.T. Haasch, 2-D material molybdenum disulfide analyzed by XPS, *Surface Science Spectra* 21(1) (2014) 19-27.  
<https://doi.org/10.1116/11.20140401>

[70] C. Guo, J. Pan, H. Li, T. Lin, P. Liu, C. Song, D. Wang, G. Mu, X. Lai, H. Zhang, W. Zhou, M. Chen, F. Huang, Observation of superconductivity in 1T'-MoS<sub>2</sub> nanosheets, *Journal of Materials Chemistry C* 5(41) (2017) 10855-10860.  
<https://doi.org/10.1039/C7TC03749J>

[71] M. Krbal, J. Prikryl, I. Pis, V. Prokop, J. Rodriguez Pereira, A.V. Kolobov, Anomalous electrical conductivity change in MoS<sub>2</sub> during the transition from the amorphous to crystalline phase, *Ceramics International* 49(2) (2023) 2619-2625.  
<https://doi.org/10.1016/j.ceramint.2022.09.242>

[72] T. Fleisch, G. Mains, An XPS study of the UV reduction and photochromism of MoO<sub>3</sub> and WO<sub>3</sub>, *The Journal of Chemical Physics* 76(2) (1982) 780-786.  
<https://doi.org/10.1063/1.443047>

- [73] C.-H. Lin, C.-H. Tsai, F.-G. Tseng, Y.-Y. Yu, H.-C. Wu, C.-K. Hsieh, Low-Temperature Thermally Reduced Molybdenum Disulfide as a Pt-Free Counter Electrode for Dye-Sensitized Solar Cells, *Nanoscale Research Letters* 10(1) (2015) 446. <https://doi.org/10.1186/s11671-015-1156-0>
- [74] A.D. Gandubert, C. Legens, D. Guillaume, E. Payen, X-ray photoelectron spectroscopy surface quantification of sulfided CoMoP catalysts. Relation between activity and promoted sites. Part II: Influence of the sulfidation temperature, *Surface and Interface Analysis* 38(4) (2006) 206-209. <https://doi.org/10.1002/sia.2249>
- [75] D. Voiry, M. Salehi, R. Silva, T. Fujita, M. Chen, T. Asefa, V.B. Shenoy, G. Eda, M. Chhowalla, Conducting MoS<sub>2</sub> Nanosheets as Catalysts for Hydrogen Evolution Reaction, *Nano Letters* 13(12) (2013) 6222-6227. <https://doi.org/10.1021/nl403661s>
- [76] H. Li, Q. Zhang, C.C.R. Yap, B.K. Tay, T.H.T. Edwin, A. Olivier, D. Baillargeat, From Bulk to Monolayer MoS<sub>2</sub>: Evolution of Raman Scattering, *Advanced Functional Materials* 22(7) (2012) 1385-1390. <https://doi.org/10.1002/adfm.201102111>
- [77] M. Placidi, M. Dimitrieva, V. Izquierdo-Roca, X. Fontané, A. Castellanos-Gomez, A. Pérez-Tomás, N. Mestres, M. Espindola-Rodríguez, S. López-Marino, M. Neuschitzer, V. Bermudez, A. Yaremko, A. Pérez-Rodríguez, Multiwavelength excitation Raman scattering analysis of bulk and two-dimensional MoS<sub>2</sub>: vibrational properties of atomically thin MoS<sub>2</sub> layers, *2D Materials* 2(3) (2015) 035006. <https://doi.org/10.1088/2053-1583/2/3/035006>
- [78] L. Yang, X. Cui, J. Zhang, K. Wang, M. Shen, S. Zeng, S.A. Dayeh, L. Feng, B. Xiang, Lattice strain effects on the optical properties of MoS<sub>2</sub> nanosheets, *Scientific Reports* 4(1) (2014) 5649. <https://doi.org/10.1038/srep05649>
- [79] M.A. Lukowski, A.S. Daniel, F. Meng, A. Forticaux, L. Li, S. Jin, Enhanced Hydrogen Evolution Catalysis from Chemically Exfoliated Metallic MoS<sub>2</sub> Nanosheets, *Journal of the American Chemical Society* 135(28) (2013) 10274-10277. <https://doi.org/10.1021/ja404523s>
- [80] S. Jiménez Sandoval, D. Yang, R.F. Frindt, J.C. Irwin, Raman study and lattice dynamics of single molecular layers of MoS<sub>2</sub>, *Physical Review B* 44(8) (1991) 3955-3962. <https://doi.org/10.1103/PhysRevB.44.3955>
- [81] L. Zhang, D. Sun, J. Kang, J. Feng, H.A. Bechtel, L.-W. Wang, E.J. Cairns, J. Guo, Electrochemical Reaction Mechanism of the MoS<sub>2</sub> Electrode in a Lithium-Ion Cell Revealed by in Situ and Operando X-ray Absorption Spectroscopy, *Nano Letters* 18(2) (2018) 1466-1475. <https://doi.org/10.1021/acs.nanolett.7b05246>
- [82] L. Seguin, M. Figlarz, R. Cavagnat, J.C. Lassègues, Infrared and Raman spectra of MoO<sub>3</sub> molybdenum trioxides and MoO<sub>3</sub> · xH<sub>2</sub>O molybdenum trioxide hydrates, *Spectrochimica Acta Part A: Molecular and Biomolecular Spectroscopy* 51(8) (1995) 1323-1344. [https://doi.org/10.1016/0584-8539\(94\)00247-9](https://doi.org/10.1016/0584-8539(94)00247-9)
- [83] A.D. Marinov, L. Bravo Priegue, A.R. Shah, T.S. Miller, C.A. Howard, G. Hinds, P.R. Shearing, P.L. Cullen, D.J.L. Brett, Ex Situ Characterization of 1T/2H MoS<sub>2</sub> and Their Carbon Composites for Energy Applications, a Review, *ACS Nano* 17(6) (2023) 5163-5186. <https://doi.org/10.1021/acsnano.2c08913>
- [84] J. Zhu, Z. Wang, H. Yu, N. Li, J. Zhang, J. Meng, M. Liao, J. Zhao, X. Lu, L. Du, R. Yang, D. Shi, Y. Jiang, G. Zhang, Argon Plasma Induced Phase Transition in Monolayer MoS<sub>2</sub>, *Journal of the American Chemical Society* 139(30) (2017) 10216-10219. <https://doi.org/10.1021/jacs.7b05765>
- [85] B. Elvers, W. Gerhardt, S. Hawkins, W.E. Russey, H. Hofmann, G. Schulz, F. Ullmann, M. Pikart-Müller, H. Günzler, M. Polke, Ullmann's Encyclopedia of Industrial Chemistry: Magnetic Materials to Mutagenic Agents. Vol. A16, 1990. ISBN 13: 9780895731661

- [86] N. Baig, I. Kammakakam, W. Falath, Nanomaterials: a review of synthesis methods, properties, recent progress, and challenges, *Materials Advances* 2(6) (2021) 1821-1871. <https://doi.org/10.1039/D0MA00807A>
- [87] K.S. Novoselov, D. Jiang, F. Schedin, T. Booth, V.V. Khotkevich, S.V. Morozov, A.K. Geim, Two-Dimensional Atomic Crystals, *Proceedings of the National Academy of Sciences of the United States of America* 102 (2005) 10451-3. <https://doi.org/10.1073/pnas.0502848102>
- [88] H. Zhang, Ultrathin Two-Dimensional Nanomaterials, *ACS Nano* 9(10) (2015) 9451-9469. <https://doi.org/10.1021/acsnano.5b05040>
- [89] L. Ottaviano, S. Palleschi, F. Perrozzi, G. D'Olimpio, F. Priante, M. Donarelli, P. Benassi, M. Nardone, M. Gonchigsuren, M. Gombosuren, A. Lucia, G. Moccia, O.A. Cacioppo, Mechanical exfoliation and layer number identification of MoS<sub>2</sub> revisited, *2D Materials* 4(4) (2017) 045013. <https://doi.org/10.1088/2053-1583/aa8764>
- [90] M. Yi, Z. Shen, A review on mechanical exfoliation for the scalable production of graphene, *Journal of Materials Chemistry A* 3(22) (2015) 11700-11715. <https://doi.org/10.1039/C5TA00252D>
- [91] C.-X. Hu, Y. Shin, O. Read, C. Casiraghi, Dispersant-assisted liquid-phase exfoliation of 2D materials beyond graphene, *Nanoscale* 13(2) (2021) 460-484. <https://doi.org/10.1039/D0NR05514J>
- [92] T. Skaltsas, X. Ke, C. Bittencourt, N. Tagmatarchis, Ultrasonication Induces Oxygenated Species and Defects onto Exfoliated Graphene, *The Journal of Physical Chemistry C* 117(44) (2013) 23272-23278. <https://doi.org/10.1021/jp4057048>
- [93] F.I. Alzakia, S.C. Tan, Liquid-Exfoliated 2D Materials for Optoelectronic Applications, *Advanced Science* 8(11) (2021) 2003864. <https://doi.org/10.1002/advs.202003864>
- [94] L. Dong, S. Lin, L. Yang, J. Zhang, C. Yang, D. Yang, H. Lu, Spontaneous exfoliation and tailoring of MoS<sub>2</sub> in mixed solvents, *Chemical Communications* 50(100) (2014) 15936-15939. <https://doi.org/10.1039/C4CC07238C>
- [95] C. Backes, B.M. Szydłowska, A. Harvey, S. Yuan, V. Vega-Mayoral, B.R. Davies, P.-I. Zhao, D. Hanlon, E.J.G. Santos, M.I. Katsnelson, W.J. Blau, C. Gadermaier, J.N. Coleman, Production of Highly Monolayer Enriched Dispersions of Liquid-Exfoliated Nanosheets by Liquid Cascade Centrifugation, *ACS Nano* 10(1) (2016) 1589-1601. <https://doi.org/10.1021/acsnano.5b07228>
- [96] I.T. Bello, A.O. Oladipo, O. Adedokun, S.M. Dhlamini, Recent advances on the preparation and electrochemical analysis of MoS<sub>2</sub>-based materials for supercapacitor applications: A mini-review, *Materials Today Communications* 25 (2020) 101664. <https://doi.org/10.1016/j.mtcomm.2020.101664>
- [97] L. Niu, J.N. Coleman, H. Zhang, H. Shin, M. Chhowalla, Z. Zheng, Production of Two-Dimensional Nanomaterials via Liquid-Based Direct Exfoliation, *Small* 12(3) (2016) 272-293. <https://doi.org/10.1002/smll.201502207>
- [98] X. Zhao, X. Ma, J. Sun, D. Li, X. Yang, Enhanced Catalytic Activities of Surfactant-Assisted Exfoliated WS<sub>2</sub> Nanodots for Hydrogen Evolution, *ACS Nano* 10(2) (2016) 2159-2166. <https://doi.org/10.1021/acsnano.5b06653>
- [99] J. Kim, S. Kwon, D.-H. Cho, B. Kang, H. Kwon, Y. Kim, S.O. Park, G.Y. Jung, E. Shin, W.-G. Kim, H. Lee, G.H. Ryu, M. Choi, T.H. Kim, J. Oh, S. Park, S.K. Kwak, S.W. Yoon, D. Byun, Z. Lee, C. Lee, Direct exfoliation and dispersion of two-dimensional materials in pure water via temperature control, *Nature Communications* 6(1) (2015) 8294. <https://doi.org/10.1038/ncomms9294>

- [100] M. Bodík, A. Annušová, J. Hagara, M. Mičušík, M. Omastová, M. Kotlár, J. Chlpík, J. Cirák, H. Švajdlenková, M. Anguš, A.M. Roldán, P. Veis, M. Jergel, E. Majkova, P. Šiffalovič, An elevated concentration of MoS<sub>2</sub> lowers the efficacy of liquid-phase exfoliation and triggers the production of MoO<sub>x</sub> nanoparticles, *Physical Chemistry Chemical Physics* 21(23) (2019) 12396-12405. <https://doi.org/10.1039/C9CP01951K>
- [101] Á. Coogan, Y.K. Gun'ko, Solution-based “bottom-up” synthesis of group VI transition metal dichalcogenides and their applications, *Materials Advances* 2(1) (2021) 146-164. <https://doi.org/10.1039/DOMA00697A>
- [102] Y. Xu, H. Cao, Y. Xue, B. Li, W. Cai, Liquid-Phase Exfoliation of Graphene: An Overview on Exfoliation Media, Techniques, and Challenges, *Nanomaterials* 8(11) (2018) 942. <https://doi.org/10.3390/nano8110942>
- [103] K.R. Paton, E. Varrla, C. Backes, R.J. Smith, U. Khan, A. O'Neill, C. Boland, M. Lotya, O.M. Istrate, P. King, T. Higgins, S. Barwick, P. May, P. Puczkarski, I. Ahmed, M. Moebius, H. Pettersson, E. Long, J. Coelho, S.E. O'Brien, E.K. McGuire, B.M. Sanchez, G.S. Duesberg, N. McEvoy, T.J. Pennycook, C. Downing, A. Crossley, V. Nicolosi, J.N. Coleman, Scalable production of large quantities of defect-free few-layer graphene by shear exfoliation in liquids, *Nature Materials* 13(6) (2014) 624-630. <https://doi.org/10.1038/nmat3944>
- [104] X.L. Li, T.C. Li, S. Huang, J. Zhang, M.E. Pam, H.Y. Yang, Controllable Synthesis of Two-Dimensional Molybdenum Disulfide (MoS<sub>2</sub>) for Energy-Storage Applications, *ChemSusChem* 13(6) (2020) 1379-1391. <https://doi.org/10.1002/cssc.201902706>
- [105] P. Joensen, R.F. Frindt, S.R. Morrison, Single-layer MoS<sub>2</sub>, *Materials Research Bulletin* 21(4) (1986) 457-461. [https://doi.org/10.1016/0025-5408\(86\)90011-5](https://doi.org/10.1016/0025-5408(86)90011-5)
- [106] K. Chrissafis, M. Zamani, K. Kambas, J. Stoemenos, N.A. Economou, I. Samaras, C. Julien, Structural studies of MoS<sub>2</sub> intercalated by lithium, *Materials Science and Engineering: B* 3(1) (1989) 145-151. [https://doi.org/10.1016/0921-5107\(89\)90194-3](https://doi.org/10.1016/0921-5107(89)90194-3)
- [107] Y. Yin, J. Han, Y. Zhang, X. Zhang, P. Xu, Q. Yuan, L. Samad, X. Wang, Y. Wang, Z. Zhang, P. Zhang, X. Cao, B. Song, S. Jin, Contributions of Phase, Sulfur Vacancies, and Edges to the Hydrogen Evolution Reaction Catalytic Activity of Porous Molybdenum Disulfide Nanosheets, *Journal of the American Chemical Society* 138(25) (2016) 7965-7972. <https://doi.org/10.1021/jacs.6b03714>
- [108] Y. Zhan, Z. Liu, S. Najmaei, P.M. Ajayan, J. Lou, Large-Area Vapor-Phase Growth and Characterization of MoS<sub>2</sub> Atomic Layers on a SiO<sub>2</sub> Substrate, *Small* 8(7) (2012) 966-971. <https://doi.org/10.1002/smll.201102654>
- [109] Y.-H. Lee, X.-Q. Zhang, W. Zhang, M.-T. Chang, C.-T. Lin, K.-D. Chang, Y.-C. Yu, J.T.-W. Wang, C.-S. Chang, L.-J. Li, T.-W. Lin, Synthesis of Large-Area MoS<sub>2</sub> Atomic Layers with Chemical Vapor Deposition, *Advanced Materials* 24(17) (2012) 2320-2325. <https://doi.org/10.1002/adma.201104798>
- [110] Y. Shi, W. Zhou, A.-Y. Lu, W. Fang, Y.-H. Lee, A.L. Hsu, S.M. Kim, K.K. Kim, H.Y. Yang, L.-J. Li, J.-C. Idrobo, J. Kong, van der Waals Epitaxy of MoS<sub>2</sub> Layers Using Graphene As Growth Templates, *Nano Letters* 12(6) (2012) 2784-2791. <https://doi.org/10.1021/nl204562j>
- [111] C.-L. Hsu, Y.-H. Chang, T.-Y. Chen, C.-C. Tseng, K.-H. Wei, L.-J. Li, Enhancing the electrocatalytic water splitting efficiency for amorphous MoS<sub>x</sub>, *International Journal of Hydrogen Energy* 39(10) (2014) 4788-4793. <https://doi.org/10.1016/j.ijhydene.2014.01.090>

- [112] S. Vishwanath, X. Liu, S. Rouvimov, P.C. Mende, A. Azcatl, S. McDonnell, R.M. Wallace, R.M. Feenstra, J.K. Furdyna, D. Jena, H. Grace Xing, Comprehensive structural and optical characterization of MBE grown MoSe<sub>2</sub> on graphite, CaF<sub>2</sub> and graphene, *2D Materials* 2(2) (2015) 024007. <https://doi.org/10.1088/2053-1583/2/2/024007>
- [113] J. Tao, J. Chai, X. Lu, L.M. Wong, T.I. Wong, J. Pan, Q. Xiong, D. Chi, S. Wang, Growth of wafer-scale MoS<sub>2</sub> monolayer by magnetron sputtering, *Nanoscale* 7(6) (2015) 2497-2503. <https://doi.org/10.1039/C4NR06411A>
- [114] C. Muratore, J.J. Hu, B. Wang, M.A. Haque, J.E. Bultman, M.L. Jespersen, P.J. Shamberger, M.E. McConney, R.D. Naguy, A.A. Voevodin, Continuous ultra-thin MoS<sub>2</sub> films grown by low-temperature physical vapor deposition, *Applied Physics Letters* 104(26) (2014) 261604. <https://doi.org/10.1063/1.4885391>
- [115] X. Zhang, Y. Zhang, B.-B. Yu, X.-L. Yin, W.-J. Jiang, Y. Jiang, J.-S. Hu, L.-J. Wan, Physical vapor deposition of amorphous MoS<sub>2</sub> nanosheet arrays on carbon cloth for highly reproducible large-area electrocatalysts for the hydrogen evolution reaction, *Journal of Materials Chemistry A* 3(38) (2015) 19277-19281. <https://doi.org/10.1039/C5TA05793K>
- [116] X. Qin, P. Ke, A. Wang, K.H. Kim, Microstructure, mechanical and tribological behaviors of MoS<sub>2</sub>-Ti composite coatings deposited by a hybrid HIPIMS method, *Surface and Coatings Technology* 228 (2013) 275-281. <https://doi.org/10.1016/j.surfcoat.2013.04.040>
- [117] J. Strachan, A.F. Masters, T. Maschmeyer, Critical review: hydrothermal synthesis of 1T-MoS<sub>2</sub> – an important route to a promising material, *Journal of Materials Chemistry A* 9(15) (2021) 9451-9461. <https://doi.org/10.1039/D1TA01230D>
- [118] J.H. Zhan, Z.D. Zhang, X.F. Qian, C. Wang, Y. Xie, Y.T. Qian, Solvothermal Synthesis of Nanocrystalline MoS<sub>2</sub> from MoO<sub>3</sub> and Elemental Sulfur, *Journal of Solid State Chemistry* 141(1) (1998) 270-273. <https://doi.org/10.1006/jssc.1998.7991>
- [119] H. Lin, X. Chen, H. Li, M. Yang, Y. Qi, Hydrothermal synthesis and characterization of MoS<sub>2</sub> nanorods, *Materials Letters* 64(15) (2010) 1748-1750. <https://doi.org/10.1016/j.matlet.2010.04.032>
- [120] J. Xie, J. Zhang, S. Li, F. Grote, X. Zhang, H. Zhang, R. Wang, Y. Lei, B. Pan, Y. Xie, Controllable Disorder Engineering in Oxygen-Incorporated MoS<sub>2</sub> Ultrathin Nanosheets for Efficient Hydrogen Evolution, *Journal of the American Chemical Society* 135(47) (2013) 17881-17888. <https://doi.org/10.1021/ja408329q>
- [121] M. Zhao, X. Ma, S. Yan, H. Xiao, Y. Li, T. Hu, Z. Zheng, J. Jia, H. Wu, Solvothermal synthesis of oxygen-incorporated MoS<sub>2-x</sub> nanosheets with abundant undercoordinated Mo for efficient hydrogen evolution, *International Journal of Hydrogen Energy* 45(38) (2020) 19133-19143. <https://doi.org/10.1016/j.ijhydene.2020.05.003>
- [122] P.W. Dunne, A.S. Munn, C.L. Starkey, E.H. Lester, The sequential continuous-flow hydrothermal synthesis of molybdenum disulphide, *Chemical Communications* 51(19) (2015) 4048-4050. <https://doi.org/10.1039/C4CC10158H>
- [123] H. Miao, X. Hu, Q. Sun, Y. Hao, H. Wu, D. Zhang, J. Bai, E. Liu, J. Fan, X. Hou, Hydrothermal synthesis of MoS<sub>2</sub> nanosheets films: Microstructure and formation mechanism research, *Materials Letters* 166 (2016) 121-124. <https://doi.org/10.1016/j.matlet.2015.12.010>
- [124] . Liu, X. Li, Q. He, A. Khalil, D. Liu, T. Xiang, X. Wu, L. Song, Gram-Scale Aqueous Synthesis of Stable Few-Layered 1T-MoS<sub>2</sub>: Applications for Visible-Light-

- Driven Photocatalytic Hydrogen Evolution, *Small* 11(41) (2015) 5556-5564. <https://doi.org/10.1002/smll.201501822>
- [125] X. Sun, Y.a. Pang, S. Li, Y. Yu, X. Ding, L. Wang, Q. Zhang, High performance asymmetric supercapacitor based on 3D microsphere-like 1T-MoS<sub>2</sub> with high 1T phase content, *Ceramics International* 48(15) (2022) 21317-21326. <https://doi.org/10.1016/j.ceramint.2022.04.098>
- [126] . Wang, X. Zhang, S. Bao, Z. Zhang, H. Fei, Z. Wu, Phase engineering of a multiphasic 1T/2H MoS<sub>2</sub> catalyst for highly efficient hydrogen evolution, *Journal of Materials Chemistry A* 5(6) (2017) 2681-2688. <https://doi.org/10.1039/C6TA09409K>
- [127] Z. Liu, Z. Gao, Y. Liu, M. Xia, R. Wang, N. Li, Heterogeneous Nanostructure Based on 1T-Phase MoS<sub>2</sub> for Enhanced Electrocatalytic Hydrogen Evolution, *ACS Applied Materials & Interfaces* 9(30) (2017) 25291-25297. <https://doi.org/10.1021/acsami.7b05775>
- [128] H. Li, H. Li, Z. Wu, L. Zhu, C. Li, S. Lin, X. Zhu, Y. Sun, Realization of high-purity 1T-MoS<sub>2</sub> by hydrothermal synthesis through synergistic effect of nitric acid and ethanol for supercapacitors, *Journal of Materials Science & Technology* 123 (2022) 34-40. <https://doi.org/10.1016/j.jmst.2022.01.018>
- [129] Y. Yao, K. Ao, P. Lv, Q. Wei, MoS<sub>2</sub> Coexisting in 1T and 2H Phases Synthesized by Common Hydrothermal Method for Hydrogen Evolution Reaction, *Nanomaterials* 9(6) (2019) 844. <https://doi.org/10.3390/nano9060844>
- [130] Z. Wang, Z. Guo, Y. Gao, D. Wang, X. Cui, Stable Mo/1T-MoS<sub>2</sub> Monolith Catalyst with a Metallic Interface for Large Current Water Splitting, *ACS Applied Materials & Interfaces* 15(11) (2023) 14206-14214. <https://doi.org/10.1021/acsami.2c19983>
- [131] S. Venkateswaran, S.M. Senthil Kumar, Template-Driven Phase Selective Formation of Metallic 1T-MoS<sub>2</sub> Nanoflowers for Hydrogen Evolution Reaction, *ACS Sustainable Chemistry & Engineering* 7(2) (2019) 2008-2017. <https://doi.org/10.1021/acssuschemeng.8b04335>
- [132] W. Ding, L. Hu, J. Dai, X. Tang, R. Wei, Z. Sheng, C. Liang, D. Shao, W. Song, Q. Liu, M. Chen, X. Zhu, S. Chou, X. Zhu, Q. Chen, Y. Sun, S.X. Dou, Highly Ambient-Stable 1T-MoS<sub>2</sub> and 1T-WS<sub>2</sub> by Hydrothermal Synthesis under High Magnetic Fields, *ACS Nano* 13(2) (2019) 1694-1702. <https://doi.org/10.1021/acsnano.8b07744>
- [133] Y. Shi, Y. Zhou, D.-R. Yang, W.-X. Xu, C. Wang, F.-B. Wang, J.-J. Xu, X.-H. Xia, H.-Y. Chen, Energy Level Engineering of MoS<sub>2</sub> by Transition-Metal Doping for Accelerating Hydrogen Evolution Reaction, *Journal of the American Chemical Society* 139(43) (2017) 15479-15485. <https://doi.org/10.1021/jacs.7b08881>
- [134] B. Gao, Y. Zhao, X. Du, D. Li, S. Ding, Y. Li, C. Xiao, Z. Song, Electron injection induced phase transition of 2H to 1T MoS<sub>2</sub> by cobalt and nickel substitutional doping, *Chemical Engineering Journal* 411 (2021) 128567. <https://doi.org/10.1016/j.cej.2021.128567>
- [135] H.Y. He, Z. He, Q. Shen, Efficient hydrogen evolution catalytic activity of graphene/metallic MoS<sub>2</sub> nanosheet heterostructures synthesized by a one-step hydrothermal process, *International Journal of Hydrogen Energy* 43(48) (2018) 21835-21843. <https://doi.org/10.1016/j.ijhydene.2018.10.023>
- [136] Z. Lin, T. Feng, X. Ma, G. Liu, Fe/Ni bi-metallic organic framework supported 1T/2H MoS<sub>2</sub> heterostructures as efficient bifunctional electrocatalysts for hydrogen and oxygen evolution, *Fuel* 339 (2023) 127395. <https://doi.org/10.1016/j.fuel.2023.127395>

- [137] J. Xie, H. Zhang, S. Li, R. Wang, X. Sun, M. Zhou, J. Zhou, X.W. Lou, Y. Xie, Defect-Rich MoS<sub>2</sub> Ultrathin Nanosheets with Additional Active Edge Sites for Enhanced Electrocatalytic Hydrogen Evolution, *Advanced Materials* 25(40) (2013) 5807-5813. <https://doi.org/10.1002/adma.201302685>
- [138] Y. Nakayasu, H. Kobayashi, S. Katahira, T. Tomai, I. Honma, Rapid, one-step fabrication of MoS<sub>2</sub> electrocatalysts by hydrothermal electrodeposition, *Electrochemistry Communications* 134 (2022) 107180. <https://doi.org/10.1016/j.elecom.2021.107180>
- [139] W. Kreuter, H. Hofmann, Electrolysis: The important energy transformer in a world of sustainable energy, *International Journal of Hydrogen Energy* 23(8) (1998) 661-666. [https://doi.org/10.1016/S0360-3199\(97\)00109-2](https://doi.org/10.1016/S0360-3199(97)00109-2)
- [140] S. Anantharaj, S.R. Ede, K. Karthick, S. Sam Sankar, K. Sangeetha, P.E. Karthik, S. Kundu, Precision and correctness in the evaluation of electrocatalytic water splitting: revisiting activity parameters with a critical assessment, *Energy & Environmental Science* 11(4) (2018) 744-771. <https://doi.org/10.1039/C7EE03457A>
- [141] J.D. Benck, T.R. Hellstern, J. Kibsgaard, P. Chakthranont, T.F. Jaramillo, Catalyzing the Hydrogen Evolution Reaction (HER) with Molybdenum Sulfide Nanomaterials, *ACS Catalysis* 4(11) (2014) 3957-3971. <https://doi.org/10.1021/cs500923c>
- [142] Z. Yin, X. Liu, S. Chen, T. Ma, Y. Li, Interface Engineering and Anion Engineering of Mo-Based Heterogeneous Electrocatalysts for Hydrogen Evolution Reaction, *Energy & Environmental Materials* 6(1) (2023) e12310. <https://doi.org/10.1002/eem2.12310>
- [143] X. Huang, M. Leng, W. Xiao, M. Li, J. Ding, T.L. Tan, W.S.V. Lee, J. Xue, Activating Basal Planes and S-Terminated Edges of MoS<sub>2</sub> toward More Efficient Hydrogen Evolution, *Advanced Functional Materials* 27(6) (2017) 1604943. <https://doi.org/10.1002/adfm.201604943>
- [144] C. Tsai, F. Abild-Pedersen, J.K. Nørskov, Tuning the MoS<sub>2</sub> Edge-Site Activity for Hydrogen Evolution via Support Interactions, *Nano Letters* 14(3) (2014) 1381-1387. <https://doi.org/10.1021/nl404444k>
- [145] T.F. Jaramillo, K.P. Jørgensen, J. Bonde, J.H. Nielsen, S. Horch, I. Chorkendorff, Identification of Active Edge Sites for Electrochemical H<sub>2</sub> Evolution from MoS<sub>2</sub> Nanocatalysts, *Science* 317(5834) (2007) 100-102. <https://doi.org/10.1126/science.1141483>
- [146] J. Kibsgaard, Z. Chen, B.N. Reinecke, T.F. Jaramillo, Engineering the surface structure of MoS<sub>2</sub> to preferentially expose active edge sites for electrocatalysis, *Nature Materials* 11(11) (2012) 963-969. <https://doi.org/10.1038/nmat3439>
- [147] C. Tsai, K. Chan, J.K. Nørskov, F. Abild-Pedersen, Theoretical insights into the hydrogen evolution activity of layered transition metal dichalcogenides, *Surface Science* 640 (2015) 133-140. <https://doi.org/10.1016/j.susc.2015.01.019>
- [148] C.L. Bentley, M. Kang, F.M. Maddar, F. Li, M. Walker, J. Zhang, P.R. Unwin, Electrochemical maps and movies of the hydrogen evolution reaction on natural crystals of molybdenite (MoS<sub>2</sub>): basal vs. edge plane activity, *Chemical Science* 8(9) (2017) 6583-6593. <https://doi.org/10.1039/C7SC02545A>
- [149] M.G. Walter, E.L. Warren, J.R. McKone, S.W. Boettcher, Q. Mi, E.A. Santori, N.S. Lewis, Solar Water Splitting Cells, *Chemical Reviews* 110(11) (2010) 6446-6473. <https://doi.org/10.1021/cr1002326>
- [150] T. Shinagawa, A.T. Garcia-Esparza, K. Takanabe, Insight on Tafel slopes from a microkinetic analysis of aqueous electrocatalysis for energy conversion, *Scientific Reports* 5(1) (2015) 13801. <https://doi.org/10.1038/srep13801>

- [151] M. Boudart, Turnover Rates in Heterogeneous Catalysis, *Chemical Reviews* 95(3) (1995) 661-666. <https://doi.org/10.1021/cr00035a009>
- [152] D. Wang, Y. Xiao, X. Luo, Z. Wu, Y.-J. Wang, B. Fang, Swollen Ammoniated MoS<sub>2</sub> with 1T/2H Hybrid Phases for High-Rate Electrochemical Energy Storage, *ACS Sustainable Chemistry & Engineering* 5(3) (2017) 2509-2515. <https://doi.org/10.1021/acssuschemeng.6b02863>
- [153] D.J. Late, B. Liu, H.S.S.R. Matte, C.N.R. Rao, V.P. Dravid, Rapid Characterization of Ultrathin Layers of Chalcogenides on SiO<sub>2</sub>/Si Substrates, *Advanced Functional Materials* 22(9) (2012) 1894-1905. <https://doi.org/10.1002/adfm.201102913>
- [154] S. Morajkar, B. Srinivasan, Convenient synthesis and Raman spectral characterization of diammonium monomolybdate(VI), *Indian Journal of Chemistry Section a* 59A (2020) 1760. <http://nopr.niscpr.res.in/handle/123456789/55746>
- [155] G. Tzvetkov, F.P. Netzer, X-ray induced irradiation effects in glycine thin films: A time-dependent XPS and TPD study, *Journal of Electron Spectroscopy and Related Phenomena* 182(1) (2010) 41-46. <https://doi.org/10.1016/j.elspec.2010.05.029>
- [156] V. Klimas, C. Bittencourt, G. Valušis, A. Jagminas, Calcination effects of 2D molybdenum disulfides, *Materials Characterization* 179 (2021) 111351. <https://doi.org/10.1016/j.matchar.2021.111351>
- [157] I.M. Weiss, C. Muth, R. Drumm, H.O.K. Kirchner, Thermal decomposition of the amino acids glycine, cysteine, aspartic acid, asparagine, glutamic acid, glutamine, arginine and histidine, *BMC Biophysics* 11(1) (2018) 2. <https://doi.org/10.1186/s13628-018-0042-4>.
- [158] A. Lasia, *Electrochemical Impedance Spectroscopy and its Applications*, Springer New York, NY 2014. <https://doi.org/10.1007/978-1-4614-8933-7>
- [159] E.B. Castro, M.J. de Giz, E.R. Gonzalez, J.R. Vilche, An electrochemical impedance study on the kinetics and mechanism of the hydrogen evolution reaction on nickel molybdenite electrodes, *Electrochimica Acta* 42(6) (1997) 951-959. [https://doi.org/10.1016/S0013-4686\(96\)00272-1](https://doi.org/10.1016/S0013-4686(96)00272-1)
- [160] G.J. Brug, A.L.G. van den Eeden, M. Sluyters-Rehbach, J.H. Sluyters, The analysis of electrode impedances complicated by the presence of a constant phase element, *Journal of Electroanalytical Chemistry and Interfacial Electrochemistry* 176(1) (1984) 275-295. [https://doi.org/10.1016/S0022-0728\(84\)80324-1](https://doi.org/10.1016/S0022-0728(84)80324-1)
- [161] A. Lasia, Mechanism and kinetics of the hydrogen evolution reaction, *International Journal of Hydrogen Energy* 44(36) (2019) 19484-19518. <https://doi.org/10.1016/j.ijhydene.2019.05.183>
- [162] K.E. Ramohlolola, E.I. Iwuoha, M.J. Hato, K.D. Modibane, Instrumental Techniques for Characterization of Molybdenum Disulphide Nanostructures, *Journal of Analytical Methods in Chemistry* 2020 (2020) 8896698. <https://doi.org/10.1155/2020/8896698>
- [163] A.S. Krishna Kumar, S.-J. Jiang, J.K. Warchał, Synthesis and Characterization of Two-Dimensional Transition Metal Dichalcogenide Magnetic MoS<sub>2</sub>@Fe<sub>3</sub>O<sub>4</sub> Nanoparticles for Adsorption of Cr(VI)/Cr(III), *ACS Omega* 2(9) (2017) 6187-6200. <https://doi.org/10.1021/acsomega.7b00757>
- [164] J. Kong, S. Yu, Fourier Transform Infrared Spectroscopic Analysis of Protein Secondary Structures, *Acta Biochimica et Biophysica Sinica* 39(8) (2007) 549-559. <https://doi.org/10.1111/j.1745-7270.2007.00320.x>
- [165] X. Gan, L.Y.S. Lee, K.-y. Wong, T.W. Lo, K.H. Ho, D.Y. Lei, H. Zhao, 2H/1T Phase Transition of Multilayer MoS<sub>2</sub> by Electrochemical Incorporation of S

Vacancies, ACS Applied Energy Materials 1(9) (2018) 4754-4765.  
<https://doi.org/10.1021/acsaem.8b00875>

[166] F. Ling, X. Liu, H. Jing, Y. Chen, W. Zeng, Y. Zhang, W. Kang, J. Liu, L. Fang, M. Zhou, Optimizing edges and defects of supported MoS<sub>2</sub> catalysts for hydrogen evolution via an external electric field, Physical Chemistry Chemical Physics 20(41) (2018) 26083-26090. <https://doi.org/10.1039/C8CP03407A>

[167] X. Wang, B. Wang, Q. Zhang, Y. Sun, E. Wang, H. Luo, Y. Wu, L. Gu, H. Li, K. Liu, Grain-Boundary Engineering of Monolayer MoS<sub>2</sub> for Energy-Efficient Lateral Synaptic Devices, Advanced Materials 33(32) (2021) 2102435. <https://doi.org/10.1002/adma.202102435>

[168] J. Bonde, P.G. Moses, T.F. Jaramillo, J.K. Nørskov, I. Chorkendorff, Hydrogen evolution on nano-particulate transition metal sulfides, Faraday Discussions 140(0) (2009) 219-231. <https://doi.org/10.1039/B803857K>

[169] W. Kautek, H. Gerischer, Anisotropic photocorrosion of n-type MoS<sub>2</sub> MoSe<sub>2</sub>, and WSe<sub>2</sub> single crystal surfaces: the role of cleavage steps, line and screw dislocations, Surface Science 119(1) (1982) 46-60. [https://doi.org/10.1016/0039-6028\(82\)90186-8](https://doi.org/10.1016/0039-6028(82)90186-8)

[170] J. Kibsgaard, T.F. Jaramillo, F. Besenbacher, Building an appropriate active-site motif into a hydrogen-evolution catalyst with thiomolybdate [Mo<sub>3</sub>S<sub>13</sub>]<sup>2-</sup> clusters, Nature Chemistry 6(3) (2014) 248-253. <https://doi.org/10.1038/nchem.1853>

[171] A. Anto Jeffery, C. Nethravathi, M. Rajamathi, Two-Dimensional Nanosheets and Layered Hybrids of MoS<sub>2</sub> and WS<sub>2</sub> through Exfoliation of Ammoniated MS<sub>2</sub> (M = Mo,W), The Journal of Physical Chemistry C 118(2) (2014) 1386-1396. <https://doi.org/10.1021/jp410918c>

[172] A. Ambrosi, Z. Sofer, M. Pumera, Lithium Intercalation Compound Dramatically Influences the Electrochemical Properties of Exfoliated MoS<sub>2</sub>, Small 11(5) (2015) 605-612. <https://doi.org/10.1002/smll.201400401>

[173] Q. Yang, Y. He, Y. Fan, F. Li, X. Chen, Exfoliation of the defect-rich MoS<sub>2</sub> nanosheets to obtain nanodots modified MoS<sub>2</sub> thin nanosheets for electrocatalytic hydrogen evolution, Journal of Materials Science: Materials in Electronics 28 (2017) 7413-7418. <https://doi.org/10.1007/s10854-017-6430-8>

[174] Y. Takahashi, Y. Nakayasu, K. Iwase, H. Kobayashi, I. Honma, Supercritical hydrothermal synthesis of MoS<sub>2</sub> nanosheets with controllable layer number and phase structure, Dalton Transactions 49(27) (2020) 9377-9384. <https://doi.org/10.1039/D0DT01453B>

[175] P. Cao, N. Chen, W. Tang, Y. Liu, Y. Xia, Z. Wu, F. Li, Y. Liu, A. Sun, Template-assisted hydrothermal synthesized hydrophilic spherical 1T-MoS<sub>2</sub> with excellent zinc storage performance, Journal of Alloys and Compounds 898 (2022) 162854. <https://doi.org/10.1016/j.jallcom.2021.162854>

[176] O. Mabayoje, Y. Liu, M. Wang, A. Shoola, A.M. Ebrahim, A.I. Frenkel, C.B. Mullins, Electrodeposition of MoS<sub>x</sub> Hydrogen Evolution Catalysts from Sulfur-Rich Precursors, ACS Applied Materials & Interfaces 11(36) (2019) 32879-32886. <https://doi.org/10.1021/acsami.9b07277>

[177] B. Seo, G.Y. Jung, S.J. Lee, D.S. Baek, Y.J. Sa, H.W. Ban, J.S. Son, K. Park, S.K. Kwak, S.H. Joo, Monomeric MoS<sub>4</sub><sup>2-</sup>-Derived Polymeric Chains with Active Molecular Units for Efficient Hydrogen Evolution Reaction, ACS Catalysis 10(1) (2020) 652-662. <https://doi.org/10.1021/acscatal.9b02700>

[178] T. Weber, J.C. Muijsers, J.W. Niemantsverdriet, Structure of Amorphous MoS<sub>3</sub>, The Journal of Physical Chemistry 99(22) (1995) 9194-9200. <https://doi.org/10.1021/j100022a037>

- [179] Y. Deng, L.R.L. Ting, P.H.L. Neo, Y.-J. Zhang, A.A. Peterson, B.S. Yeo, Operando Raman Spectroscopy of Amorphous Molybdenum Sulfide ( $\text{MoS}_x$ ) during the Electrochemical Hydrogen Evolution Reaction: Identification of Sulfur Atoms as Catalytically Active Sites for  $\text{H}^+$  Reduction, *ACS Catalysis* 6(11) (2016) 7790-7798. <https://doi.org/10.1021/acscatal.6b01848>
- [180] M.-L. Grutza, A. Rajagopal, C. Streb, P. Kurz, Hydrogen evolution catalysis by molybdenum sulfides ( $\text{MoS}_x$ ): are thiomolybdate clusters like  $[\text{Mo}_3\text{S}_{13}]^{2-}$  suitable active site models?, *Sustainable Energy & Fuels* 2(9) (2018) 1893-1904. <https://doi.org/10.1039/C8SE00155C>
- [181] T. Weber, J.C. Muijsers, J.H.M.C. van Wolput, C.P.J. Verhagen, J.W. Niemantsverdriet, Basic Reaction Steps in the Sulfidation of Crystalline  $\text{MoO}_3$  to  $\text{MoS}_2$ , As Studied by X-ray Photoelectron and Infrared Emission Spectroscopy, *The Journal of Physical Chemistry* 100(33) (1996) 14144-14150. <https://doi.org/10.1021/jp961204y>
- [182] L. Sygellou, An in-situ photoelectron spectroscopy study of the thermal processing of ammonium tetrathiomolybdate,  $(\text{NH}_4)_2\text{MoS}_4$ , precursor, *Applied Surface Science* 476 (2019) 1079-1085. <https://doi.org/10.1016/j.apsusc.2019.01.193>
- [183] S.H. Laurie, Thiomolybdates — Simple but Very Versatile Reagents, *European Journal of Inorganic Chemistry* 2000(12) (2000) 2443-2450. [https://doi.org/10.1002/1099-0682\(200012\)2000:12<2443::AID-EJIC2443>3.0.CO;2-I](https://doi.org/10.1002/1099-0682(200012)2000:12<2443::AID-EJIC2443>3.0.CO;2-I)
- [184] H. Li, C. Tsai, A.L. Koh, L. Cai, A.W. Contryman, A.H. Fragapane, J. Zhao, H.S. Han, H.C. Manoharan, F. Abild-Pedersen, J.K. Nørskov, X. Zheng, Activating and optimizing  $\text{MoS}_2$  basal planes for hydrogen evolution through the formation of strained sulphur vacancies, *Nature Materials* 15(1) (2016) 48-53. <https://doi.org/10.1038/nmat4465>
- [185] H.H. Do, T.D.C. Ha, H. Jo, K.M. Ok, J.H. Cho, S.H. Ahn, M.-G. Kim, S.Y. Kim, Low-temperature synthesis of molybdenum sulfides, tungsten sulfides, and composites thereof as efficient electrocatalysts for hydrogen evolution reaction, *Applied Surface Science* 576 (2022) 151828. <https://doi.org/10.1016/j.apsusc.2021.151828>
- [186] L.R.L. Ting, Y. Deng, L. Ma, Y.-J. Zhang, A.A. Peterson, B.S. Yeo, Catalytic Activities of Sulfur Atoms in Amorphous Molybdenum Sulfide for the Electrochemical Hydrogen Evolution Reaction, *ACS Catalysis* 6(2) (2016) 861-867. <https://doi.org/10.1021/acscatal.5b02369>
- [187] C. Tsai, H. Li, S. Park, J. Park, H.S. Han, J.K. Nørskov, X. Zheng, F. Abild-Pedersen, Electrochemical generation of sulfur vacancies in the basal plane of  $\text{MoS}_2$  for hydrogen evolution, *Nature Communications* 8(1) (2017) 15113. <https://doi.org/10.1038/ncomms15113>
- [188] H. Vrubel, D. Merki, X. Hu, Hydrogen evolution catalyzed by  $\text{MoS}_3$  and  $\text{MoS}_2$  particles, *Energy & Environmental Science* 5(3) (2012) 6136-6144. <https://doi.org/10.1039/C2EE02835B>
- [189] J.D. Benck, Z. Chen, L.Y. Kuritzky, A.J. Forman, T.F. Jaramillo, Amorphous Molybdenum Sulfide Catalysts for Electrochemical Hydrogen Production: Insights into the Origin of their Catalytic Activity, *ACS Catalysis* 2(9) (2012) 1916-1923. <https://doi.org/10.1021/cs300451q>
- [190] P. Joensen, E.D. Crozier, N. Alberding, R.F. Frindt, A study of single-layer and restacked  $\text{MoS}_2$  by X-ray diffraction and X-ray absorption spectroscopy, *Journal of Physics C: Solid State Physics* 20(26) (1987) 4043. <https://doi.org/10.1088/0022-3719/20/26/009>

[191] G. Li, D. Zhang, Q. Qiao, Y. Yu, D. Peterson, A. Zafar, R. Kumar, S. Curtarolo, F. Hunte, S. Shannon, Y. Zhu, W. Yang, L. Cao, All The Catalytic Active Sites of MoS<sub>2</sub> for Hydrogen Evolution, *Journal of the American Chemical Society* 138(51) (2016) 16632-16638. <https://doi.org/10.1021/jacs.6b05940>

[192] N. Abidi, A. Bonduelle-Skrzypczak, S.N. Steinmann, How Stable Are 2H-MoS<sub>2</sub> Edges under Hydrogen Evolution Reaction Conditions?, *The Journal of Physical Chemistry C* 125(31) (2021) 17058-17067. <https://doi.org/10.33774/chemrxiv-2021-63rbf-v2>

## NOTES

Vilniaus universiteto leidykla  
Saulėtekio al. 9, III rūmai, LT-10222 Vilnius  
El. p. [info@leidykla.vu.lt](mailto:info@leidykla.vu.lt), [www.leidykla.vu.lt](http://www.leidykla.vu.lt)  
[bookshop.vu.lt](http://bookshop.vu.lt), [journals.vu.lt](http://journals.vu.lt)  
Tiražas 20 egz.